Spin relaxation in quantum Hall edge states
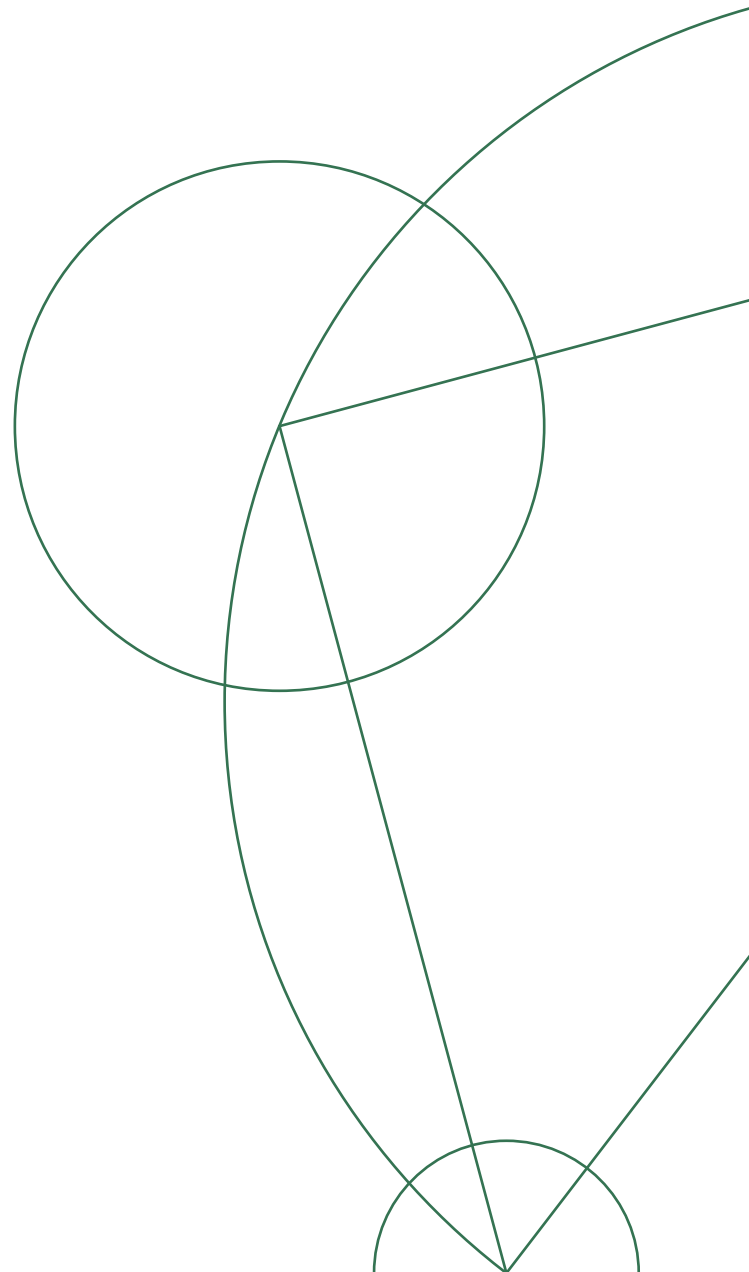
Stef P.J. Koenis

Niels Bohr Institute
University of Copenhagen
Jagtvej 155A, DK-2200, Copenhagen, Denmark

Master's thesis in Physics
Advisor: Mark S. Rudner

Dated: May 12, 2021

Abstract

When a two-dimensional electron gas at liquid helium temperature is exposed to a perpendicular magnetic field, it enters the quantum Hall effect (QHE) regime. In this regime, current flows in channels at the edges. In a set-up with quantum point contacts (QPCs), it is possible to create non-equilibrium populations in neighbouring spin-polarised edge channels. The hyperfine interaction mediates relaxation between the spin-polarised edge channels and thus creates dynamical polarisation of the nuclei (DNP). Understanding this spin relaxation may give us further insight into the different phases of matter of the QHE.

In this thesis, we theoretically study spin relaxation in the integer QHE. Both elastic and inelastic processes are considered. We compare different edge models of which the semi-classical, interacting Chklovskii, Shklovskii & Glazman (CSG) model performs best at predicting the experimentally observed scattering rates. We use a mean-field (Hartree-only) analysis to infer the non-equilibrium band structures and their fillings in the CSG model. Our results qualitatively account for non-linear transport behaviour observed in experiments, and also reveal great sensitivity to the detailed structure of the edge.

1

Acknowledgements

Contents

Chapter 1

Introduction

The physical phenomenon that lies at the heart of the physics investigated in this thesis is the quantum Hall effect (QHE). However, even before talking about the QHE, it is helpful to remember its classical analogue: the Hall effect. In 1879, Edwin Hall investigated the electrical resistance of a metal strip subject to a perpendicular magnetic field. He discovered that when a current is sent through the strip, a voltage is generated in the direction perpendicular to the current flow [1]. This perpendicular voltage we refer to as the Hall voltage (V_H). A typical measurement set-up for the Hall effect is the Hall bar displayed in Fig. 1.1. This effect is explained by the fact that moving charges in a magnetic field experience a magnetic (Lorentz) force $\vec{F}_m = q\vec{v} \times \vec{B}$ that has a direction perpendicular to both the velocity and the magnetic field. In general, such a perpendicular magnetic field causes a charged particle to move around in circles, the so-called *cyclotron orbits*. In the Hall bar shown in Fig. 1.1, a negatively charged particle that flows from contact 1 to contact 4 is deflected upward because of the magnetic force. A negative charge accumulates at the top of the sample, and a Hall voltage can be measured between contacts 3 and 5. The Hall voltage grows until the electric force $\vec{F}_e = q\vec{E}$ in the $\hat{x}$-direction that is caused by the charge difference between the edges, cancels the magnetic force.

In 1980, Klaus von Klitzing and collaborators [2] discovered a quantum version of the classical Hall effect whereby the Hall conductance is quantised to integer multiples of the conductance quantum $\frac{e^2}{h}$. This integer quantum Hall effect (IQHE) can be observed in a two-dimensional system at dilution fridge temperatures, again with a perpendicular magnetic field (see left panel of Fig. 1.2). It turns out that the quantised value of the conductance on the plateaus (see right panel of Fig. 1.2) is extraordinarily robust, independent of any microscopic details of the sample, and reproducible: the relative uncertainty is only a few parts in 10^9. Because of its universality, the IQHE has been used to provide the electrical resistance standard since 1990 [3]. At a plateau, the longitudinal resistance disappears, and the system facilitates dissipationless transport. When we change the strength of the perpendicular magnetic field, the system transitions into a different plateau. During this transition, the longitudinal resistance becomes non-zero,
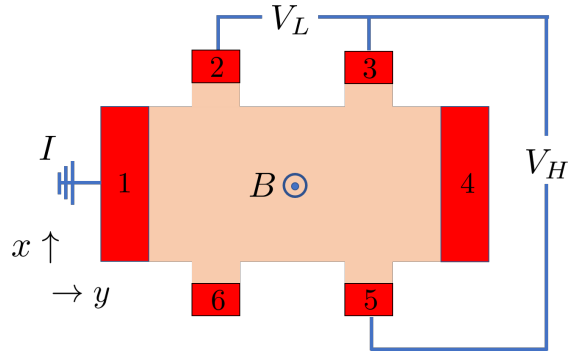
Figure 1.1: Hall bar set-up. A current flows between contacts 1 and 4. The longitudinal voltage V_L is measured between contacts 2 and 3, and the Hall voltage V_H between contacts 3 and 5. The magnetic field is in the $\hat{z}$-direction.
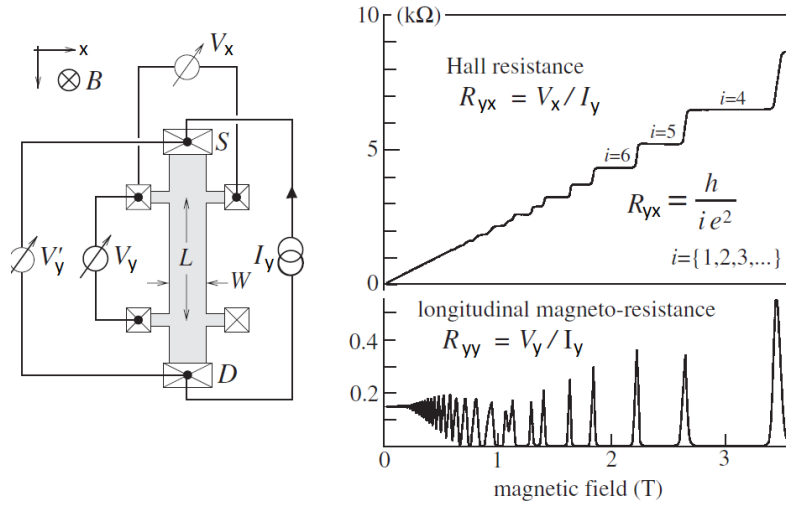
Figure 1.2: A typical quantum Hall measurement in the low magnetic field regime. The experimental Hall-bar set-up is displayed in the left panel and the right panel shows the measured Hall resistance and longitudinal resistance. Figure adapted from [3].

and the system becomes dissipative (see right panel of Fig. 1.2).

In 1982, Tsui et al. discovered that when the magnetic field is made even stronger, the conductance quantisation extends to rational fractions of $\frac{e^2}{h}$ [4]. The discovery of this *fractional* quantum Hall effect (FQHE) opened a fascinating new field in condensed matter physics. The FQHE is interesting from a fundamental point of view because we can study it to improve our understanding of strongly correlated quantum systems in general. Apart from this fundamental interest, the FQHE also plays a role in a proposal for a topological quantum computer. In this proposal, the non-abelian statistics of the FQHE quasi-particles protect the quantum states in the quantum computer against de-

6

coherence [5, 6].

There are many different IQH and FQH states with different types of internal structure (including spin). For example, the $\frac{2}{3}$ fraction supports multiple distinct phases [7]. We can investigate the transitions between these phases by using the hyperfine coupling between the electronic and nuclear spins. By driving the electronic system out of equilibrium, this coupling can cause dynamic nuclear polarisation (DNP). DNP can be used as a tool to learn more about the IQH and FQH phases of matter. Several studies [8, 9] have used DNP to study the edge structure in the IQHE.

Yusa et al. [10] and Hennel et al. [7] investigated DNP in a FQH system constricted by a quantum point contact (see left inset in Fig. 1.3a). They biased the system by applying a constant voltage or current between the source (S) and drain (D) contacts. Surprisingly, they found the longitudinal resistance showed very slow temporal oscillations (see Fig. 1.3). The mechanism behind these oscillations is believed to be an intricate interplay between DNP at the edges and nuclear spin-diffusion [7].

Many knowledge gaps need to be filled to understand this mechanism quantitatively: How exactly is the DNP created? Where in the sample is it created? How does it diffuse? How does DNP affect electronic transport? More generally, by investigating these questions we will develop a deeper understanding of non-equilibrium dynamics in quantum Hall edge states, which may help give further insight into the QH phases of matter.

(a)

(b)
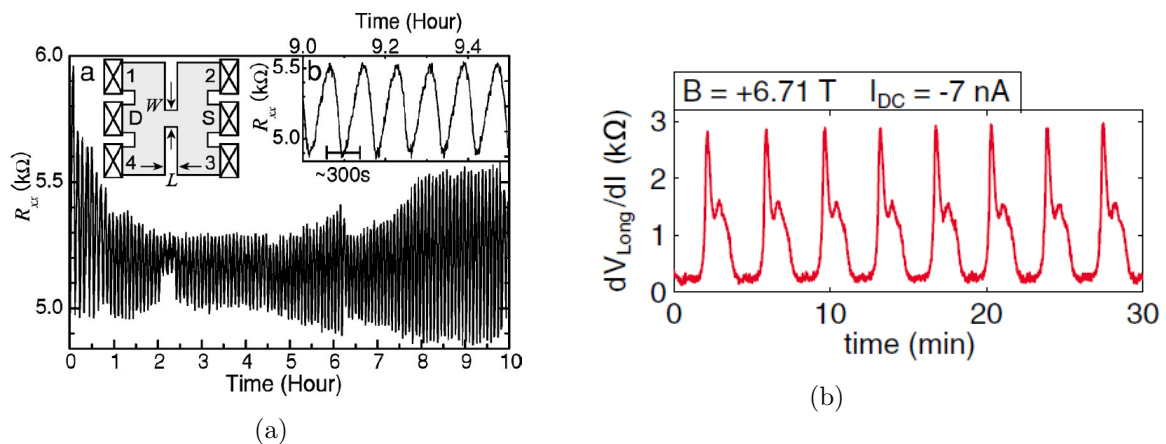
Figure 1.3: Spontaneous temporal oscillations in FQHE systems. Panel (a) shows the set-up and result of the Yusa et al. [10] experiment. The experiment is performed at the $\frac{2}{3}$ FQHE, magnetic field 7.5 T, and temperature 0.3 K. The voltage is fixed and the current between the source and the drain oscillates around 3.57 nA. Panel (b) shows the result of the Hennel et al. [7] at the same filling factor. This measurement was carried out at a temperature of 70 mK. In contrast to the other experiment, the current was fixed.

In this thesis, we look at the mechanism creating DNP. We study spin-scattering mediated by the hyperfine interaction in the somewhat simpler IQHE. By doing so, we aspire to build a foundation of knowledge about scattering that can be used to better understand this intriguing phenomenon within the FQHE. As we will see, even in the relatively simple IQHE regime, the problem is highly complex and is sensitive to a variety of system details.

This thesis is outlined as follows: in chapter 2, we discuss the quantum Hall effect and introduce different edge channel models. We end the chapter with a detailed discussion of experiments that measured scattering between spin-polarised edge channels. In chapter 3, we present the non-equilibrium versions of the models that we introduced in chapter 2. After that, we set up the calculation for the spin-scattering rate. We calculate spin-scattering rates and compare them to the experimental data in chapter 4. At the end of this chapter, we assess which of the different theoretical models is best suited to describe spin-scattering in an integer quantum Hall system. In chapter 5, we discuss the lessons learnt, the limitations of our model, and directions for future research.

Chapter 2

Background

In this chapter, we discuss the microscopic origin of the QHE. In the Hall bar geometry, the theory of edge channels can explain many properties of the system in the QHE state, such as the phase transitions and current. We introduce different models for these edge channels. Finally, we discuss scattering between non-equilibrium edge channels. In the first part of this chapter, we closely follow the approach of Steven Girvin's excellent lecture notes on the quantum Hall effect [11].

2.1   The quantum Hall effect

As we discussed above, the QHE can be observed in a very cold two-dimensional (2D) electron system with a perpendicular magnetic field applied to it. Such a 2D electron system can for example be realised in a $GaAs/Al_xGa_{1-x}As$ heterostructure [9, 8]. In this 3D material, the energy bands are engineered such that there is a narrow well in one spatial direction, which we will call the $\hat{z}$-direction in all that follows. In the $\hat{z}$-direction, the quantised energy levels have a large energy spacing due to the narrowness of the well. Because this energy spacing is much larger than the thermal energy k_BT, all particles are in the lowest energy level. If this is the case, there is no degree of freedom left in this spatial direction, and the electrons effectively form a 2D 'gas' of electrons (2DEG).

We consider a finite 2DEG of dimensions $W \times L$ to lie in the xy-plane with the magnetic field pointing in the $\hat{z}$-direction. We will start by looking at this system using the naïve model that neglects electron-electron interactions. We will also disregard spin for the time being. The Hamiltonian for a non-interacting gas of electrons that move in this 2D system is given by:

$$H = \frac{1}{2m}(\vec{p} - q\vec{A})^2, \tag{2.1}$$

where $\vec{A}$ is the vector potential and $q = -e$ the electronic charge. We can describe the field $B\hat{z}$ with the Landau gauge $\vec{A} = xB\hat{y}$. To find the eigenstates and eigenvalues of this Hamiltonian we can use the separation-of-variables ansatz $\psi_{nk}(x,y) = \frac{1}{\sqrt{L}}e^{iky}f_{nk}(x)$

and then solve $H\psi_{nk}(x,y) = \varepsilon_{nk}\psi_{nk}(x,y)$. Here we have assumed periodic boundary conditions in the $\hat{y}$-direction so that we have for the values of k:

$$k = m\frac{2\pi}{L}, \qquad m = \{1, 2, 3...\}. \tag{2.2}$$

Throughout, we assume that the confinement in the $\hat{z}$-direction is so strong that we can approximate the $\hat{z}$-direction wave function with a delta function. This delta function effectively makes the wave function two-dimensional. The state that the wave function $\psi_{nk}(x,y)$ describes is an eigenstate of p_y so we can replace the operator p_y by the eigenvalue $\hbar k$ to get the 1D equation:

$$\frac{1}{2m}(p_x^2 + (\hbar k + eBx)^2)f_{nk}(x) = \varepsilon_{nk}f_{nk}(x).$$

This is the Schrödinger equation for a shifted harmonic oscillator and hence we find for the energies and eigenstates:

$$\psi_{nk}(x,y) = \frac{1}{\sqrt{L}}e^{iky}f_{nk}(x), \qquad f_{nk}(x) = H_n(x - X_k)e^{-\frac{1}{2l_B^2}(x-X_k)^2}, \qquad X_k = -kl_B^2, \tag{2.3}$$

$$\varepsilon_{nk} = (n + \tfrac{1}{2})\hbar\omega_c, \tag{2.4}$$

where $l_B = \sqrt{\frac{\hbar}{eB}}$ is the magnetic length and $\omega_c = \frac{eB}{m}$ the cyclotron frequency. The transverse wave functions $\{f_{nk}(x)\}$ are harmonic oscillator eigenstate wave functions centred at the positions $\{X_k\}$. The functions $\{H_n(x)\}$ are Hermite polynomials that are normalised such that $\int dx |f_{nk}(x)|^2 = 1$.

The energy eigenstates [see Eq. (2.3)] are grouped together in so-called Landau levels (LLs) wherein all states are degenerate in energy. This means that the energy only depends on the LL index n [see Eq. (2.4)], which is a non-negative integer: $\{0, 1, 2, 3, ...\}$. The grouping of all states in energy-degenerate LLs gives a peaked density of states (DoS) profile (Fig. 2.1b). The LLs are usually split up into two spin-polarised sub-LLs by the spin-splitting energy Δ. In the simplest case, the strength of the spin-splitting is determined entirely by the external magnetic field via the Zeeman term: $E_z = g\mu_B B S_z$. Here g is the g-factor, which has a value -0.44 in GaAs, and S_z is the spin-z operator with eigenvalues $\pm\frac{1}{2}$.

Within this specific Landau gauge, the LL eigenstates are de-localised in the $\hat{y}$-direction and localised in the $\hat{x}$-direction. The key point is that the centre of the $\hat{x}$-localisation X_k depends on the wave-vector k of the plane wave in the $\hat{y}$-direction, which is illustrated in Fig. 2.1a.

The filling factor $\nu = n_e/n_L$ is a measure of how many of the spin-polarised sub-LLs are filled. Here n_e is the local electron density and $n_L = \frac{1}{2\pi l_B^2} = \frac{eB}{h} = \frac{B}{\Phi_0}$ the density per sub-LL, where Φ_0 is the magnetic flux quantum. We note that when B is increased through a sample of fixed area, a sub-LL can accommodate more electrons. We use the
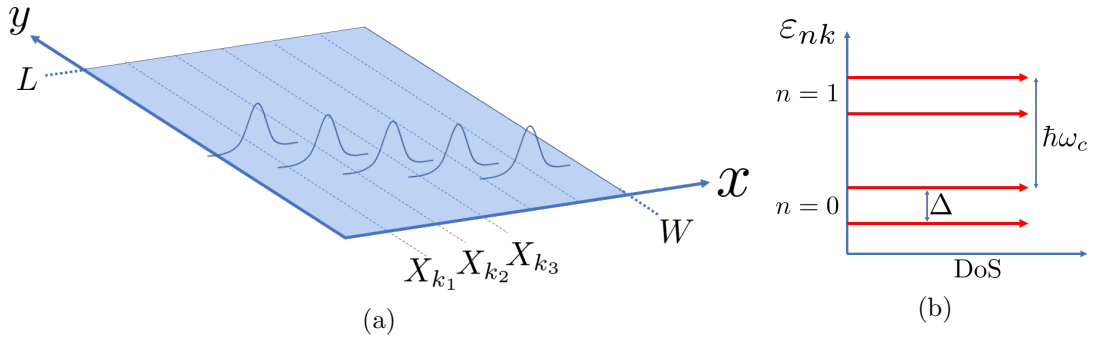
Figure 2.1: (a) Illustration of the states within a LL in a rectangular 2DEG. Each state is a delocalised plane wave in the $\hat{y}$-direction and a localised wave function in the $\hat{x}$-direction centred at $X_k = -kl_B^2$, where k is the wavenumber of the $\hat{y}$-direction plane wave. (b) Density of states (DoS) of the 2DEG with a perpendicular magnetic field. All states have collapsed in LLs with a enormous DoS. Due to the spin-splitting, the LLs are split up in two sub-LLs. Only the first two LLs are displayed.

symbol ν_0 for the filling factor of the bulk.

Having found the eigenstates of the non-interacting system without any external potential [see Eq. (2.3)], it is instructive to look at the expectation value of the single particle velocity operators:

$$v_y = \frac{dy}{dt} = (p_y + eA_y)/m, \qquad v_x = p_x/m. \qquad (2.5)$$

It turns out that $\langle v_y \rangle = \langle \psi_{nk} | (p_y + exB)/m | \psi_{nk} \rangle = 0$ and also that $\langle \psi_{nk} | v_x | \psi_{nk} \rangle = 0$ for every n and k. Intuitively this makes sense because the energy bands [see Eq. (2.4)] are completely flat, something we usually associate with a zero group velocity. Zero velocity is also what we would expect from the classical perspective: charges revolving around in cyclotron orbits do not cause any net current. Concluding, the single-particle states in Eq. (2.3) do not carry any net current, and nor does any wave-packet made up of these states.

We will mostly deal with states in the lowest LL ($n = 0$), where $H_{n=0}(x - X_k) = 1$; this makes the transverse wave functions $\{f_{nk}(x)\}$ simple Gaussians with a width of l_B [see Eq. (2.3)].

2.2 Edge channels

In the previous section, we have seen that there is no net current in the non-interacting system without an external potential. The 2DEG is confined to a finite region of space because the sample physically ends (etching or cleaving) or because some gate potential

confines the electrons to move in a finite region. Both etching and electrostatic confinement have the same qualitative effect: the energies of the states localised near the edge go up. The sample becomes fully depleted even closer to the edge because the energy required to be in that region is larger than the electrochemical potential μ [12].

In the Hall bar geometry, the confinement potential that defines the finite 2DEG causes a chiral (uni-directional) local current density at the system's edges. This chiral edge current in the so-called *edge channels* can be used to explain the main features of the QHE: plateaus of quantised Hall resistance where the longitudinal resistance disappears and non-zero longitudinal resistance between the plateaus [13]. We want to mention that the QHE has also been observed in other geometries; notably, the Corbino geometry [14]. In the Corbino disk geometry, no edges are connecting the source and drain electrodes. Hence, the net current can not be carried by edge channels. This shows that bulk transport can also cause the QHE and that the edge channel explanation is not the only possible explanation of the QHE. Still, the edge channel theory has been proven to be well-suited to the geometries that we consider, and that is why we will use it.

This section presents different models for the confined 2DEG and the associated current-carrying edge channels. We start with a naïve model that neglects electron-electron (e-e) interactions. We discuss current and the quantisation of conductance within this naïve model. Then we present the renowned Chklovksii, Shklovskii & Glazman (CSG) model [12] that takes e-e interactions into account semi-classically. Finally, we discuss more advanced theoretical models that consider the quantum effect of exchange.

2.2.1 Naïve model

Linear potential

To study the effect of the confining potential on the eigenstates and eigenenergies in the naïve model, we first take a step back and start by looking at the effect of adding the simplest possible external potential: a linear potential in the $\hat{x}$-direction: $V(x) = eEx$. Adding this potential term to the Hamiltonian in Eq. (2.1) gives the eigenstates in Eq. (2.6) and eigenenergies in Eq. (2.7):

$$\psi'_{nk}(x,y) = \frac{1}{\sqrt{L}}e^{iky}f'_{nk}(x), \qquad f'_{nk}(x) = H_n(x-X'_k)e^{-\frac{1}{2l_B^2}(x-X'_k)^2}, \qquad X'_k = -kl_B^2 - \frac{eE}{m\omega_c^2}, \tag{2.6}$$

$$\varepsilon_{nk} = (n+\frac{1}{2})\hbar\omega_c + eEX'_k + \frac{1}{2}mv^2, \qquad v = E/B. \tag{2.7}$$

We observe that the eigenstates in Eq. (2.6) are very similar to the ones without a linear potential [see Eq. (2.3)]. The difference is that the centres of the transverse wave functions $\{X'_k\}$ are shifted by an amount $\frac{eE}{m\omega_c^2}$ compared the centres $\{X_k\}$ in Eq. (2.3). The new states [see Eq. (2.6)] can be constructed as linear combinations of all Landau

level states [see Eq. (2.3)]: $\psi'_{nk} = \sum_{n'} A_{n'} \psi_{n'k}$. In the literature, this is often referred to as Landau level mixing. The external potential lifts the k-degeneracy in the eigenvalues: now the single-particle state energy is linearly dependent on k and thus on the centre X'_k of the transverse wave function [see Eq. (2.7)]. Thus, an external potential causes the flat LLs to bend.

Now we can again calculate $\langle v_x \rangle$ and $\langle v_y \rangle$ using the unperturbed velocity operators from Eq. (2.5) and the new eigenstates from Eq. (2.6). Again, we have $\langle \psi'_{nk} | v_x | \psi'_{nk} \rangle = 0$ but now $\langle \psi'_{nk} | v_y | \psi'_{nk} \rangle = -v$. So, under a linear external potential in the $\hat{x}$-direction, the original eigenstates get shifted in the $\hat{x}$-direction and they carry a current in the $\hat{y}$-direction. We can understand v as the classical drift velocity $\vec{v} = \frac{\vec{E} \times \vec{B}}{B^2}$ of a particle experiencing both an electric and a magnetic field. The direction of the velocity is perpendicular to both fields. This is the essence of the QHE: a current in the $\hat{y}$-direction and a magnetic field in the $\hat{z}$-direction imply a electric field and thus a (Hall) voltage in the $\hat{x}$-direction. A way of calculating $\langle v_y \rangle$ without using the explicit eigenstates is by calculating the wave-packet velocity:

$$v_g = \frac{1}{\hbar} \frac{\partial \varepsilon}{\partial k}. \tag{2.8}$$

It can be easily verified using Eq. (2.7) that in the case of a linear potential Eq. (2.8) gives the same result $\langle v_y \rangle = -v$ if we use the perturbed energy from Eq. (2.7) for ε.

Lowest Landau level approximation

In the following, we will often fall back to the lowest Landau level (LLL) approximation when we study systems with a filling factor $\nu \leq 2$. This means that we will only consider the states in the lowest ($n = 0$) LL of the system *without* an external potential [see Eq. (2.3)] with wave functions:

$$\psi_{n=0,k}(x,y) = \frac{1}{\sqrt{\pi^{1/2} l_B L}} e^{iky} e^{\frac{1}{2l_B^2}(x+kl_B^2)^2}, \tag{2.9}$$

and consider them to be eigenstates of the system. In this thesis, when we only deal with LLL states and there can be no ambiguity, we leave out the index n in our notation.

In the LLL approximation, the eigenenergies ε_{nk} corresponding to these eigenstates are not always equal to $\frac{1}{2} \hbar \omega_c$. For a system with an external potential that varies with x, the single particle energy ε_k depends on the centre of the transverse wave function X_k and thus on k. In the LLL approximation, the calculation of the current is slightly paradoxical: the expectation values of the velocity operators in Eq. (2.5) with respect to the LLL basis-states both give zero. This because only states with more than one LL mixed into it have a non-zero expectation value of the velocity operators. However, the velocity calculated via Eq. (2.8) is non-zero since $\frac{d\varepsilon_k}{dk} \neq 0$. Hence, when we want to calculate the current in the LLL, we rely on the single-particle energy ε_k because this takes notice of the external potential while the LLL eigenstates do not.

13

We can quantify the size of the error in the LLL approximation in the case of a linear external potential. The $n = 0$ eigenstates in the case of a linear potential [see Eq. (2.6)] are of the same type (plane wave $\times$ harmonic oscillator state) as in the case without a potential [see Eq. (2.3)], only now the centres of the harmonic oscillator have been shifted. By comparing the wave function shift $\frac{eE}{m\omega_c^2}$ to the width of the transverse wave function $\sim l_B$ we say that the LLL approximation is justified when we have for the electric field:

$$E \ll \frac{\hbar^2}{me} \frac{1}{l_B^3}. \tag{2.10}$$

Even for non-linear external potentials, this condition makes sense because every non-linear potential can be written as a Taylor series that contains a linear component.

Edge channels in the naïve model

The reality is more complicated than a uniform electric field: the confining electric field is not constant across the sample and generally not even in the edge region. Figure 2.2 sketches the cross-section of a confined 2DEG in the naïve, non-interacting model. The external confining potential simply bends the originally flat LLs upwards at both edges. In the naïve model, the point where a bent LL intersects the Fermi level μ is referred to as an *edge channel*. This is where one can inject electrons into the system at low bias because there are low-lying empty states.

We can see in Fig. 2.2 that the number of edge channels on each edge is equal to the number of filled sub-LLs in the bulk.

In a system with an inhomogeneous density, the filling factor ν is a local quantity that varies from 0 at the edge to ν_0 in the bulk. In Fig. 2.2, ν is 0 all the way to the left. Further to the right, the filling factor jumps to 1 across the point where the spin-up band intersects the chemical potential, μ. The filling factor then jumps to its bulk value 2 across the point where the spin-down band intersects μ.

We do not know the exact eigenstates when the external potential looks more complicated (e.g. as in Fig. 2.2). Nevertheless, we still assume plane waves in the $\hat{y}$-direction that run along lines of constant potential energy [11] and localised wave functions in the $\hat{x}$-direction. These wave functions in the $\hat{x}$-direction will not be harmonic oscillator states anymore. However, as long as the external potential is more or less smooth ($El_B \ll \hbar\omega_c$, see Sec. 2.2.1), we expect these wave functions to be centred not too far away from their centres in the case without an external potential [see Eq. (2.3)].

We do not know the exact eigenenergies corresponding to the eigenstates either. However, we can at least say that the eigenenergy goes up as the centre of the wave function gets closer to the edge. Hence, we can say that the wave-packet velocity has opposite signs on opposite edges, and therefore there will be a chiral current flowing along the edges. The net $\hat{y}$-current transported by one sub-LL can be calculated by summing the group velocities of all occupied states labelled by k. Assuming the states are sufficiently closely spaced so that the local velocity differs smoothly from one state to the next, we can convert this sum to an integral:

$$I^y = \frac{-e}{L} \sum_k v_g(k) = \frac{-e}{L\Delta k} \int dk v_g(k) = \frac{-e}{h} \int dk \frac{\partial \varepsilon}{\partial k} = \frac{-e}{h} \int_{\mu_L}^{\mu_R} dk, \qquad (2.11)$$

In the equilibrium situation, the electrochemical potentials of the two edges, μ_R and μ_L (see Fig. 2.2), are equal, and the net current is zero: the current flowing in one direction at one of the edges cancels completely with the current flowing in the opposite direction at the opposite edge.

To have a net current, there should be a electrochemical potential difference $\Delta \mu = \mu_R - \mu_L$ between the edges as in Fig. 2.3. In this non-equilibrium case, the net $\hat{y}$-current carried by one sub-LL is given by:

$$I^y = \frac{-e\Delta \mu}{h}. \qquad (2.12)$$

A top view of our 2DEG with the edge states at $\nu_0 = 2$ is given in Fig. 2.4. The edge channels on top and at the bottom of the sample are respectively equilibrated with contacts 1 and 4 (indicated by the colours). If the electrochemical potentials of contacts 1 and 4 are different, there is a net $\hat{y}$-current [see Eq. (2.12)]. Note that the electrochemical potentials of contacts 1 and 4 respectively correspond to μ_R and μ_L in Figs. 2.2 and 2.3.

We can also write the electrochemical potential difference $\Delta \mu$ in Eq. (2.12) as eV_H, where V_H is the Hall voltage between the edges, so in the $\hat{x}$-direction. Every sub-LL contributes $I^y = \frac{-e^2}{h} V_H$ and the total current in the $\hat{y}$-direction is $I_{tot}^y = mI^y = m\frac{-e^2}{h}V_H$, where $m = \{1, 2, 3...\}$ is the number of contributing edge channels. The G_{xy} conductance of each sub-LL is precisely the conductance quantum $\frac{e^2}{h}$ and the total G_{xy} conductance
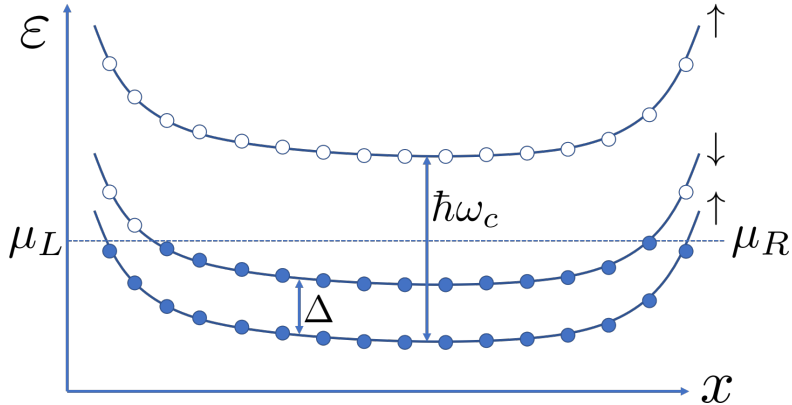
Figure 2.2: Sketch of the band-bending at the edge due to the confining potential in the naïve, non-interacting picture. The blue and white dots respectively represent filled and empty single-particle states. All single-particle states below μ are filled and the bulk filling factor ν_0 equal to 2.
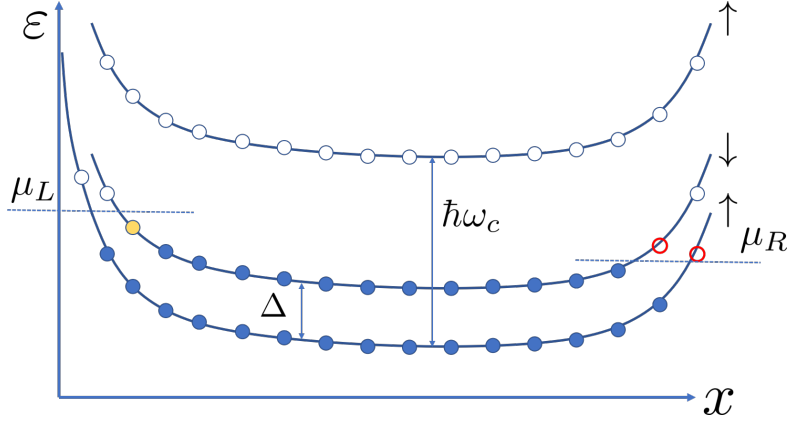
Figure 2.3: Cross-section of 2.4 just like 2.2 but now with biased edge channels $\mu_L \neq \mu_R$. The extra electron with respect to the equilibrium situation in Fig. 2.2 is depicted in gold and the removed electrons have a red outline. The positive y-direction is out of the page.
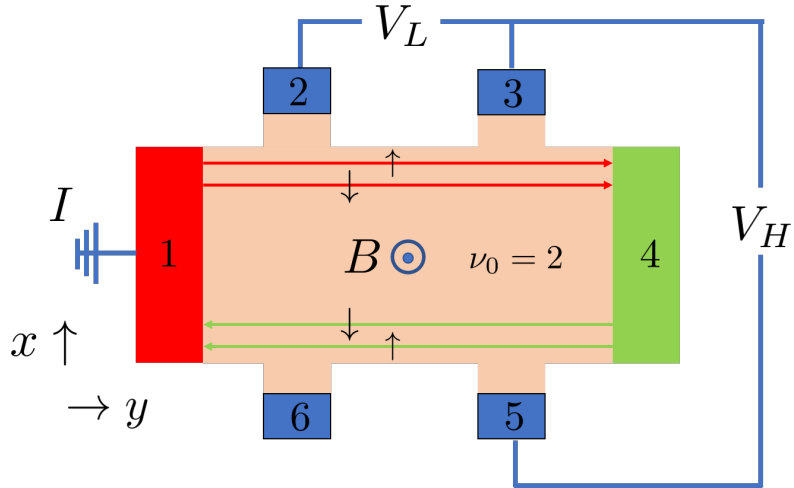
Figure 2.4: Top view of a 2DEG in the Hall bar geometry. The red and green lines are the chiral edge states that are respectively equilibrated with contacts 1 and 4. The bulk filling factor ν_0 is 2 and therefore there are two edge channels (spin-up and spin-down) on either edge. Figures 2.2 and 2.3 are cross-sections of this system, respectively in and out of equilibrium.

equals $m\frac{e^2}{h}$.

The essence of the quantum Hall effect is the following. We apply a bias between contacts 1 and 4 in Fig. 2.4 such that there is a current flowing in the $\hat{y}$-direction. When the system is in a quantised conductance state (on a plateau in the measurement

data in Fig. 1.2), we measure a non-zero Hall voltage between contacts 3 and 6, and a zero longitudinal voltage between contacts 2 and 3. This means that the current between contacts 2 and 3 is dissipationless ($R_{yy} = 0$). The explanation of the absence of dissipation in the edge channel picture is that the chirality of the edge channels blocks any backscattering, which is the mechanism causing dissipation. Considering for example a left-moving electron localised around a certain x-value in the sample of Figs. 2.2, 2.3, and 2.4, there is no empty right-moving state nearby where it can scatter to because these states are spatially well-separated from the filled left-moving states in the $\hat{x}$-direction.

Quantum phase transitions and disorder

When we change the electrochemical potential, the electronic density n_e (for instance, by depleting the sample with a gate) or the magnitude of the perpendicular magnetic field B, the filling factor ν also changes. When we are for example at $\nu_0 = 2$ in the bulk as in Fig. 2.2 and then increase B, we can push the spin-down sub-LL beyond μ so that we get $\nu_0 = 1$. This is the quantum phase transition from the quantised conductance $2\frac{e^2}{h}$ to $\frac{e^2}{h}$.

However, ν_0 can be non-integer in reality and it turns out that we can observe the quantised conductance $G_{xy} = m\frac{e^2}{h}$ not just for extremely fine-tuned values of n_e and B, but over a finite width in B and n_e (see the plateaus in Fig. 1.2). This allows the actual observation of these quantum phases. The missing ingredient in our discussion thus far that allows for these finite-sized plateaus is disorder.

Disorder localises some of the LL states and gives them energies that spread into
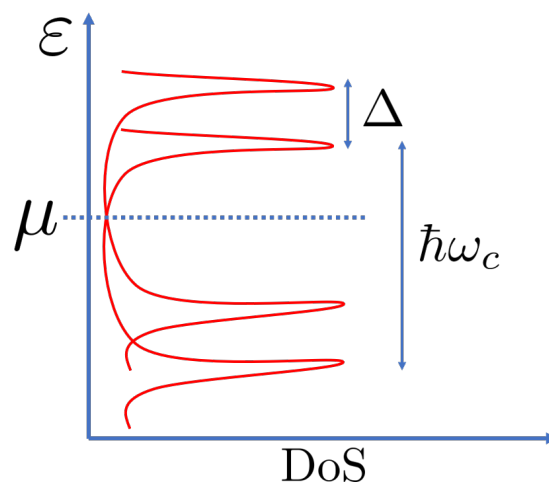

Figure 2.5: The DoS profile of the 2DEG with a perpendicular magnetic field. The Zeeman energy splits the LL-peaks (dashed grey) into two sub-LL-peaks (red). The broadening of the peaks is due to disorder. The electrochemical potential μ is positioned such that $\nu = 2$.

the energy gaps between the LLs. This allows μ to be varied smoothly with the density n_e [11]. Disorder thus broadens the - previously infinitely sharp - LL peaks in the DoS as in Fig. 2.5. States at the centres of the LL peaks maintain their de-localised character and contribute to the current. However, states that sit in between the centres of the LL peaks do not affect the current or the quantised conductance because they are strongly localised. This allows us to observe the quantised conductance $G_{xy} = m\frac{e^2}{h}$ over a plateau of finite width in B or n_e, so also when $\nu_0 = \frac{n_e h}{eB}$ is not exactly an integer [11]. To accurately measure the QH conductance for metrological purposes, a fair amount of disorder that gives wide plateaus is even required [3].

In Fig. 1.2 we can see that during the transition between two resistance (conductance) plateaus, the longitudinal resistance becomes non-zero. In the naïve edge channel model for the finite Hall bar-like sample that we have discussed thus far, this is explained as follows. When we start in the $m = 2$ phase and lower the magnetic field, at some point the third sub-LL will intersect the chemical potential. Figure 2.6 shows that this creates two additional edge channels. Note that this representation does not show any disorder states with energies between the LL peaks. The two new edge channels are spatially not well-separated from each other. When we bias the system slightly so that $\mu_L > \mu_R$ and there is a (Hall) potential across the sample $V_H \neq 0$, electrons in the innermost edge channel can backscatter as indicated by the red arrow. Backscattering means a current in the $\hat{x}$-direction and a non-zero longitudinal resistance R_{yy}. Because electrons are leaking away from the edge channel, the perfect quantisation of the Hall conductance is destroyed. When we lower the magnetic field even further, the spatial separation between the innermost edge channels increases, the backscattering stops, and we have arrived at the $m = 3$ plateau.
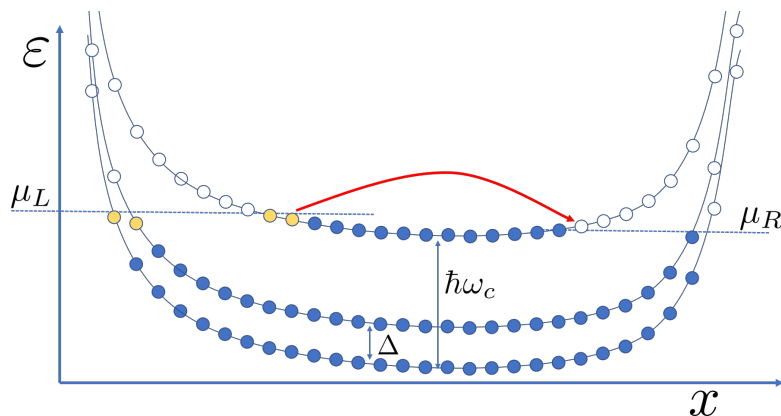

Figure 2.6: Cross-section of a QH system during the transition between the $m = 2$ and $m = 3$ phase according to the naïve model. There are some extra electrons on the left side compared to the right side (because $\mu_L > \mu_R$) which are depicted in gold.

Fractional quantum Hall effect

When the magnetic field is increased beyond the $m = 1$ conductance plateau, more plateaus appear that correspond to fractional filling factors. For example, the $m = \frac{1}{3}$ plateau for ν_0 around $\frac{1}{3}$. For the FQHE, we still have the relation $G_{xy} = m\frac{e^2}{h}$. In the $m = \frac{1}{3}$ state, the lowest sub-LL is only filled for one third. The robustly quantised conductance can only be explained by the interactions between the electrons and the electrons' collective behaviour. The FQH system has remarkable properties, such as fractionally charged quasi-particles.

The next step towards a more realistic model of the edge, even for the integer case, is the inclusion of interactions between the electrons.

2.2.2 The CSG model

In 1992, Chklovskii, Shklovskii and Glazman (CSG) made an important step towards a model of the edge that includes interactions [12]. Their motivation was that when assuming a smooth confining potential, the naïve model does not predict the correct scattering rates between biased edge channels (see Sec. 2.3) because it overestimates the spatial separation between occupied and empty states. Based on work by Beenakker [15] and Chang [16], it was known that the modification of the 2DEG DoS due to the perpendicular magnetic field (Fig. 2.1b) leads to a landscape of compressible and incompressible strips. The compressible strips have a large DoS, behave metallically, and have good screening properties. The incompressible strips have a low DoS and hence poor screening properties. Chklovskii, Shklovskii and Glazman took this concept further. They calculated the positions and widths [see Eq. (2.14)] of these strips using a (quantum) DoS for a QHE system without disorder as in Fig. 2.1b and classical electrostatics. The latter means that only the Hartree term is considered for the e-e interactions.
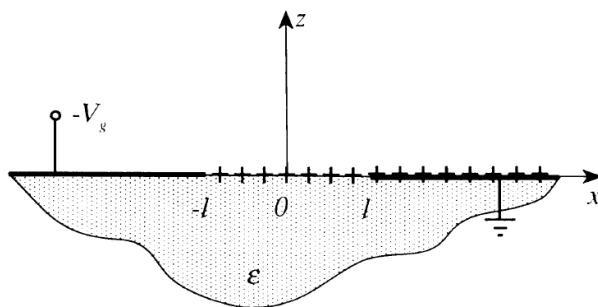
Figure 2.7: Geometry of the electrostatic problem solved by Chklovskii, Shklovskii and Glazman. Plusses represent the jellium background. The dotted area represents the semiconductors that sandwich the 2DEG. Figure from reference [12].
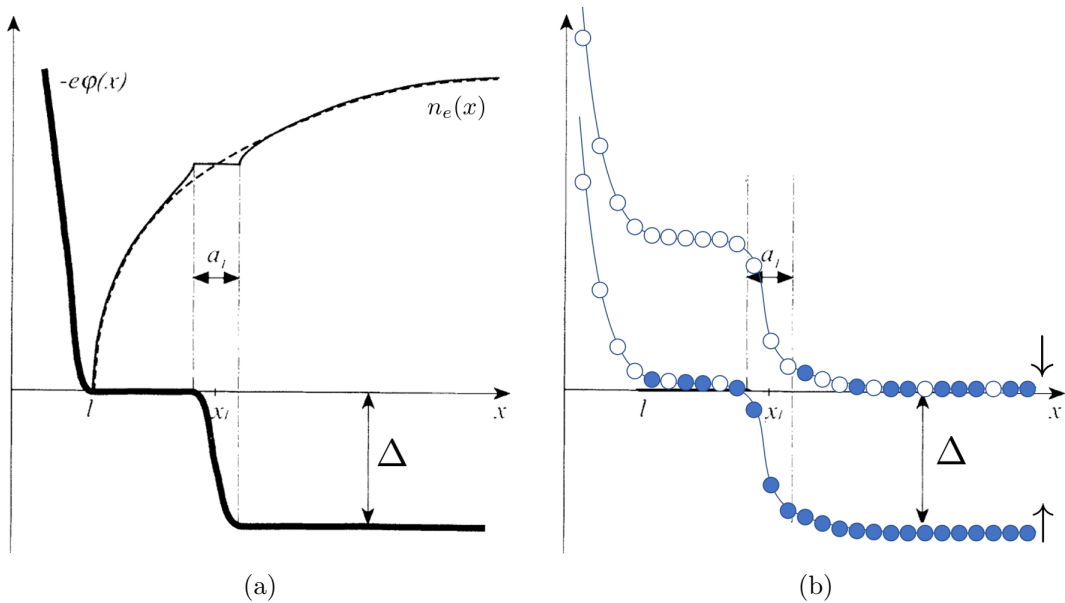
Figure 2.8: (a) Edge of a 2DEG with $\nu_0 = 1.5$. The thin solid line is the electron density and the thick solid line is the total potential. The coordinate x_1 is the position of the centre of the first IS. Adapted from [12]. (b) The bands and their filling corresponding to the left panel. Note that the electron density increases as we move towards the bulk (right).

The geometry of the system they consider lies in the (x, y) plane and is thus two-dimensional. Figure 2.7 shows the geometry from left to right: the gate set to a voltage $-V_g$, the depleted region of width $2l$, and the region where the electron density gradually increases from 0 to its bulk value n_0. Because of the translational invariance in the $\hat{y}$-direction, the problem becomes effectively one-dimensional. The half-width of the depleted region l is given by:

$$l = \frac{V_g \epsilon}{4\pi^2 n_0 e},$$
(2.13)

where ϵ is the dielectric constant which is assumed to be 12 throughout this thesis. Typical values for l are reported to be around 250 nm, both for edges defined by gates and chemical etching [12].

The appearance of compressible and incompressible strips in the CSG model is best explained by looking at the edge of a 2DEG with bulk filling factor $\nu_0 = 1.5$. For this case, Fig. 2.8 shows the electron density $n_e(x)$ and the total potential $\phi(x) = \phi_{ext}(x) + \phi_{ee}(x)$, i.e., the external potential $\phi_{ext}(x)$ plus the mean-field potential due to the e-e interactions $\phi_{ee}(x)$. The circles in the right panel of Fig. 2.8 represent the single-particle states. The vertical coordinate is the total single-particle energy $-e\phi(x) + \frac{1}{2}\omega_c \pm \frac{1}{2}\Delta$ associated to a state. This energy depends on the filling of the other states (see Sec. 2.2.4). The electrochemical potential μ of the 2DEG electrons coincides with the vertical coordinate

20

where the axes intersect. From $x = -l$ to $x = l$, the electron density is zero because the 2DEG is fully depleted. In this region, the total potential drops quickly due to the positive ionic background. When the external potential has dropped sufficiently such that the total potential plus the lowest (spin-up) sub-LL energy $-e\phi(x) + \frac{1}{2}\omega_c - \frac{1}{2}\Delta$ equals μ at $x = l$, we have electrons with sufficient energy to be in this region. Hence, $n_e(x)$ becomes non-zero. Because of the large DoS (see Fig. 2.1b), the density $n_e(x)$ would jump if it were not for the interactions. The electrons cannot all sit next to each other because this would increase the total potential and push $-e\phi(x) + \frac{1}{2}\omega_c - \frac{1}{2}\Delta$ beyond μ again. The only way to accommodate all the electrons at the same energy in a sub-LL, is by letting the density $n_e(x)$ increase as we move towards the bulk (see Fig. 2.8). This gradual increase of $n_e(x)$ ensures that the e-e interaction potential screens out the external potential, creating a strip with a flat total potential. On the right side of the flat strip in Fig. 2.8, the electron density is larger, and the electrons experience larger interaction energy than on the left side. However, the external potential drops from the left of the strip to the right due to the positive background. These energy differences cancel each other, and the result is a total potential that is flat. Because the electron density can vary within this strip, we call it *compressible*.

This increase of the density within the first sub-LL cannot go on forever as we move towards the bulk because when $n_e(x) = n_L$, the spin-up sub-LL is completely filled: $\nu = 1$. At this point, the DoS drops to (almost) zero (see Fig. 2.1b), and the electrons are not able to screen out the external potential any more. The total potential drops across this strip. Because the cannot vary within this strip, we call it *incompressible*. When the total potential $\phi(x)$ has dropped by an amount Δ, the energy of the electron states in the second (spin-down) sub-LL: $-e\phi(x) + \frac{1}{2}\omega_c + \frac{1}{2}\Delta$ equals μ and electrons start filling this second sub-LL. Here, the DoS is high again, and we get a second compressible strip where the total potential is flat. Note that the spin-down sub-LL only becomes half-filled as we assumed $\nu_0 = 1.5$ for the example shown in the figure.

In the CSG model, the screening in the compressible strips is assumed to be perfect. Hence, the compressible strips are perfectly flat. Although we also assume flat bands in many of our calculations in chapter 4, we note that in reality, the screening might not be perfect and that at non-zero temperature, the compressible strips attain a finite slope [17]. In general, the incompressible strips are much more narrow than the compressible strips [12]. In the CSG model, the width of the *first* incompressible strip width a_1 can be expressed as:

$$a_1^2 = \frac{8\epsilon l \Delta}{\pi^2 e^2 n_L} \frac{\nu_0^2}{(\nu_0^2 - 1)^2}.$$ (2.14)

Current

Much of the discussion about current and disorder from the previous section also applies here. In the CSG model, the current is carried by the sloped incompressible strips [3, 16]. However, Chklovskii et al. seem to define the compressible strips at the edge

as 'edge channels'. The compressible strips are the regions where one can add electrons to the system or take them out of the system at low bias. Adding an electron to the compressible strip increases the electrochemical potential μ. Each electron present is given a slightly higher energy from the mean-field e-e interactions with the extra electron. The consequence of this is that the compressible strip is shifted up in energy, making the energy drop over the incompressible strip larger. A larger energy drop means more current flow in the incompressible strip [see Eq. (2.12)]. So, both the compressible and incompressible regions, which can cover the entire bulk, are involved in producing a net current in the sample. Because the nature of the CSG 'edge channels' is so different from those in the naïve model, we often refer explicitly to the compressible and incompressible strips instead of the vaguer 'edge channels'.

We see from Eq. (2.14) that the first incompressible strip becomes wider as ν_0 gets closer to 1. When ν_0 equals 1, the incompressible strip width diverges. What happens here is that the widened incompressible strips from opposite edges merge and that the whole bulk becomes incompressible. The same happens for the kth incompressible strip when $\nu_0 = k$ [12]. Here we see that already in the CSG model, the notion that the current is being carried purely at the edges breaks down.

The innermost incompressible strip is always the widest. For good quantisation of the conductance, the Hall voltage drop has to happen entirely over the innermost incompressible strip [3]. For Hall conductance plateaus with conductance greater than $\frac{e^2}{h}$, this means that the compressible strips at each edge have to be equilibrated. Figure 4 and the accompanying discussion in the paper by Weis and von Klitzing provides an excellent explanation of this.

Quantum phase transitions

Due to disorder, we measure conductance quantisation over a finite width in the magnetic field. Weis and von Klitzing note that in the CSG model, the high and low magnetic field sides of the conductance plateau are different [3].

To explain this, we take the $m = 2$ conductance plateau. At the high magnetic field side of the plateau, the bulk filling factor ν_0 is close to 2 (see left panel of Fig. 2.9). Weis and von Klitzing take this regime to be from $\nu_0 = 1.95$ until $\nu_0 = 2.1$. At this side of the plateau, the bulk is incompressible and insulates both edges from each other. Hence, there is no backscattering possible through the bulk, and the Hall conductance is quantised. When the magnetic field is made larger, the two innermost compressible strips become wider, and the incompressible bulk shrinks. At $\nu_0 = 1.95$, the two compressible strips merge and form a compressible bulk. Backscattering through the bulk destroys the perfect quantisation and makes the longitudinal resistance non-zero: we are in the window between two plateaus. At even larger magnetic fields, the first incompressible strip a_1 at each edge becomes wide enough to insulate the outer compressible strip from the bulk: the system is in the phase corresponding to the $m = 1$ conductance plateau.

At the low magnetic field side of the plateau, the bulk filling factor is larger than 2 (see right panel of Fig. 2.9). Weis and von Klitzing take this regime to be from $\nu_0 = 2.1$

until $\nu_0 = 2.5$. In this case, states in the third sub-LL peak are occupied in the bulk, and hence the bulk is compressible. The two innermost incompressible strips (a_2) are well localised at the edges. If the magnetic field is not too low ($2.1 < \nu_0 < 2.5$), these strips are still sufficiently wide to insulate the compressible strip(s) at the edge from the compressible bulk and thus prevent backscattering through the bulk. If we lower the magnetic field further ($\nu_0 > 2.5$), these inner incompressible strips become so narrow that they lose their insulating property. Backscattering through the bulk takes off, and the Hall quantisation is destroyed. Lowering the magnetic field yet a bit more fills up the next sub-LL in the bulk. This makes the bulk incompressible again, stops the backscattering, and brings us to the $m = 3$ conductance plateau.

(a)

(b)

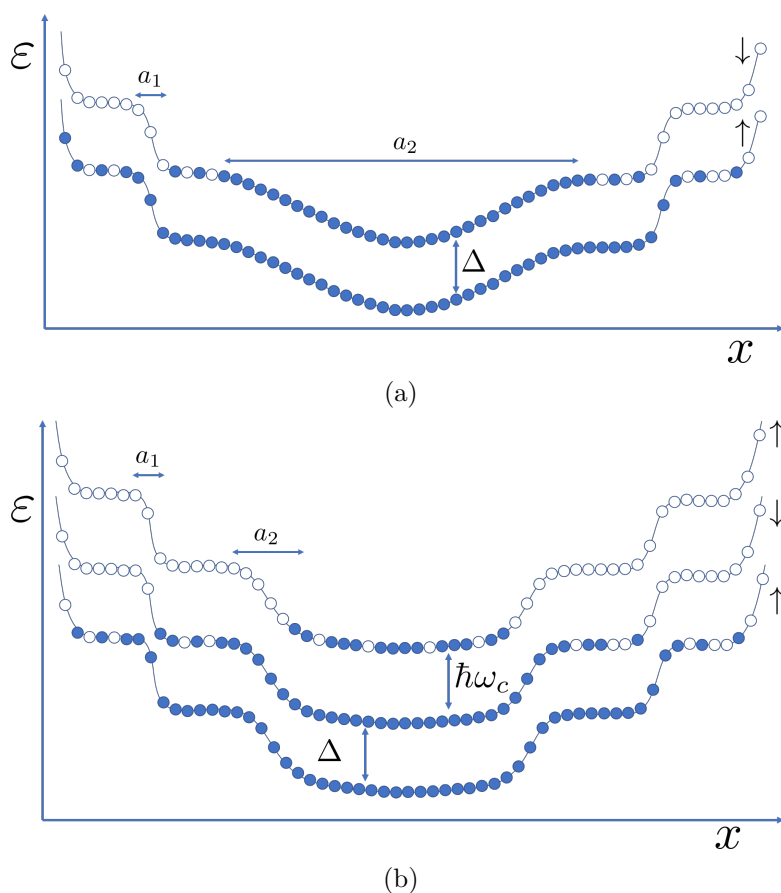Figure 2.9: Schematic picture of the band structures corresponding to the high (a) and low (b) magnetic field side of the second conductance plateau. The widths of the first and second incompressible strip are respectively indicated by a_1 and a_2. Note that again, the localised states in between the LLs are not displayed for simplicity. In reality, $\hbar\omega_c$ is usually much larger than Δ.

In general, the QHE is more robust on the high magnetic field side of the conductance plateau because the quantisation is protected by an insulating, incompressible bulk [3].

As mentioned before, the CSG model is based on classical electrostatics (Hartree interaction) and does not include quantum effects like exchange (Fock interaction). The third and last model that we introduce is an interacting model that also includes the exchange interaction between the electrons.

2.2.3 Model including exchange

The primary effect of exchange in a system in the QHE state is that it can enhance the spin-splitting between sub-LLs. The exchange-enhancement of the spin-splitting is a quantum effect that originates from the Coulomb interaction. It is best understood by looking at a system of two electrons in a finite system. Electrons are fermionic spin $\frac{1}{2}$ particles, and the many-body wave function of the system should therefore be anti-symmetric and has both a spatial and a spin part. The electron spins can either be aligned or opposite, which respectively corresponds to a symmetric and an anti-symmetric many-body spin-state. If the many-body spin-state is symmetric, the spatial state should be anti-symmetric and vice-versa. In a symmetric spatial state, the probability distribution (the absolute square of the wave function) is such that the particles are generally closer together than in the anti-symmetric spatial state. The symmetric and anti-symmetric wave functions respectively correspond to the molecular bonding and anti-bonding orbitals. When the two charged electrons are on average closer together, this leads to a larger Coulomb interaction energy. Hence, it saves Coulomb energy for the electrons to be in a symmetric spin state because this implies an anti-symmetric spatial state.

This same principle holds for systems with more than two electrons, such as our 2DEG. When the system is in some degree spin-polarised (let us say in the spin-up direction), and we add an extra electron to the system, it is energetically more favourable for this electron to also be in the spin-up state than to be in the spin-down state. This is because being in the spin-up state allows the extra electron to avoid the other electrons more, saving Coulomb energy. This effect increases the energy difference Δ between the spin-up and the spin-down band to beyond the Zeeman-splitting E_z. We say that the exchange effect enhances the spin-splitting. A popular way of incorporating enhancement of the spin-splitting in a model is by assuming an enhanced g-factor in the Zeeman-splitting: $\Delta = g^*\mu_B B$. The *significance* of the exchange-enhancement depends on the strength of the Coulomb interaction relative to the bare spin-splitting.

Exchange-enhancement of the spin-splitting only plays a role when the system is locally polarised. Hence, we expect the exchange-enhancement of the spin-splitting to be maximal in regions with odd filling factors [18, 19, 20]. For instance, as we approach the edge, ν drops to 1 at some point (see Fig. 2.8). Only the spin-up band is fully filled at this filling factor, and we expect a strong exchange-enhancement. Figure 2.10 shows a schematic picture of the edge where we can see this effect.

The study of exchange-enhancement of the spin-splitting goes back to the 1970s,
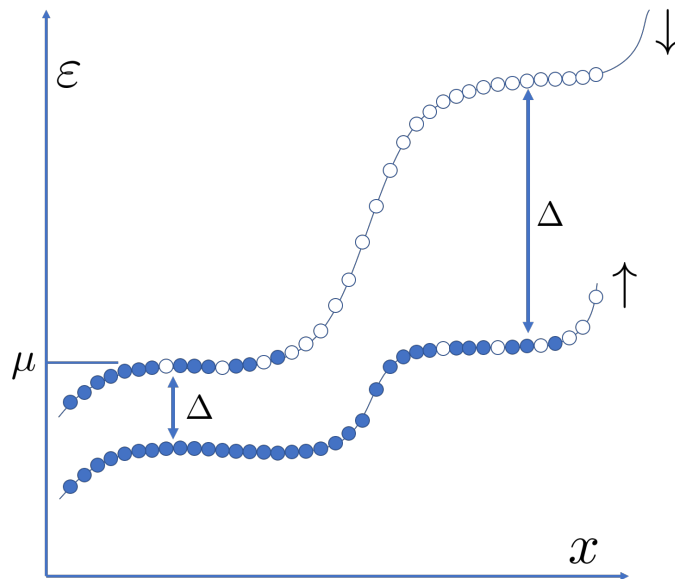
Figure 2.10: Picture of the edge that illustrates the exchange-enhancement of the spin-splitting that is especially strong in regions with an odd-integer filling factor.

when Ando et al. predicted the enhancement and oscillation of the g-factor in a MOS inversion layer on a Si(100) surface [19]. Since then, several studies have reported an enhanced spin-splitting using different methods. We will highlight a few of these studies.

By studying the temperature dependence of the Shubnikov - De Haas oscillations, Englert et al. [18] determined an enhanced and oscillating g-factor g^* of up to 2.6 in a GaAs/GaAlAs 2DEG.

Dolgopolov et al. [21] measured the (bulk) spin-splitting by a capacitance technique. They found an enhanced g-factor of $g^* \approx 5.2$ to describe the data. The dependence of the spin-splitting on the magnetic field was found to be linear.

Experiments using the coincidence technique [22] and activation energy measurements [22, 23] also found a strong enhancement of the spin-splitting of up to $g^* = 7$.

Dixon et al. [9] and Sukhodub et al. [24] extract the spin-splitting from the scattering between biased edge states (see Sec. 2.3). They find little to no enhancement of the spin-splitting.

Rijkels and Bauer [25] theoretically studied the 2DEG edge using the Hartree-Fock (HF) approximation. Amongst other things, they found an exchange-enhancement of the spin-splitting of about a factor 50 compared to the bare spin-splitting. They mention that the HF approximation might overestimate the exchange enhancement. We later in this thesis also reflect on this ourselves when we perform a HF analysis (see Sec. 3.1.1).

More recently, theoretical studies by Oswald and Römer [26], and Werner and Oswald [27] also used the HF approximation and showed that exchange drastically affects the structure of the edge.

All in all, there seems to be no consensus on how the exchange interaction changes

the edge structure. The experimental and theoretical results vary a lot between the different methods used.

2.2.4 Implementation of the interacting models

In a fully-interacting many-body model, it is in a sense meaningless to associate energies to single-particle states in the system. If we add, remove, or relocate a single electron (e.g. in the case of scattering) in the many-body state, all these 'single-particle energies' and the many-body ground-state configuration would change.

It is convenient to deal with a non-interacting system with well-defined single-particle energies from a practical point of view; for example, when using Fermi's golden rule [see Eq. (3.5)] for the calculation of a scattering rate.

Mean-field methods (see appendix B) show a landscape of alternating compressible and incompressible strips, which differs significantly from the naïve edge picture. In the CSG and exchange models, we take this mean-field edge structure and the corresponding electron density seriously but then assume that it is made up of electrons with well-defined single-particle energies. Each of these single-particle energies is a sum of the LL energy, the Zeeman splitting, the external potential, and the mean-field (Hartree-only or Hartree-Fock) e-e interaction energy.

The single-particle states are depicted by filled and empty circles, for example, in Fig. 2.8. During the derivation of the scattering rates (see chapter 3), we will not consider changes to the initial single-particle energy landscape due to the relocation (scattering) of electrons. In that sense, we consider the electrons to be non-interacting.

Concluding, the CSG and exchange models, especially in the way we use them in the continuation of this thesis, do not take all aspects of the e-e interaction into account. Of course, it would be better to consider more aspects of the e-e interaction, especially when modelling a FQH system wherein interactions dominate. However, other pictures, such as the Luttinger liquid picture [28, 29], are more suited for this.

2.2.5 Conclusion

In this section, we have presented three models of the edge of a confined 2DEG: the non-interacting naïve model, the CSG model, and the exchange model. The three models give rather different pictures of the edge, as can be seen in Figs. 2.2, 2.8, and 2.10.

In the next section, we see what happens if neighbouring edge channels at one edge carry different electrochemical potentials. In chapter 3, we discuss the non-equilibrium versions of the three models presented in this section.

2.3 Edge channel scattering

Since the early 1990s, experiments have been carried out that study the scattering between edge channels that run along the same edge [30, 31, 32, 33]. In this thesis, we
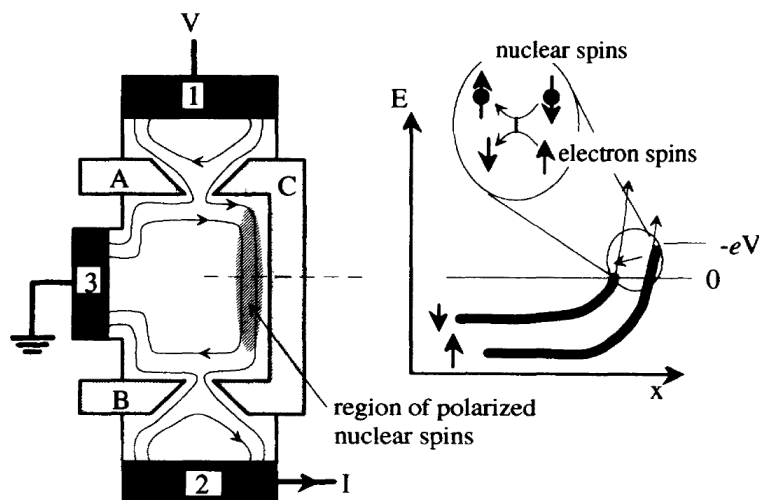
Figure 2.11: Left panel: the device geometry of the Wald et al. experiment [8]. The thin lines indicate the edge channels; A, B, C are gates that define the two QPCs and 1,2,3 are Ohmic contacts. Right panel: Band-structure of the edge in the scattering region in the case that $\mu_1 > \mu_3$ (reverse bias). Figure from [8].

focus on the slightly later experiments about the spin-flip scattering between the lowest two sub-LLs: the spin-up and spin-down sub-LL of the LLL [34, 8, 9].

The Müller et al. [34], Wald et al. [8], and Dixon et al. [9] experiments were all performed in dilution fridges at respective base temperatures of 100, 50, and 30 mK.

The use of gates makes it possible to let two edge channels meet that originate from different contacts and can thus be filled up until different electrochemical potentials. Figure 2.11 illustrates such a sample geometry. The gates A, B, and C, define two quantum point contacts (QPCs). Under the gates, the 2DEG is fully depleted and in the region between respectively A and C, and B and C, the depletion is such that only the spin-up edge channel can flow through. Before any equilibration occurs, all edge channels 'carry' the electrochemical potential of the contact they originate from. For instance, the edge channels that originate from the Ohmic contact 1 are filled up until the electrochemical potential μ_1. Between the QPCs, there is a *scattering region* with a spin-up channel at μ_1 and a spin-down channel at μ_3.

In the Wald et al. set-up, contact 3 is grounded. When contact 1 is *reverse* biased such that $\mu_1 > \mu_3$, we expect equilibration by scattering from spin-up to spin-down (right panel of 2.11). At *forward* bias, we expect electron scattering from spin-down to spin-up. When an electron scatters from one spin-polarised edge channel to the other, it has to flip its spin. Because the total angular momentum (and thus also spin) is conserved, some mechanism has to 'absorb' this difference in the electronic spin.

Some studies have assumed the spin-orbit coupling to be the mechanism behind the interedge spin-flip scattering [34, 35] and others the hyperfine interaction [8, 9]. The (contact) hyperfine interaction [see Eq. (2.15)] is the coupling between the electronic

27

spin $\vec{S}$ and the nuclear spin $\vec{I}$. It allows an electronic spin-flip by a simultaneous nuclear spin flip (illustrated in the right panel of 2.11). The contact hyperfine interaction,

$$A\vec{I} \cdot \vec{S} = \frac{A}{2}(I^+ S^- + I^- S^+) + A I_z S_z, \qquad (2.15)$$

can be written as the sum of two flip-flop terms - $I^+ S^-$ flops the nuclear spin up and simultaneously flips the electronic spin down and $I^- S^+$ does the opposite - and an energy-splitting term. This last term produces the so-called Overhauser shift in the electron energies. The electronic spin-scattering dynamically polarises the nuclei (DNP).

The experiments by Wald et al. [8] and Dixon et al. [9] both found evidence for the contact hyperfine origin of the scattering via hysteretic IV curves (Fig. 2.12) and nuclear magnetic resonance (NMR) data. Some of the same people were involved in both experiments. The main difference is that Wald et al. used fully depleted QPCs (see Fig. 2.11) while Dixon et al. used partially depleted QPCs that should reduce unintended scattering (see Sec. 2.3.1).

Wald et al. explain the hysteresis in the IV curves with the flip-flop terms in Eq. (2.15). In the reverse bias case, nuclei flop from down to up as electrons scatter from up to down. In the positive bias case, it is the other way around. When we scan to negative bias coming from positive bias, the scattering at positive bias has created a population of down-polarised nuclei $\langle I_z \rangle < 0$ around the edge channel. This nuclear polarisation leaks away due to diffusion but this is a slow process due to the weak dipole-dipole coupling between nuclei [36]. Therefore, the downward polarisation will survive for some time once the sweep has reached negative bias. The excess availability of downward polarised nuclei enhances the flip-flop scattering compared to a scan coming from the negative bias side. Because the same story holds for positive bias, the hysteresis is symmetric, as shown in their Fig. 2 [8].

Three years later, Dixon et al. observed *asymmetric* hysteresis (see Fig. 2.12) and argued that it is the energy splitting term $A I_z S_z$ in Eq. (2.15) that causes this, and not the flip-flop terms. The spin-flip scattering induces a polarisation $\langle I_z \rangle \neq 0$ in the vicinity of the edge channel. If we assume a positive sign for the hyperfine coupling constant A, a positive nuclear polarisation $\langle I_z \rangle$ reduces the existing energy splitting between the spin-up and spin-down band Δ at the edge. In contrast, a negative $\langle I_z \rangle$ makes Δ larger. A smaller spin-splitting brings the occupied and empty states closer together in both the naïve model and the CSG model [see Eq. (2.14)] and thus leads to more scattering.

A positive nuclear polarisation $\langle I_z \rangle > 0$ is created at negative bias. Hence, when we sweep from negative to positive bias, there is more scattering than from positive to negative bias (compare the two sweep directions in Fig. 2.12). This hysteresis is asymmetric.

Because the Dixon et al. experiment has especially inspired our calculations in chapters 3 and 4, we discuss it in more detail below.
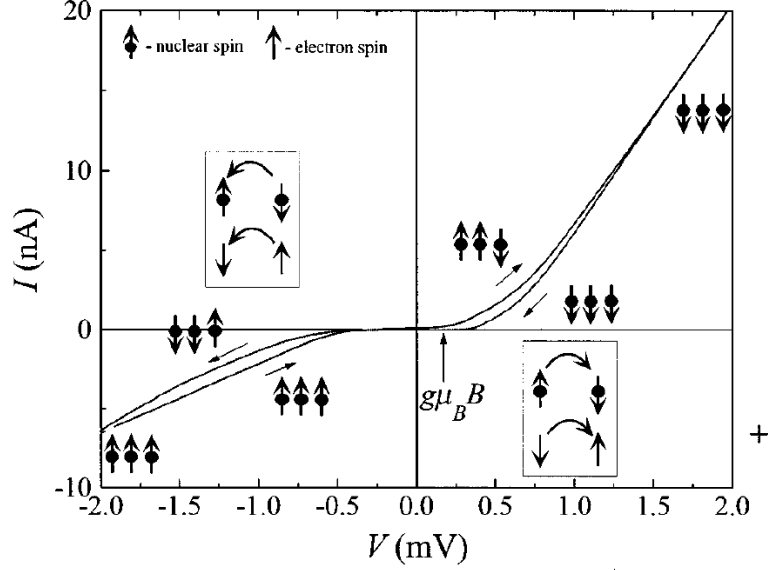
Figure 2.12: IV curve from the Dixon experiment [9]. Note that the current is the *scattering* current measured at contact 3 (seeFig. 2.13).

2.3.1 Experiment Dixon et al.

The experimental set-up in the Dixon et al. experiment (see Fig. 2.13) is similar to the one in the Wald et al. experiment. An important difference is that in the Dixon et al. set-up, they measure the current that is scattered, while in the Wald et al. set-up, they measure the current that has passed through without scattering. Another difference is that the B and C gates in the Dixon et al. experiment are not fully depleted but are tuned to $\nu = 1$ so that one edge channel flows through. This makes the QPCs effectively much wider and is supposed to reduce unintended scattering between the μ_1 and μ_3 spin-down bands, and between the μ_1 and μ_3 spin-up bands (see Sec. V in Dixon et al. for a more extensive discussion). They attribute it to this difference that the hysteresis they observe is asymmetric and not symmetric as in the Wald et al. experiment.

The authors also report a threshold voltage V_t for positive bias, indicated by the arrow in Fig. 2.12. They explain this threshold using the non-equilibrium CSG model, which will be dealt with in detail in Sec. 3.1. All we need to know here is that under forward bias, the a_1 incompressible strip shrinks [37] (see Fig. 3.3c in Sec. 3.1.1). However, when $\Delta\mu = \mu_3 - \mu_1 < \Delta$, where Δ is the (possibly enhanced) spin-splitting, the occupied spin-down states are still well spatially separated from the empty spin-up states to which they could scatter. Because of this separation, there is little overlap between the transverse wave functions. The scattering is thus weak. When $\Delta\mu = \Delta$, the incompressible strip width a_1 disappears, and the spin-down electrons can easily redistribute to the vicinity of available spin-up states. At this point, the scattering current grows rapidly. Thus, the condition $eV_t = \Delta\mu = \Delta$ defines the threshold voltage
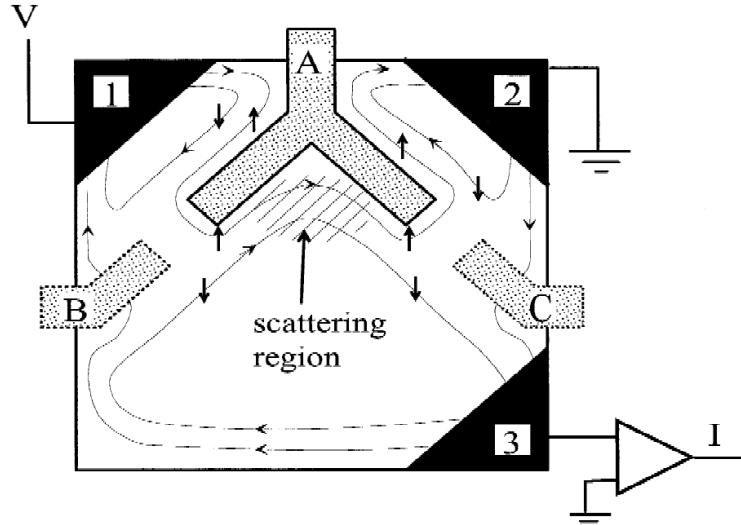
29

Figure 2.13: The device geometry of the Dixon experiment [9].

V_t and this is also the way they deduce the spin-splitting Δ from the measurements.

According to the authors, there is no such threshold for negative bias. According to the CSG model, there should not be a threshold at negative bias because the band-structure never changes as radically as in the positive bias case (see Fig. 3.3b in Sec. 3.1.1). The IV curve in Fig. 2.12 indeed shows different behaviour for positive and negative bias. However, the difference is not as dramatic as expected from the theoretical model. For negative bias, there even seems to be a threshold voltage.

Another peculiarity we observe in the paper is that the reported electronic density n_e is 2.5×10^{11} cm^{-2} while the authors state the bulk filling factor ν_0 to be 2 at $B = 7$ T. However, at this magnetic field, the density for one filled sub-LL n_L is 1.7×10^{11} cm^{-2}. Hence, the reported electronic density, together with the reported field value of 7 T, gives a *bulk* filling factor ν_0 of 1.4. Furthermore, the authors mention that according to the CSG model, the width of the first incompressible strip a_1 [see Eq. (2.14)] is around 7 nm. However, assuming $l \approx 250$ nm, we can only reproduce this result if we base ourselves on the reported values for the magnetic field and electronic density, and disregard $\nu_0 = 2$. We conclude that the reported filling factor, electronic density, and magnetic field are inconsistent.

If the experiment were carried out at $\nu_0 = 1.4$, the theoretical picture would be different in several ways. The bulk would have been mostly compressible as in Figs. 2.8 and 2.9b, and the sample might not even have been in a plateau state [3]. Because the first incompressible strip [see Eq. (2.14)] is wider at $\nu_0 = 1.4$ than at $\nu_0 = 2$, the scattering rate (see chapter 3) would be greater. The non-equilibrium pictures (see Fig. 3.3) and thus the voltage dependence of the scattering rate are also expected to be different.

Parameter	Symbol	Value
2DEG density	n	2.5×10^{11} cm^{-2}
Magnetic field	B	7 T
Magnetic length	l_B	9.7 nm
(bare) g-factor	g	-0.44
Zeeman splitting	E_z	0.18 meV
Spin-splitting	Δ	0.27 meV
Cyclotron splitting	$\hbar\omega_c$	11.3 meV

Table 2.1: Values of parameters in the Dixon et al. experiment [9].

In Sec. 2.2.3, we discussed the enhancement of the spin-splitting due to the exchange interaction effect. Assuming that there indeed is a correspondence between the threshold voltage V_t and the spin-splitting Δ, the observed enhancement of the spin-splitting is very small in the Dixon et al. experiment: they measure $\Delta = 0.27$ meV while $E_z = 0.18$ meV. Hence the enhancement could be described by an enhanced g-factor $g^* = 1.5g$. So either this assumption is wrong, or there is really only a very slight enhancement of the spin-splitting. Table 2.1 contains an overview of the parameters of the Dixon et al. experiment. When we make certain estimates later in this thesis, we will often use these values.

In order to measure maximal hysteresis, Dixon et al. let the system dwell at either a large negative (-1 mV) or a large positive (1 mV) bias for 60 s. They then quickly ramped the bias to a specific value to measure the current at that bias before setting it back to the dwelling bias. The IV curves measured in this fashion (see Fig. 4 in their paper) show a hysteretic shift comparable to the threshold voltage. They calculated the Overhauser field - the effective field due to the polarised nuclei - to be 4 T, close to its maximum value. This means that the nuclei in the vicinity of the edge become almost fully ($\approx 85\%$) polarised during this dwelling procedure.

When we look at the IV curve in Fig. 2.12, we see that the current at -1 mV is around -2 nA. For full ballistic conductance (one channel), the scattering current would be zero and the non-scattered current (measured at contact 2) would be $I_2 = \frac{e^2}{h}V = -38.7$ nA. Hence, a scattering current of -2 nA means that $\approx 5\%$ of the current is scattered. A scattering current -2 nA means that 2 nC of charge is scattered per second, this corresponds to 1.2×10^{10} electrons per second. Hence, to explain the scattering current at -1 mV, the *scattering rate* Γ between spin-up and spin-down states should be 1.2×10^{10} s^{-1}. For $+1$ mV, the scattering current is around $+6$ nA, which corresponds to a scattering of $\approx 15\%$ of the total ballistic current, and a scattering rate of 3.7×10^{10} s^{-1}.

In the next chapter, we set up the calculation for the scattering rates at both forward and negative bias using the models we introduced in this chapter.

Chapter 3

Set-up and derivation of scattering rates

As we have seen in the previous chapter, equilibration occurs when two edge channels that carry a different electrochemical potential meet.

This chapter introduces the non-equilibrium versions of the edge models that we introduced in Sec. 2.2. We then set up the calculation for both the elastic and inelastic scattering rate within the different models. We focus on calculating scattering rates for the case with two spin-polarised edge channels. We find how these scattering rates depend on the bias (electrochemical potential difference) between the edge channels, the bias direction, and the theoretical model of the edge.

3.1   Non-equilibrium model

In our modelling effort, we are considering the geometry of the Dixon et al. experiment (see Figs. 2.13 and 3.1). We assume the bulk filling factor ν_0 to be 2 throughout the calculation. At $\nu_0 = 2$, there are two edge channels at each edge between the bulk and a fully depleted region (for example, the A gate).

Figure 3.1 shows the current-carrying edge channels in the Dixon et al. geometry. The thickness of the line represents the amount of current carried by the channel. Only spin-up current is let through the AB- and AC-QPCs. Note that not the entire spin-up current that originates from contact 1 flows through the AB-QPC, but that part of it also circulates back to contact 1.

The edge of the scattering region underneath the A gate is the edge we are interested in. This edge is where the scattering takes place in the experiment. In order to calculate the scattering rate between the spin-up and spin-down channel, we should know up until which electrochemical potentials the spin-up and spin-down bands are filled in the scattering region

The naïve option is that the spin-up and spin-down band at the start of the scattering region are filled up until μ_1 and μ_3 since they respectively are connected to contacts 1
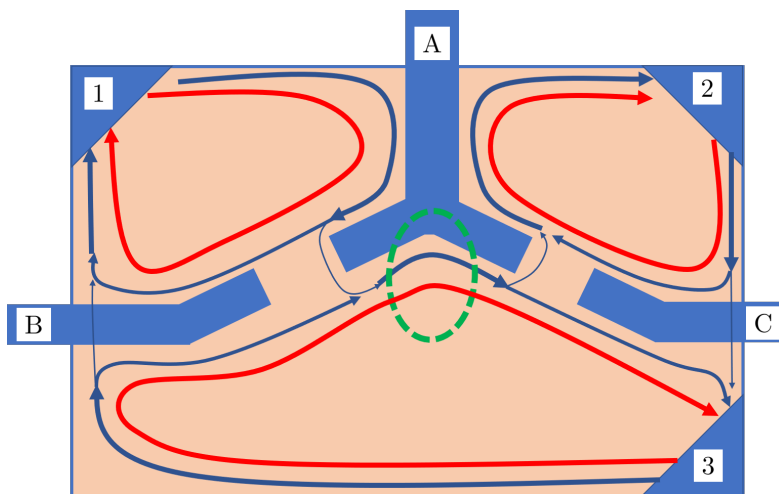
Figure 3.1: Edge channels in the Dixon et al. geometry at zero bias ($\mu_1 = \mu_2 = \mu_3$). The spin-up current is indicated by blue lines and the spin-down current by red lines. The scattering region is encircled by a green dotted line.

and 3 (see Fig. 3.1). This situation is what one would expect in the absence of electron-electron interactions. In appendix A, we use a current conservation argument to show that this is also the case in the presence of interactions. Henceforth, we will sometimes refer to μ_1 as $\mu_\uparrow$, and to μ_3 as $\mu_\downarrow$.

3.1.1 Non-equilibrium pictures in different models

Before calculating the scattering rate, it is necessary to know what the bands and their filling look like at the edge. Only then do we know which transitions from filled to empty states we need to consider and also how these states are separated in both energy and space.

In the following, we present pictures of the edge for the different models discussed in Sec. 2.2. We apply the argument from appendix A by filling the spin-up and spin-down band up until μ_1 and μ_3 respectively. In all figures, we depict the case where both spin-bands of the lowest LL are completely filled in the bulk: $\nu_0 = 2$. In Figs. 3.2a and 3.3b, the electrochemical potential of the spin-up electrons is raised above that of the spin-down electrons: $\Delta\mu = \mu_3 - \mu_1 = \mu_\downarrow - \mu_\uparrow < 0$. In Figs. 3.2b, 3.3c and 3.3d, the electrochemical potential is of the spin-up electrons is lower than that of the spin-down electrons: $\Delta\mu > 0$. Following Dixon et al. [9], we will respectively refer to these cases as the reverse (negative) and forward (positive) bias situations.

Justification of the LLL approximation

In Sec. 2.2.1, we gave an inequality that has to be satisfied for the LLL approximation to be justified [see Eq. (2.10)]. We can now check whether this holds for the type
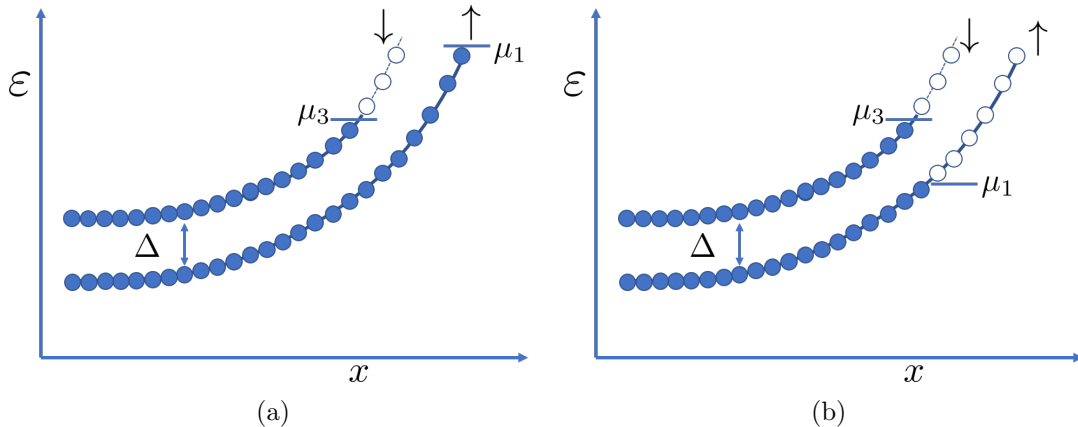
Figure 3.2: The non-equilibrium band filling in the scattering region in the naïve model for reverse bias (a) and forward bias (b).

of experiments we want to model. We check the requirement by calculating a typical electric field strength at the edge for both the naïve and CSG model.

In the naïve model, the electric field is fully determined by the external potential because there is no screening. Kataoka et al. estimated the external potential from the energy dependence of the edge state velocity [38]. During this experiment, they used GaAs/AlGaAs heterostructures at a typical electron density of about 1.8×10^{11} cm^{-2}. By injecting electrons at different energies far above the Fermi level and measuring their velocities, they could deduce the external potential profile. This external potential drops about 60 mV over 150 nm, which corresponds to an average electric field strength of around 4×10^5 V/m.

In the CSG model, the total electric field that an electron experiences is due to both the external potential and the other electronic charges. The electric field is strongest inside the incompressible strip. We estimate the electric field strength in the incompressible strip using parameters from the Dixon et al. experiment (see Sec. 2.3.1) because this is a representative study of the regime we are interested in. Using the parameters from Tab. 2.1, $l = 250$ nm, and $\nu_0 = 2$, the incompressible strip width [see Eq. (2.14)] at zero bias a_0^1 equals 3.1 nm. In equilibrium, the potential drops an amount $\Delta = 0.27$ mV over the incompressible strip. This gives an average electric field strength of 8.7×10^4 V/m inside the incompressible strip. Out of equilibrium, the total potential might become steeper (see Sec. 3.2) but the electric field strength will be of the same order of magnitude for the bias range we are interested in.

In the regime of the Dixon et al. experiment, the scale that controls LL mixing takes the approximate value $\frac{\hbar^2}{me} \frac{1}{l_B^3} = 1.2 \times 10^6$ V/m. Here m is the effective mass in GaAs: $m = 0.067 m_0$. Compared with the estimates above, the inequality in Eq. (2.10) holds, and this justifies the LLL approximation for both the naïve and the CSG models. Thus, we will assume that the occupied and empty states (the blue and white circles in the figures) are LLL states [see Eq. (2.9)].

34

Naïve model

In Fig. 3.2a we see that under reverse bias, extra electrons have been added to the spin-up band compared to the equilibrium ($\mu_1 = \mu_3$) situation. Scattering happens from the spin-up band to the spin-down band. In Fig. 3.2b, we see that the spin-up band is depleted in the scattering region under forward bias. Here scattering happens from down to up.

Note that the spin-splitting Δ is the bare Zeeman-splitting E_z. There is no enhancement of the spin-splitting in the naïve model because the only enhancement that we consider in this thesis comes from the e-e interaction, which the naïve model neglects.

Models including e-e interactions

We have discussed the CSG and exchange models that include e-e interactions in Secs. 2.2.2 and 2.2.3. In this section we discuss the non-equilibrium pictures of the edge in these models.

We start with the simplest, semi-classical CSG model. Figure 3.3 shows the non-equilibrium bands and their respective filling in the scattering region in this model.

In the literature there is consensus on what the band-structure and filling should be in the reverse bias case (see Fig. 3.3b) and in the forward bias case for small ($\Delta\mu < \Delta$) biases (see Fig. 3.3c) [9, 39, 40]. Away from equilibrium, there is a potential drop $\Delta\mu$ additional to the equilibrium drop Δ over the incompressible strip. This additional drop changes the width of the incompressible strip [37]:

$$ a_1 = \left(\frac{\Delta - \Delta\mu}{\Delta} \right)^{1/2} a_1^0, \tag{3.1} $$

where a_1^0 is the incompressible strip width at zero bias. At reverse bias, the width a_1 of the incompressible increases and at forward bias, a_1 becomes smaller. When we reach $\Delta\mu = \Delta$, the incompressible strip between the inner and outer compressible strip disappears completely [37]. There seems to be no consensus on what happens to the bands if the bias is increased even further. For instance, Fig. 2b of Ref. [40] poses that the bands go up as they come from the bulk and then steeply drop again as they reach the edge. This picture appears to contradict the argument constructed in appendix A.

Understanding the band-structure in the 'non-linear' regime $\Delta\mu > \Delta$ is important because some of the experiments are performed in this regime [9, 40].

To shed more light on this regime in the CSG model and exchange models, we have performed a Hartree-Fock (HF) analysis of the edge. The HF analysis is detailed in appendix B, but we will highlight its main aspects and how it justifies the pictures in Fig. 3.3 in the following. Because the CSG model only includes the Hartree interaction, we have made sure to switch off the Fock term to produce the CSG pictures in Fig. 3.3.
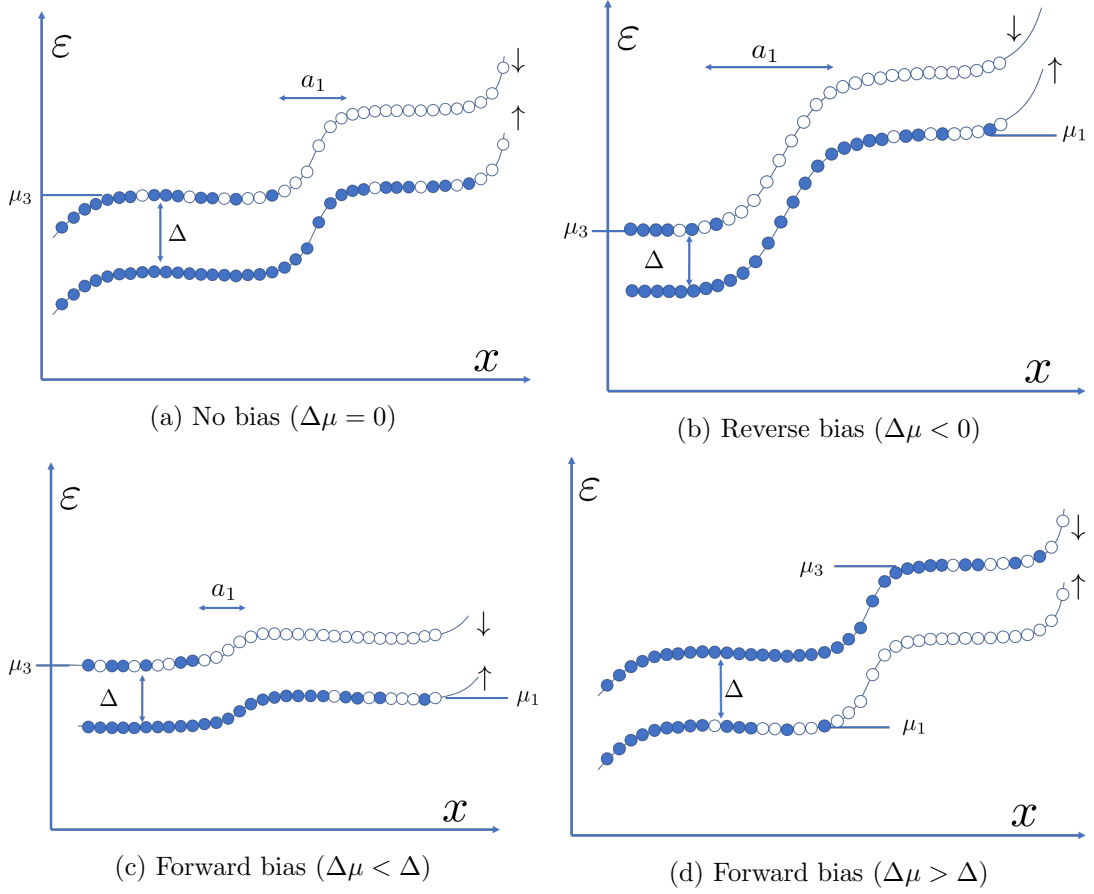
Figure 3.3: The non-equilibrium band filling in the scattering region in the CSG model. Note the decreasing density as we move to the right end of a compressible strip.

Hartree-Fock analysis

In the HF method, we aim to find the best possible (lowest energy) uncorrelated (Slater-determinant) many-body state for a given many-body system. The HF method includes e-e interactions on a mean-field level. Usually, the method boils down to self-consistently finding the optimal single-particle orbitals for a fixed number of particles. This self-consistency means that the single-particle orbitals that determine the mean-field [see Eqs. (B.3) and (B.4)] should be the same single-particle orbitals that diagonalise the mean-field Hamiltonian in Eq. (B.2).

Our approach is a bit different because we fix the single-particle orbitals: we assume that the LLL states [see Eq. (2.3)] form the optimal single-particle basis. However, we do not fix *which* of these LLL states will be filled and which will be empty, and this filling of the orbitals is what we seek to optimise.

The result is the alternating compressible/incompressible strip pattern from the CSG

model (see Fig. 3.3). In our HF simulations, we can see the origin of this pattern: the Hartree interaction ensures that when the external potential is not too steep, it is energetically favourable for an electron to be 'further up the hill' where the external potential is larger, but the electron density is lower. When we zoom out, we see that this is the mechanism that gives rise to the screening of the external potential. The electron density steadily increases over the flat, compressible strip until the density in that sub-LL can increase no further ($n = n_L$). During the simulations, we noted that if the potential is too steep and the external potential difference on neighbouring states is too large compared to the mean-field interaction energy, no screening occurs. In that case, no compressible strip forms and the CSG and naïve picture look much alike.

The next step is to find non-equilibrium distributions where the spin-up and spin-down bands are filled up until different electrochemical potentials $\mu_\uparrow$ and $\mu_\downarrow$. The procedure is similar to that for the equilibrium case.

The Hartree-only simulation gives the expected pictures for no bias, reverse bias and small ($\Delta\mu < \Delta$) forward bias in the CSG model - respectively Figs. 3.3a, 3.3b, and 3.3c. We find that at large ($\Delta\mu > \Delta$) positive bias (see Fig. 3.3d), a new incompressible strip appears.

Another interesting feature that manifests itself in the HF analysis is a strong exchange-enhancement of the spin-splitting due to the Fock term.

To start this discussion, we compare the energy scales of the bare Zeeman spin-splitting E_z and the Coulomb interaction $V_{ee} = \frac{e^2}{4\pi\epsilon_0}\frac{1}{r}$ between two electrons. Using the parameters from the Dixon et al. experiment (Tab. 2.1), we can calculate $E_z = g\mu_B B = 0.18$ meV. As for the Coulomb interaction between two electrons, we have $\frac{e^2}{4\pi\epsilon_0} = 0.12$ eV· nm. Here $\varepsilon = \varepsilon_r \varepsilon_0$ and we took $\varepsilon_r = 12$ for the relative permittivity of GaAs. For a typical length-scale r between two electrons we can look at the 2DEG density n_e, which gives us $r \approx 20$ nm. Hence, the Coulomb energy between two neighbouring electrons is typically around $5 - 10$ meV, which is much larger than the bare Zeeman spin-splitting.

Because of these different energy scales, we expect a large exchange-enhancement of the spin-splitting (see Sec. 2.2.3). In the HF simulations, we observe an exchange-enhancement of the spin-splitting of up to a hundred times the bare spin-splitting E_z in regions where $\nu \approx 1$. This result agrees to some degree with the other theoretical HF studies discussed in Sec. 2.2.3.

The Fock/exchange interactions play a significant role in the HF simulation of the bands using the Dixon et al. parameters. However, no strong exchange-enhancement of the spin-splitting is observed in the experiment (see Sec. 2.3.1). Hence, we cannot exclude that the HF method overestimates the importance of the exchange interaction. On top of this, there seems to be a general disagreement in both experimental and theoretical studies on the effects of exchange (see Sec. 2.2.3). Hence, we choose to perform the scattering calculations only within the naïve and the CSG model, and not pursue the exchange model further.

3.1.2 Treatment of the nuclei as a classical field

Scattering takes place from the spin-up channel to the spin-down channel or vice versa. In order to conserve spin, the scattering mechanism should be able to absorb the difference in the electronic spin. In the experiments [8, 9] discussed in the previous chapter, the hyperfine interaction was found to be the dominant scattering mechanism. Since we try to model the scattering regime of these experiments, we will also assume the hyperfine interaction to be the dominant scattering mechanism.

The conduction band electrons in GaAs are s-like [41]. Therefore, we will consider the hyperfine *contact* interaction, which is the only relevant hyperfine coupling for s-like states that are distributed with spherical symmetry around the nucleus [41]. The hyperfine contact interaction looks as follows in real-space:

$$\hat{V}^{HF}(x,y) = J \sum_j \delta(y-y_j)\delta(x-x_j)\hat{\vec{s}} \cdot \hat{\vec{I}^j},$$

where $\hat{\vec{s}} = \frac{1}{2}\hat{\vec{\sigma}}$ is the dimensionless electronic spin operator, $\hat{\vec{I}}_j$ the dimensionless nuclear spin operator with the j-sum is over all nuclei, and J the hyperfine coupling constant with units of energy. Here (x,y) are the electron coordinates and (x_j, y_j) are the coordinates of the nucleus j. Because of the delta-functions, we consider the electronic wave function at the positions of the nuclei.

We want to first calculate an approximate relaxation rate for the electrons and for that it is not necessary to keep track of the state of the individual nuclei. Instead of considering all nuclei individually, we will describe their effect on the electrons by a classical nuclear field $\vec{B}_N(\vec{r})$. This turns the hyperfine contact interaction into:

$$\hat{V}^{HF}(\vec{r}) = \hat{\vec{s}} \cdot \vec{B}_N(\vec{r}), \tag{3.2}$$

where $\vec{B}_N(\vec{r})$ has units of energy. We can write this interaction in second quantisation [see Eq. (3.3)] using the Landau level eigenstates $\{|nk\rangle\}$ of the system without an external potential from Eq. (2.3) and adding a spin part: $|nk\sigma\rangle = |nk\rangle \otimes |\sigma\rangle$. Because $\{|nk\sigma\rangle\}$ form a complete basis, we have the completeness relation: $\mathbb{1} = \sum_{nk\sigma} |nk\sigma\rangle \langle nk\sigma|$. Inserting this completeness relation twice and plugging in the LL wave functions [see Eq. (2.3)], the second quantised interaction in the LL-basis looks as follows:

$$\hat{V}^{HF} = \frac{1}{2L} \sum_{nk\alpha} \sum_{n'k'\beta} a^\dagger_{nk\alpha} \left[\int d\vec{r}\, e^{i(k'-k)y} f_{nk}(x) f_{n'k'}(x) \hat{\vec{\sigma}}_{\alpha\beta} \cdot \vec{B}_N(\vec{r}) \right] a_{n'k'\beta}, \quad (3.3)$$

where α and β are the spin indices. The operators $a^\dagger_{nk\alpha}$ and $a_{n'k'\beta}$ respectively create and annihilate electrons in the LL-states $|nk\alpha\rangle$ and $|n'k'\beta\rangle$. In the rest of the calculation, we consider Eq. (3.3) with n and n' set to 0 because all scattering processes are confined to the LLL.

In order to perform the calculation of the scattering rate, we should know the properties of this effective nuclear field. In all the experiments we consider, the nuclear Zeeman energy is small ($\sim 0.1 - 1 \; mK$ at $B = 1$ T) and the nuclear dipole-dipole interaction is even smaller ($\sim 0.1 \; \mu K$) compared to the thermal energy. This prevents any nuclear ordering: each nucleus is essentially randomly oriented. Hence, we take the thermal ensemble average - indicated by $\overline{(...)}$ - of each component of the nuclear field $B_N^\alpha(\vec{r})$ to be zero. Moreover, we assume the nuclear field to be completely uncorrelated:

$$\overline{B_N^\alpha(\vec{r})} = 0, \qquad \overline{B_N^\alpha(\vec{r})B_N^\beta(\vec{r'})} = D_0^c\delta_{\alpha\beta}\delta(\vec{r} - \vec{r'}), \tag{3.4}$$

where D_0^c is the squared rms-strength of each component of the effective nuclear field and has units $[energy]^2[length]^2$ (the delta function has units $[length]^{-2}$ because we are considering a two-dimensional system). Using the infinite temperature approximation, which is justified by the extremely low nuclear ordering temperatures, we derive the value of D_0^c to be 1.634×10^{-27} eV^2 m^2 in appendix C.

3.1.3 Calculation of the scattering rate

We now consider two different types of scattering processes: elastic and inelastic. Figure 3.4 illustrates the two processes. Elastic scattering means that a spin-up (spin-down) electron with certain energy scatters into an empty spin-down (spin-up) state with the same energy (arrow 1 in Fig. 3.4). This process conserves the total electronic energy and a scattering rate for this process can be calculated with Fermi's golden rule:

$$\Gamma_{f \leftarrow i} = \frac{2\pi}{\hbar}|\langle f| \hat{V} |i\rangle|^2\delta(\varepsilon_{k_f} - \varepsilon_{k_i}). \tag{3.5}$$
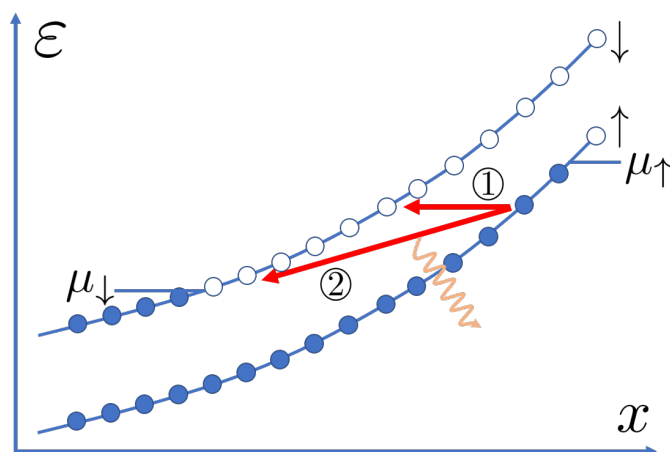

Figure 3.4: Examples of elastic (1) and inelastic (2) relaxation in the case of negative bias ($\mu_\uparrow > \mu_\downarrow$). The wiggly line represents the emission of an acoustic phonon that dissipates the energy difference between the initial and final state.

The $|i\rangle$ state in Eq. (3.5) is the initial non-equilibrium many-body state. We assume a zero-temperature-like distribution for both bands where the spin-up and spin-down states are respectively filled up until $\mu_\uparrow$ and $\mu_\downarrow$. At elevated temperatures, we would have to consider an ensemble of initial states, each with a weight associated with it. Note that electrochemical potentials $\mu_\uparrow$ and $\mu_\downarrow$ respectively correspond to μ_1 and μ_3 in the set-up we discussed above (see Fig. 3.1).

The $|f\rangle$ state is the final many-body state related to $|i\rangle$ through one spin-flip event. The energies ε_{k_i} and ε_{k_f} are respectively the single-particle energies (see Sec. 2.2.4) of the two states involved in the flip event. We neglect the nuclear Zeeman energy and any changes to the Overhauser and Knight fields.

The operator $\hat{V}$ in Eq. (3.5) that connects the initial and final states should be the hyperfine contact interaction [see Eq. (3.3)]. This interaction is a 2×2 matrix and in the reverse bias case (scattering from spin-up to spin-down) we need the $\alpha = \downarrow, \beta = \uparrow$ component:

$$\hat{V}_{\downarrow \leftarrow \uparrow}^{HF} = \frac{1}{2L} \sum_{kk'} a_{k\downarrow}^\dagger \left[\int d\vec{r} \, e^{i(k'-k)y} f_k(x) f_{k'}(x) (B_N^x(\vec{r}) + i B_N^y(\vec{r})) \right] a_{k'\uparrow}. \qquad (3.6)$$

Likewise, for forward bias the relevant part of the interaction is:

$$\hat{V}_{\uparrow \leftarrow \downarrow}^{HF} = \frac{1}{2L} \sum_{kk'} a_{k\uparrow}^\dagger \left[\int d\vec{r} \, e^{i(k'-k)y} f_k(x) f_{k'}(x) (B_N^x(\vec{r}) - i B_N^y(\vec{r})) \right] a_{k'\downarrow}. \qquad (3.7)$$

Inelastic scattering, on the other hand, means that a spin-up (spin-down) electron with a certain energy scatters into an empty spin-down (spin-up) state with a *different* energy (arrow 2 in Fig. 3.4). This process alone does not conserve the total electronic energy and therefore needs an additional process that dissipates/supplies the difference in energy. This scattering rate for the inelastic processes can be calculated with the second-order Fermi's golden rule [42]:

$$\Gamma_{f \leftarrow i} = \frac{2\pi}{\hbar} \left| \sum_\nu \frac{\langle f| \hat{V} |\nu\rangle \langle \nu| \hat{V} |i\rangle}{E_i - E_\nu} \right|^2 \delta(E_f - E_i), \qquad (3.8)$$

where $|\nu\rangle$ is an intermediate many-body state with energy E_ν. We sum over all the intermediate states that can get us from the initial to the final state. We immediately note that we can only use the second-order FGR formalism when no elastic processes are allowed. Otherwise, the denominator in Eq. (3.8) can become zero due to the presence of degenerate states. For example, the inelastic scattering rate for the situation in Fig. 3.4 cannot straightforwardly be calculated using Eq. (3.8) because there are spin-up and spin-down states at the same energy. For the calculation of the inelastic scattering rate in the presence of degenerate states, the calculation becomes more involved (see discussion in chapter 5).

There are multiple conceivable dissipation mechanisms, for instance e-e interactions [43] or acoustical phonons [42]. In this thesis, we take the latter to be the sole dissipation

mechanism at play. Hence, the interaction $\hat{V}$ should contain both a hyperfine part for the spin-flip and an electron-phonon coupling [44] for the dissipation:

$$\hat{V} = \hat{V}^{HF} + \hat{V}^{e-ph}, \qquad \hat{V}^{e-ph} = \sum_{\vec{q},p} \lambda_{\vec{q},p} \rho_{\vec{q}} [b_{\vec{q},p} + b^{\dagger}_{-\vec{q},p}], \tag{3.9}$$

where b and $b^{\dagger}$ are the phonon annihilation and creation operators respectively. In the Fourier-transformed electronic density operator $\rho_{\vec{q}} = \sum_{\vec{k}\sigma'} c^{\dagger}_{\vec{k}\sigma'} c_{\vec{k}+\vec{q}\sigma'}$, the $c^{\dagger}$ and c operators respectively create and annihilate electrons in the plane-wave basis. The $\vec{q}$ and p sums are respectively over the phonon wavevector and the phonon polarisation. The electron-phonon coupling constant $\lambda_{\vec{q},p}$ that appears in Eq. (3.9) is given by:

$$\lambda_{\vec{q},p} = M_{\vec{q},p} \sqrt{\frac{\hbar}{2\rho \mathcal{V} \omega_{\vec{q},p}}}, \qquad M_{\vec{q},p} = M^{pe}_{\vec{q},p} + M^{def}_{q,p}. \tag{3.10}$$

Here ρ is the mass density, $\omega_{\vec{q},p}$ the phonon frequency, and $\mathcal{V}$ the phonon normalisation volume. The constant $M_{\vec{q},p}$ consists of two terms: one for the piezoelectric (pe) and one for the deformation potential (def) mechanism. The piezoelectric coupling mechanism is based on the presence of dipole moments within the unit cell. A phonon that moves through makes these dipoles oscillate and thus couple to the electrons. The deformation coupling mechanism is based on the fact that when a longitudinal phonon travels through a crystal, it changes the distance between the atoms. This changing distance affects the electronic band structure. For the piezoelectric contribution we have:

$$M^{pe}_{\vec{q},p} = ieh_{14} A_{\vec{q},p}. \tag{3.11}$$

Here h_{14} is the piezoelectric constant which is 1.38×10^9 V/m in GaAs, and $A_{\vec{q},p}$ is an anisotropy factor which depends on both the phonon polarisation and direction [42]. In the following, we assume $A_{\vec{q},p} = 1$ and thus neglect all direction-dependence. For the deformation potential contribution we have:

$$M^{def}_{q,p} = \Xi q \delta_{p,l}. \tag{3.12}$$

This mechanism only plays a role for longitudinally polarised phonons and depends only on the magnitude of the phonon wavevector. The value of the deformation potential Ξ is 13.7 eV in GaAs [42]. The deformation potential mechanism becomes increasingly important at larger q i.e., at larger phonon energies. When q is around 10^8 m^{-1}, the deformation potential contribution is comparable to the piezoelectric contribution for longitudinal phonons. If we assume a linear phonon dispersion: $\omega_{\vec{q},p} = v_p q$ with a longitudinal phonon velocity of around 5×10^3 m/s [42], $q = 10^8$ m^{-1} corresponds to a phonon energy of about 0.3 meV. Given a g-factor 0.44, this corresponds to a Zeeman splitting of around 12 T.

We present the general calculation for respectively elastic and inelastic scattering in the following two sections. In Secs. 4.1 and 4.2, we calculate actual scattering rates in the different models for respectively the reverse and forward bias case.

3.2 Elastic scattering rate

In Sec. 3.1.1, we justified the LLL approximation for the regime of the Dixon et al. experiment. In this section, we first calculate the single-electron rate at which an electron in the LLL state $|k_i\sigma\rangle$ elastically relaxes to another, empty LLL state in the opposite spin-band (see Fig. 3.5). After this, we discuss the calculation of the total elastic scattering rate Γ^e between the spin-bands.

As we discussed in the previous section, we use Fermi's golden rule [see Eq. (3.5)] to calculate the scattering rate. We consider spin-up to spin-down scattering, so the occupied state is $|k_i\uparrow\rangle$ and the empty states are $|k_f\downarrow\rangle$, where we sum over k_f. Note that the scattering rate for the opposite direction (spin-down to spin-up) would be exactly the same if the filled and empty states were reversed. In the case of scattering from spin-up to spin-down, the initial and final many-body states are related as follows: $|f\rangle = a^\dagger_{k_f\downarrow}a_{k_i\uparrow}|i\rangle$. Both operators act in the LLL ($n = 0$) but the index n is left out to simplify the notation. We assume a single initial state wherein the spin-up and spin-down bands are respectively filled up until $\mu_\uparrow$ and $\mu_\downarrow$. The scattering rate that we calculate in this way corresponds to the rate at the start of the scattering region, when no equilibration has taken place yet.

The relevant part of the hyperfine contact interaction is given by Eq. (3.6). Plugging this into Eq. (3.5) and summing over the final states gives:

$$\Gamma^e_{\downarrow\leftarrow k_i\uparrow} = \frac{2\pi}{\hbar}\sum_{k_f}|\langle i| a^\dagger_{k_i\uparrow}a_{k_f\downarrow}\hat{V}^{HF}_{\downarrow\leftarrow\uparrow}|i\rangle|^2\delta(\varepsilon_{k_f\downarrow} - \varepsilon_{k_i\uparrow}). \tag{3.13}$$

The energies $\varepsilon_{k_f\downarrow}$ and $\varepsilon_{k_i\uparrow}$ in the delta function are the single-particle energies of the states $|k_f\downarrow\rangle$ and $|k_i\uparrow\rangle$ respectively (see Sec. 2.2.4). We now first evaluate the matrix element $\langle i| a^\dagger_{k_i\uparrow}a_{k_f\downarrow}\hat{V}^{HF}_{\downarrow\leftarrow\uparrow}|i\rangle$ by inserting Eq. (3.6) and performing the k and k' sums:

$$\langle i| a^\dagger_{k_i\uparrow}a_{k_f\downarrow}\hat{V}^{HF}_{\downarrow\leftarrow\uparrow}|i\rangle = \frac{1}{2L}\int d\vec{r}e^{i(k_i-k_f)y}f_{k_f}(x)f_{k_i}(x)\left[B^x_N(\vec{r}) + iB^y_N(\vec{r})\right]\langle i| n_{k_i\uparrow}(1-n_{k_f\downarrow})|i\rangle .\tag{3.14}$$

Here the expectation value of the number operators with respect to the initial many-body state $|i\rangle$ means that the the LLL single-particle states $|k_i\uparrow\rangle$ and $|k_f\downarrow\rangle$ should respectively be occupied and empty for the matrix element to be non-zero. In the following, we assume that $|k_i\uparrow\rangle$ and $|k_f\downarrow\rangle$ are such that the expectation value gives one. We can plug the matrix element back into Eq. (3.13) and then perform the absolute squaring:

$$\Gamma^e_{\downarrow\leftarrow k_i\uparrow} = \frac{2\pi}{\hbar}\frac{1}{4L^2}\sum_{k_f}\int d\vec{r}\int d\vec{r'}e^{i(k_i-k_f)(y-y')}f_{k_f}(x)f_{k_i}(x)f_{k_f}(x')f_{k_i}(x')\times$$
$$[B^x_N(\vec{r}) + iB^y_N(\vec{r})][B^x_N(\vec{r'}) - iB^y_N(\vec{r'})]\delta(\varepsilon_{k_f\downarrow} - \varepsilon_{k_i\uparrow}). \tag{3.15}$$

Next, we average over the different possible realisations of the nuclear field $\vec{B}_N(\vec{r})$ using Eq. (3.4):

$$\overline{[B_N^x(\vec{r}) + iB_N^y(\vec{r})][B_N^x(\vec{r'}) - iB_N^y(\vec{r'})]} = 2D_0^c\delta(\vec{r} - \vec{r'}).$$

We then integrate over the delta-function in $\vec{r'}$ and plug in the explicit form of the transverse wave functions $f_k(x)$ [see Eq. (2.9)] to get:

$$\overline{\Gamma_{\downarrow \leftarrow k_i \uparrow}^e} = \frac{\sqrt{2\pi}}{\hbar} \frac{D_0^c}{2Ll_B} \sum_{k_f} e^{-\frac{d^2}{2l_B^2}} \delta(\varepsilon_{k_f\downarrow} - \varepsilon_{k_i\uparrow}), \tag{3.16}$$

where the overlap between wave functions of the occupied and empty states is determined by the width of the Gaussian wave functions ($\propto l_B$) and the separation $d = X_{k_f} - X_{k_i} = (k_f - k_i)l_B^2$ between their centres. Next we perform the sum over the final states $|k_f\rangle$. Assuming the k-spacing [see Eq. (2.2)] is sufficiently small compared to $1/l_B$, we can convert the k_f-sum to an integral. We then change the integration variable from k_f to ε_{k_f} by introducing the density of states per unit length:

$$\left(\frac{d\varepsilon_k}{dk}\right)^{-1} = \frac{1}{\hbar v_g},$$

to obtain:

$$\overline{\Gamma_{\downarrow \leftarrow k_i \uparrow}^e} = \frac{D_0^c}{2\sqrt{2\pi}\hbar^2 v_{g\downarrow} l_B} e^{-\frac{d^2}{2l_B^2}}, \tag{3.17}$$

where $v_{g\downarrow}$ is the group-velocity [see Eq. (2.8)] of electrons in the spin-down band *at* energy $\varepsilon_{k_i\uparrow}$ [45, 38].

3.2.1 Total elastic scattering rate

Above, we have found an expression for the scattering rate of an electron in the state $|k_i \uparrow\rangle$ into an empty spin-down state at the same energy. We stress that the scattering rate of the opposite process $\overline{\Gamma_{\uparrow \leftarrow k_i \downarrow}^e}$, which takes place under forward bias, is exactly the same when $|k_i \downarrow\rangle$ is occupied and the spin-up band empty at this same energy.

As the bias is increased, there are more electrons in the energy window $\Delta\mu$ between $\mu_\uparrow$ and $\mu_\downarrow$ where $\langle i | n_{k_i\sigma}(1 - n_{k_f\sigma'}) | i \rangle = 1$ (see Fig. 3.4). These electrons can scatter elastically to the other spin-band and thus contribute to the *total* scattering rate. To calculate this total scattering rate, we should sum over all possible initial wavenumbers k_i:

$$\overline{\Gamma_{\sigma' \leftarrow \sigma}^e} = \sum_{k_i} \frac{D_0^c}{2\sqrt{2\pi}\hbar^2 v_{g\sigma'} l_B} e^{-\frac{d^2}{2l_B^2}} = \int_{\mu_{\sigma'}}^{\mu_\sigma} d\varepsilon \frac{L}{2\pi\hbar v_{g\sigma}} \frac{D_0^c}{2\sqrt{2\pi}\hbar^2 v_{g\sigma'} l_B} e^{-\frac{d^2}{2l_B^2}}. \tag{3.18}$$

Note that the total rate is proportional to L because the y-length determines how closely spaced the wave functions are in the x-direction: $\Delta x = \Delta k l_B^2 = \frac{2\pi}{L} l_B^2$. When converting from a k-integral to a ε-integral, we again get a density of states per unit length factor $\frac{1}{\hbar v_{g\sigma}}$, where $v_{g\sigma}$ is the group velocity in the band of departure at energy ε. The difficulty is now that the distance d between the centres of the wavefuctions of the LLL states $|k_i\sigma\rangle$ and $|k_f\sigma'\rangle$ may also depend on the energy ε of these states. Moreover, the group velocities $v_{g\sigma}$ and $v_{g\sigma'}$ may also depend on ε.

For the reverse bias case in the CSG model, for example, *same-energy* states are generally closer together if both are in the sloped (incompressible) region, and further apart when either the occupied or empty state is in a flat (compressible) region (see Fig. 3.3b). In the naïve model, we see that when the external potential is not linear, the spatial separation d between same-energy states also changes. In Fig. 3.2 for example, we see that same-energy states are closer together at higher energies.

Linearisation

Usually we do not have sufficient knowledge about the actual shape of the external potential. A sensible first attempt is to assume that the dispersion is linear near the Fermi level:

$$\varepsilon_{k\uparrow} = \hbar v_{g\uparrow}|k| - \frac{1}{2}\Delta, \qquad \varepsilon_{k\downarrow} = \hbar v_{g\downarrow}|k| + \frac{1}{2}\Delta. \qquad (3.19)$$

This approximation is well-justified for small biases ($|\Delta\mu| < \Delta$). In the simplest case, we have two parallel lines: $v_{g\uparrow} = v_{g\downarrow}$. This is illustrated in Fig. 3.5.

In this case, there is the following relation between the separation d, the spin-splitting Δ and the velocity v_g appearing in Eq. (3.19):
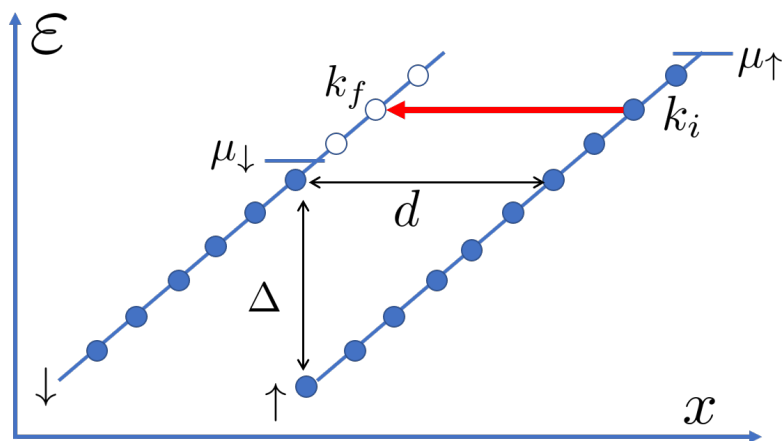

Figure 3.5: Elastic relaxation in the reverse bias case ($\mu_\uparrow > \mu_\downarrow$) at linear dispersion.

$$d = \left(\frac{d\varepsilon}{dx}\right)^{-1}\Delta = \left(\frac{1}{l_B^2}\frac{d\varepsilon}{dk}\right)^{-1}\Delta = \frac{l_B^2}{\hbar v_g}\Delta. \tag{3.20}$$

Because the bands run perfectly parallel the separation does not depend on energy. We apply this simplest case to the naïve model. In this case, the equation for the total rate in Eq. (3.18) turns into:

$$\overline{\Gamma^e_{\sigma'\leftarrow\sigma}} = \frac{LD_0^c(\mu_\sigma - \mu_{\sigma'})}{4\pi\sqrt{2\pi}\hbar^3 v_g^2 l_B}e^{-\frac{l_B^2\Delta^2}{2\hbar^2 v_g^2}}. \tag{3.21}$$

We now estimate the group velocity at the edges so that we can get a number out of the formula in Eq. (3.21). Time-of flight measurements provide a way to measure the group velocity at the edges. Kamata et al. [45] showed that the group velocity along an edge defined by a metallic gate electrode is $2.8\times10^5 - 4.3\times10^5$ m/s in a AlGaAs/ GaAs sample at 6.5 T ($\nu_0 = 2$). In a similar experiment, Kataoka et al. [38] found a group velocity of $0.5\times10^5 - 1\times10^5$ m/s. They made sure to deplete the edge and inject an electron well above the Fermi energy to avoid the influence of interactions with the other electrons in the system. Although there seems to be a dependence on the details of the edge, 10^5 m/s seems to be the right order of magnitude estimate for the group velocity of electrons at the edge.

Using this estimate for the group velocity and a spin-splitting energy of 0.27 meV as reported by Dixon et al. [9], we find a separation d [see Eq. (3.20)] of about 0.4 nm at $B = 7$ T. This separation is very small compared to the magnetic length l_B. This implies that the exponential in Eq. (3.17) does not significantly suppress the scattering rate.

In the biased CSG model, we can also assume linear dispersion within the incompressible strip (see Fig. 4.2). We now give an estimate for the velocities [see Eq. (3.19)] in the incompressible strips. At zero bias, the separation d [see Eq. (3.20)] between the spin-up and spin-down electrons closest to the incompressible strip is equal to the incompressible strip width a_1^0 [see Eq. (2.14)]. Using the parameters from Tab. 2.1, $l = 250$ nm, and ν_0 equal to 2, we get $a_1^0 = 3.1$ nm. Using Eq. (3.20) we can calculate that this corresponds to a velocity v_g of around 1.3×10^4 m/s.

At non-zero bias, the incompressible strip width changes with the square-root of the bias [see Eq. (3.1)]. Hence, the slope of the bands in the incompressible strip changes. Assuming a constant spin-splitting Δ, the separation d between the bands varies as:

$$d = a_1^0\left(\frac{\Delta}{\Delta - \Delta\mu}\right)^{\frac{1}{2}}. \tag{3.22}$$

Via the relation in Eq. (3.20), this also changes the velocity v_g in the linearised picture.

In Secs. 4.1 and 4.2 we use the theory from this section to calculate some elastic scattering rates. First, however, we will discuss the inelastic relaxation mechanism.

3.3 Inelastic relaxation rate

During the inelastic scattering process in the single-particle picture, an electron relaxes to the opposite spin-band and lowers its energy while doing so. As mentioned in Sec. 3.1.3, we assume the emission of acoustical phonons to be the primary mechanism that dissipates the energy difference between the initial and final electronic state. We do not consider processes where the electrons *absorb* energy from acoustical phonons and scatter to a higher energy state because the experiments we are modelling were performed at very low temperatures (see Sec. 2.3).

Given that we are in a situation without degenerate states (see Fig. 3.6), we are allowed to use the second-order FGR [see Eq. (3.8)] to calculate the inelastic scattering rate. We first focus on the internal sum:

$$\sum_\nu \frac{\langle f| \hat{V} |\nu\rangle \langle \nu| \hat{V} |i\rangle}{E_i - E_\nu}, \tag{3.23}$$

where we sum over all processes that can take us from the initial many-body state $|i\rangle$ via an intermediate state $|\nu\rangle$ to *the same* final many-body state $|f\rangle$. Later, we take the absolute square of this result and then sum over all the possible final states $|f\rangle$ where one spin is flipped compared to the initial state $|i\rangle$. In this calculation we assume $T = 0$, just as we did for the elastic calculation in Sec. 3.2. Hence, we only consider *one* initial state $|i\rangle$. The initial, intermediate and final states all consist of an electronic part and a phonon part: $|i\rangle = |i_e\rangle \otimes |vac\rangle$ and $|f\rangle = |f_e\rangle \otimes |1_{\vec{q},p}\rangle$. Here $|vac\rangle$ is the phonon vacuum and $|1_{\vec{q},p}\rangle = b_{\vec{q},p}^\dagger |vac\rangle$ is one phonon with wavevector $\vec{q}$ and polarisation p added to the phonon vacuum. The energy of this phonon is $\omega_q^{(p)}$.

By writing the electron-phonon coupling [see Eq. (3.9)] in the LL basis $\{|kn\rangle\}$ [see Eq. (2.3)], we see that the phonon emission process can also cause an electron to transition to another state, without changing its spin this time:

$$\hat{V}^{e-ph} = \sum_{\vec{q}',p'} \lambda_{\vec{q}',p'} \sum_{k_y \sigma'} \sum_{nn'} \int dx\, f_{k_y n'}(x) f_{k_y + q_y' n}(x) e^{-iq_x' x} a_{k_y n' \sigma'}^\dagger a_{k_y + q_y' n \sigma'} [b_{\vec{q}',p'} + b_{-\vec{q}',p'}^\dagger]. \tag{3.24}$$

Anticipating that we will only use the inelastic calculation in the forward bias case, we consider an initial state where the spin-down band is filled up until a higher electro-chemical potential than the spin-up band. Figure 3.6 shows a picture of the bands that shows both steps of the inelastic scattering process: the spin-flip from $|k_i \downarrow\rangle$ to $|k_f \uparrow\rangle$, and the emission of a phonon with wavevector $\vec{q}$ and polarisation p. During the phonon emission, an electron also transitions from $|k_i' \sigma\rangle$ to $|k_f' \sigma\rangle$. Note that in order to elucidate the process in the simplest way, the bands in Fig. 3.6 are linearised. We again employ the LLL approximation. Hence, we only consider $n = n' = 0$ in Eq. (3.24). Generally, the final electronic state $|f_e\rangle$ then differs from the initial one $|i_e\rangle$ at four points: $|k_i \downarrow\rangle, |k_f \uparrow\rangle, |k_i' \sigma\rangle$, and $|k_f' \sigma\rangle$.
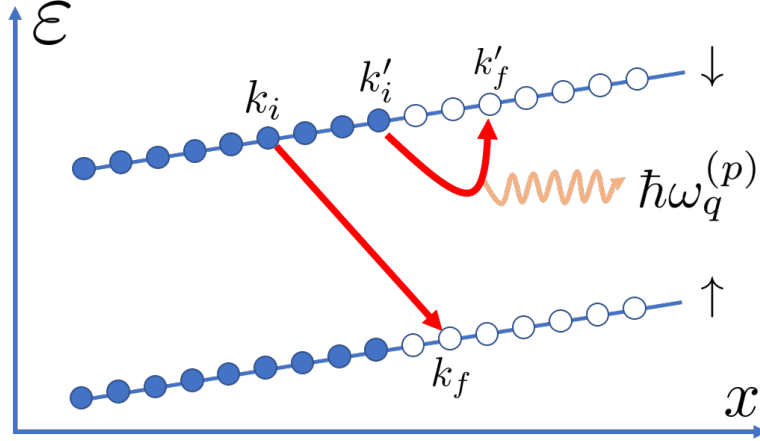
Figure 3.6: Inelastic relaxation in the forward bias case ($\mu_\uparrow < \mu_\downarrow$) at linear dispersion.

There are two types of processes that connect $|i\rangle$ and $|f\rangle$. In the first type of process, the spin-flip 'happens first' and $\hat{V}^{HF}$ takes the initial state $|i\rangle$ to the intermediate state $|\nu\rangle = a^\dagger_{k_f\uparrow}a_{k_i\downarrow}|i_e\rangle \otimes |vac\rangle$. Subsequently, the phonon emission happens and takes the intermediate state to the final state $|f\rangle = a^\dagger_{k'_f\sigma}a_{k'_i\sigma}|\nu_e\rangle \otimes |1_{\vec{q},p}\rangle$. Here σ could be both $\uparrow$ and $\downarrow$ because the transition could happen on either branch.

In the second type of process, the phonon emission happens first and $\hat{V}^{e-ph}$ takes $|i\rangle$ to $|\nu\rangle = a^\dagger_{k'_f\sigma}a_{k'_i\sigma}|i_e\rangle \otimes |1_{\vec{q},p}\rangle$. Secondly, the spin-flip takes the intermediate state to the final state $|f_e\rangle = a^\dagger_{k_f\uparrow}a_{k_i\downarrow}|\nu_e\rangle \otimes |1_{\vec{q},p}\rangle$.

The way to proceed is to calculate the matrix elements $\langle f|\hat{V}|\nu\rangle$ and $\langle \nu|\hat{V}|i\rangle$ for both types of processes and then perform the ν-sum [see Eq. (3.23)]. It turns out that for a process as the one that is shown in Fig. 3.6, the terms in the sum cancel each other. This cancelling is because the spin-flip and the phonon emission are independent because they can happen in either order. The denominator $E_i - E_\nu$ has the same magnitude for both terms because the delta-function in Eq. (3.8) demands that the energy dissipated by the phonon emission (energy of phonon plus the electronic transition) is equal to the energy difference between the states involved in the spin-flip. However, the denominators have a different sign. Hence the term corresponding to the first process (spin-flip followed by phonon emission) is cancelled by the term corresponding to the second process (phonon emission followed by spin-flip).

There is no such cancellation when the second step of the process uses an electron state involved in the first step. An example of this is shown in Fig. 3.7. For these non-cancelling processes, the final electronic state differs from the initial electronic state on only two points: $|k_i \downarrow\rangle$ and $\left|k'_f \uparrow\right\rangle$ in the case of Fig. 3.7. In this case, there is no cancellation between the matrix elements of the first and second type processes because the matrix elements are different.

We have seen that only when the final electronic state differs at two points from the
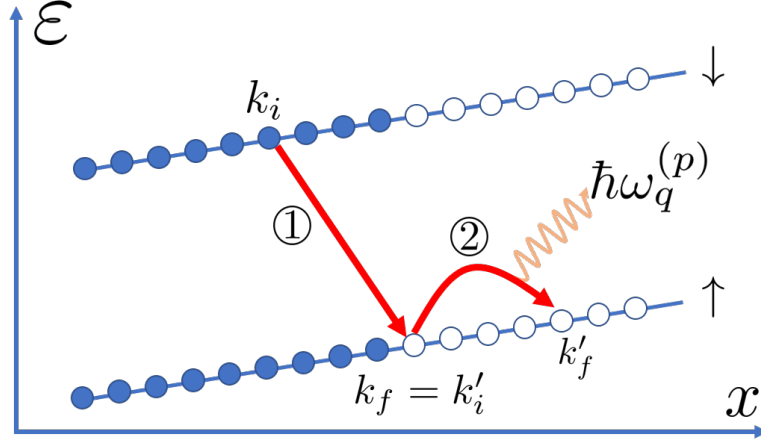
Figure 3.7: Inelastic scattering process where the electron involved in the first process is 'recycled' in the second process. In this example, the spin-flip (1) has to happen before the phonon emission (2).

initial electronic state, Eq. (3.23) is non-zero. We now write the final electronic state as: $|f_e\rangle = a^\dagger_{k_e\uparrow} a_{k_h\downarrow} |i_e\rangle$. In the case when $q_y \neq 0$, so when the phonon is not perpendicular to the edge, and using the new labels k_e and k_f, the ν-sum from Eq. (3.23) can be calculated to be:

$$\frac{\lambda_{\vec{q},p}}{2(\varepsilon_{k_h+q_y\downarrow} - \varepsilon_{k_e\uparrow})L} \int d\vec{r} \, e^{i(k_h-k_e+q_y)y} f_{k_e}(x) f_{k_h+q_y}(x)[B^x_N(\vec{r}) + iB^y_N(\vec{r})] \times$$

$$\int dx' f_{k_h+q_y}(x') f_{k_h}(x') e^{iq_x x'} n_{k_h\downarrow}(1 - n_{k_e\uparrow})(2n_{k_h+q_y\downarrow} - 1)$$

$$+ \frac{\lambda_{\vec{q},p}}{2(\varepsilon_{k_h\downarrow} - \varepsilon_{k_e-q_y\uparrow})L} \int d\vec{r} \, e^{i(k_h-k_e+q_y)y} f_{k_e-q_y}(x) f_{k_h}(x)[B^x_N(\vec{r}) + iB^y_N(\vec{r})] \times$$

$$\int dx' f_{k_e}(x') f_{k_e-q_y}(x') e^{iq_x x'} n_{k_h\downarrow}(1 - n_{k_e\uparrow})(1 - 2n_{k_e-q_y\uparrow}). \quad (3.25)$$

For the special case $q_y = 0$, the result will be slightly different. However, as we will show later on, we can neglect this case because it forms a negligible contribution. The occupation factors $n_{k\sigma}$ can be either 0 or 1. We used the delta-function in Eq. (3.8) to write the energy denominators $E_i - E_\nu$ in terms of the single-particle energies. The first and second terms in Eq. (3.25) respectively refer to processes where the electronic transition that goes with the phonon emission happens on the spin-down/spin-up branch. In Fig. 3.8 panels (a) and (b) correspond to cases described by the first term in Eq. (3.25) is non-zero. Panels (c) and (d) correspond to the second term in Eq. (3.25).

In the first term in Eq. (3.25) the factor $(2n_{k_h+q_y\downarrow} - 1)$ determines the overall sign of the term. When the intermediate state $|k_h + q_y \downarrow\rangle$ is initially occupied, the sign is positive and the spin-flip has to happen before the phonon emission (panel (a) in
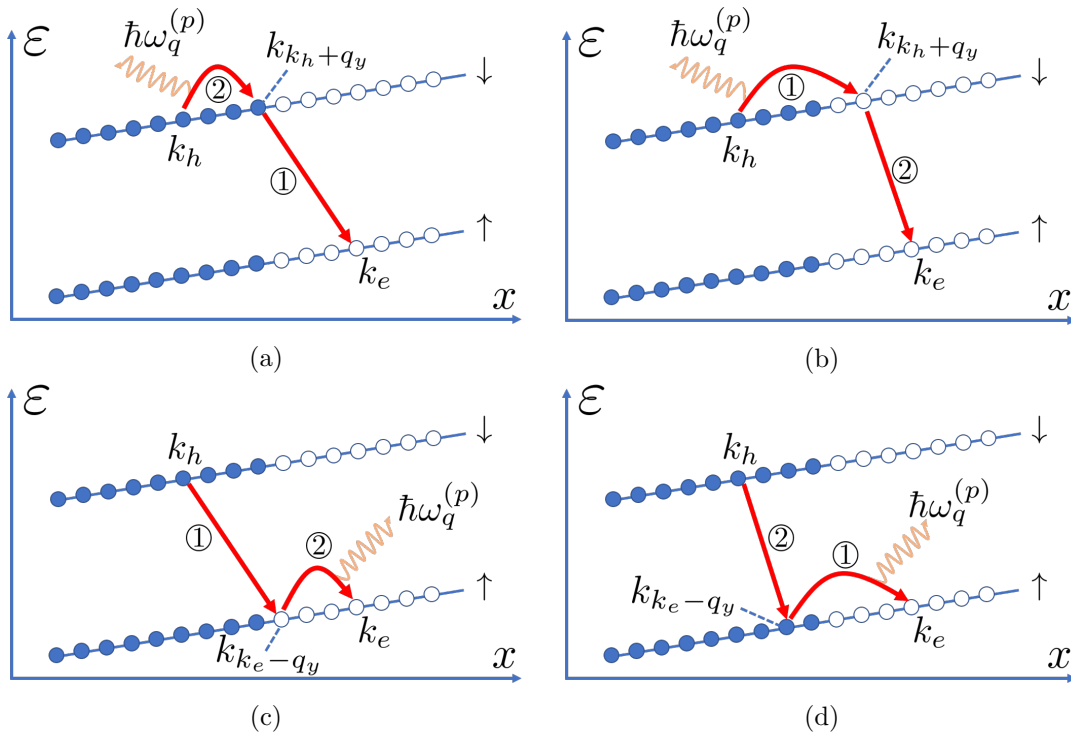
Figure 3.8: Examples of scattering processes where the spin-flip and phonon emission steps are coupled. These processes contribute to the total scattering rate [see Eq. (3.27)]. Panels (a) and (b) correspond to the first term in Eq. (3.25). Panels (c) and (d) correspond to the second term in Eq. (3.25). The numbers ① and ② indicate which step happens first.

Fig. 3.8). When the intermediate state $|k_h + q_y \downarrow\rangle$ is initially empty, we get a negative sign (panel (b) in Fig. 3.8). Likewise, for the second term in Eq. (3.25), the factor $(1 - 2n_{k_e-q_y\uparrow})$ determines the overall sign. Again, when the spin-flip happens before the phonon emission, the overall sign is positive. When it is the other way around, the overall sign is negative.

We note that the final states $|f\rangle$ for panels (a) and (c) are equal to each other because k_h, k_e, and q_y are the same in both processes (and we take q_x, q_z, and p to be the same for both processes as well). Hence, these two processes interfere. They do not cancel because their matrix elements [see Eq. (3.25)] are different. The same holds for panels (b) and (d).

The next step is to perform the absolute square of the expression in Eq. (3.25) to account for the interference between the different paths leading to the same final state $|f\rangle$. At the same time, we average over the different realisations of the nuclear field to insert the assumed characteristics of the nuclear field [see Eq. (3.4)]:

$$\overline{\left|\sum_\nu \frac{\langle f|\,\hat{V}\,|\nu\rangle\,\langle\nu|\,\hat{V}\,|i\rangle}{E_i - E_\nu}\right|^2} = \frac{|\lambda_{\vec{q},p}|^2 D_0^c}{2\sqrt{2\pi}l_B L}e^{-\frac{1}{2}l_B^2(k_e - k_h - q_y)^2}e^{-\frac{1}{2}l_B^2(q_x^2 + q_y^2)}n_{k_h\downarrow}(1 - n_{k_e\uparrow})\times$$

$$\left(\frac{1}{(\varepsilon_{k_h + q_y\downarrow} - \varepsilon_{k_e\uparrow})^2} + \frac{1}{(\varepsilon_{k_h\downarrow} - \varepsilon_{k_e - q_y\uparrow})^2} + \right.$$

$$\left. \frac{2(2n_{k_h + q_y\downarrow} - 1)(1 - 2n_{k_e - q_y\uparrow})}{(\varepsilon_{k_h + q_y\downarrow} - \varepsilon_{k_e\uparrow})(\varepsilon_{k_h\downarrow} - \varepsilon_{k_e - q_y\uparrow})}e^{-\frac{1}{2}l_B^2 q_y^2}\cos[l_B^2 q_x(k_h + q_y - k_e)]\right). \quad (3.26)$$

The transverse wave functions in Eq. (3.25) are simple Gaussians in the LLL [see Eq. (2.9)]: $f_k(x) = \frac{1}{\sqrt{\pi^{1/2}l_B}}e^{\frac{1}{2l_B^2}(x + kl_B^2)^2}$. To get to the expression in Eq. (3.26), we have used the integrals from appendix D.

The final step in calculating the inelastic scattering rate $\overline{\Gamma^i_{\uparrow\leftarrow\downarrow}}$ is summing over the possible final configurations. We assumed there to be only one initial many-body state $|i\rangle$, corresponding to zero-temperature distributions in both bands. The final state differs from the initial state by: the phonon wavevector $\vec{q} = (q_x, q_y, q_z)$, the phonon polarisation p, and the wavenumbers k_h and k_e. These are then also the variables we should sum over to get the total inelastic scattering rate:

$$\overline{\Gamma^i_{\uparrow\leftarrow\downarrow}} = \frac{2\pi}{\hbar}\sum_p \sum_{q_x q_y q_z} \sum_{k_e k_h}\left|\sum_\nu \frac{\langle f|\,\hat{V}\,|\nu\rangle\,\langle\nu|\,\hat{V}\,|i\rangle}{E_i - E_\nu}\right|^2 \delta(\Delta E(k_h, k_e) - \hbar\omega_q^{(p)}). \quad (3.27)$$

The delta-function in Eq. (3.27) contains the energy difference $\Delta E(k_h, k_e)$ between the $|k_h \downarrow\rangle$ and $|k_e \uparrow\rangle$ states, and the phonon energy $\hbar\omega_q^{(p)}$. We assume the latter to have a linear dispersion relation and be independent of the phonon direction [42]:

$$\omega_q^{(p)} = q v_p.$$

The delta-function fixes the magnitude of the phonon wavevector q for a given k_h and k_e to be:

$$q_p = \frac{\Delta E(k_h, k_e)}{\hbar v_p}. \quad (3.28)$$

This eliminates one degree of freedom. In applying the Dirac delta function, we convert the q-sums to integrals. When we have that Δq is much smaller than $1/l_B$, we can convert the q-sums to integrals just like we did for the k-integrals in the inelastic calculation (see Sec. 3.2). Additionally, this allows us to neglect the special case $q_y = 0$ because it would not contribute significantly. When we assume a system length of about 1 μm and a magnetic field of 7 T as in the Dixon et al. [9] experiment, this condition is satisfied. When we convert the sums to integrals, we do so in spherical coordinates:

$$q_x = q\sin\theta\cos\phi, \qquad q_y = q\sin\theta\sin\phi, \qquad q_z = q\cos\theta, \quad (3.29)$$

so that:

$$\sum_{q_x q_y q_z} \rightarrow \frac{\mathcal{V}}{(2\pi)^3} \int dq \int d\theta \int d\phi \sin\theta q^2, \tag{3.30}$$

where $\mathcal{V}$ is the same normalisation volume as in Eq. (3.10). We then perform the q-integral in Eq. (3.27), insert the definition of the electron-phonon coupling [see Eq. (3.10)], and plug in the absolute square of the ν-sum from Eq. (3.26):

$$\overline{\Gamma^i_{\downarrow \leftarrow \uparrow}} = \frac{D_0^c}{4\rho\hbar(2\pi)^2\sqrt{2\pi}l_B L} \sum_{p,k_e,k_h} \frac{q_p(e^2 h_{14}^2 + \Xi^2 q_p^2 \delta_{p,l})}{v_p^2} \int d\theta \int d\phi \sin\theta e^{-\frac{1}{2}l_B^2(k_e - k_h - q_p \sin\theta \sin\phi)^2} \times$$

$$e^{-\frac{1}{2}l_B^2 q_p^2 \sin^2\theta} n_{k_h\downarrow}(1 - n_{k_e\uparrow}) \left(\frac{1}{(\varepsilon_{k_h+q_y\downarrow} - \varepsilon_{k_e\uparrow})^2} + \frac{1}{(\varepsilon_{k_h\downarrow} - \varepsilon_{k_e-q_y\uparrow})^2} + \right.$$

$$\left. \frac{2\mathfrak{S}(k_h,k_e,\theta,\phi,p)e^{-\frac{1}{2}l_B^2 q_p^2 \sin^2\theta \sin^2\phi}}{(\varepsilon_{k_h+q_y\downarrow} - \varepsilon_{k_e\uparrow})(\varepsilon_{k_h\downarrow} - \varepsilon_{k_e-q_y\uparrow})} \cos[l_B^2 q_p \sin\theta \cos\phi(k_h + q_p \sin\theta \sin\phi - k_e)] \right), \tag{3.31}$$

where q_p is defined in Eq. (3.28) and

$$\mathfrak{S}(k_h,k_e,\theta,\phi,p) = (2n_{k_h+q_p \sin\theta \sin\phi\downarrow} - 1)(1 - 2n_{k_e - q_p \sin\theta \sin\phi\uparrow})$$

determines the sign.

In general, the expression in Eq. (3.31) is calculated numerically. In order to perform the calculation, we need to know how the energies $\varepsilon_{k\sigma}$ depend on k and σ (the dispersion). We also need to know the respective occupations of the spin-up and spin-down bands. This information is contained in the electrochemical potentials $\mu_\uparrow$ and $\mu_\downarrow$.

Chapter 4

Evaluation of scattering rates

In this chapter, we calculate values for the scattering rates in both the reverse and forward bias situations and compare these results to the experimental data that we discussed in Sec. 2.3. We find it important to mention that although the Wald et al. and Dixon et al. experiments have provided the main inspiration for our calculations, we aim to understand spin relaxation in general and not explain these experiments specifically.

4.1 Rates for reverse bias

In this section, we calculate the scattering rates for reverse bias ($\Delta\mu < 0$) in both the naïve and the CSG models. In all calculations, we assume the bulk filling factor ν_0 to be 2, unless explicitly stated otherwise.

4.1.1 Naïve model

Figure 4.1 shows the reverse bias situation in the naïve model. Because of the presence of degenerate states, we cannot use the second-order FGR to calculate the inelastic scattering rate. Hence, we limit ourselves to calculating the elastic scattering rate. The contribution of the inelastic scattering grows relative to that of elastic scattering as the bias strength is increased. This because the number of possible inelastic scattering processes grows faster than the number of possible elastic scattering processes as the bias voltage is made more negative. Therefore, neglecting inelastic scattering at a small bias is not as bad as doing it at a large bias.

As we discussed in Sec. 3.2, at small bias we may linearise the electronic dispersion [see Eq. (3.19)]. We then use Eq. (3.21) to calculate the total elastic scattering rate $\overline{\Gamma^e_{\downarrow\leftarrow\uparrow}}$.

We now estimate the rate by inserting realistic values for the parameters (see tables 2.1 and 4.1). We take 10^5 m/s for both $v_{g\uparrow}$ and $v_{g\downarrow}$ (see the discussion in Sec. 3.2). The value for D_0^c is derived in appendix C. Looking at the size of the sample (see Fig. 1b in Ref. [9]), 1 μm seems to be a realistic estimate for the length L. Because the
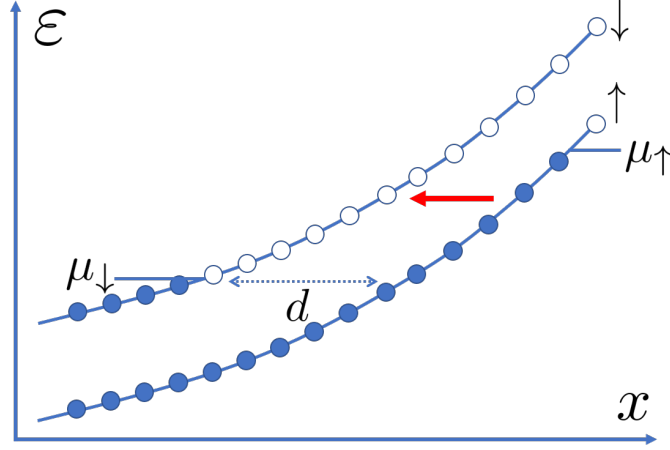
Figure 4.1: Reverse bias situation in the naïve model.

linearisation is justified for small biases ($|\Delta\mu| < \Delta$), we take $\Delta\mu$ to equal $-\frac{1}{2}\Delta = -0.14$ meV. This gives a total elastic scattering rate:

$$\overline{\Gamma^e_{\downarrow\leftarrow\uparrow}} = \frac{LD^c_0|\Delta\mu|}{4\pi\sqrt{2\pi}\hbar^3 v_g^2 l_B} e^{-\frac{l_B^2\Delta^2}{2\hbar^2 v_g^2}} = 2.7 \times 10^5 \text{s}^{-1}.$$

We note that using these parameters, the exponent $-\frac{l_B^2\Delta^2}{2\hbar^2 v_g^2}$ has a value of -7.9×10^{-4}. Hence, the exponential does not provide any suppression.

Parameter	Symbol	Value
Mean-squared-strength of $\vec{B}_N(\vec{r})$	D^c_0	1.634×10^{-27} [eV]^{2}m^2
Group velocities in naïve model	v_g	10^5 m/s
Length	L	1 μm

Table 4.1: Basic parameters that are used to calculate the rates in this chapter.

Taking this relaxation rate and the velocity v_g, we calculate a relaxation *length*: $l_x = \frac{v}{\Gamma} = 5$ cm. The fact that $l_x \gg L$ means that few electrons actually decay as they travel from contact 1 to contact 2 in the Dixon et al. geometry (see Fig. 2.13). In Sec. 4.3, we compare the relaxation rate to the experimentally observed scattering currents.

4.1.2 CSG model

In the CSG model, we cannot use this simple picture of parallel bands over the entire energy window $\Delta\mu$. Instead, we can divide the energy window up into three parts as in Fig. 4.2.
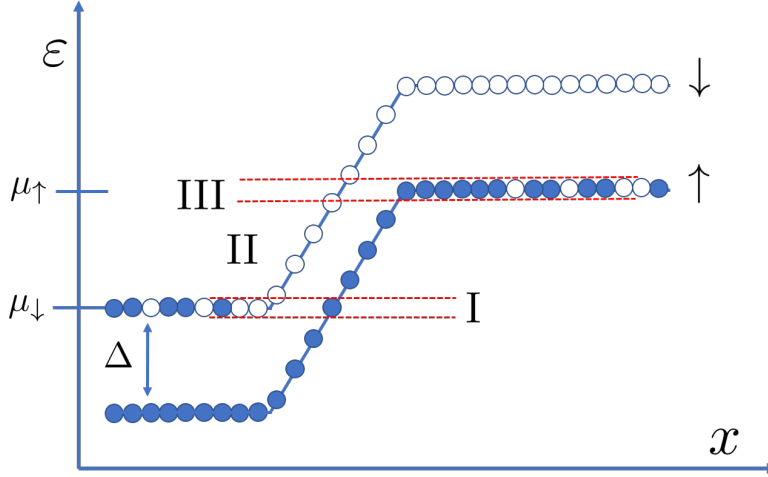
Figure 4.2: Stepwise linearisation in the CSG picture of the non-equilibrium edge at reverse bias.

The calculation for window II is the same as the one for the negative bias case in the naïve model (see Sec. 4.1.1). However, there are there are two main differences that we discussed in Sec. 3.2: the separation between the bands is much larger ($d = a_1^0 = 3.1$ nm at zero bias) and hence the velocity of the linearised bands is much smaller ($v_g = 1.3 \times 10^4$ m/s). Furthermore, the separation d becomes smaller, and the velocity v_g larger as the bias becomes more negative [see Eq. (3.22)]. On the one hand, this means that the overlap between the occupied and empty states increases, but on the other hand, the density of states of both bands decreases. However, under relatively small bias ($|\Delta\mu| \sim \Delta$), we can neglect these effects. Again, assuming a small bias: $\Delta\mu = -\frac{1}{2}\Delta$ and using the same parameters as in the naïve model calculation, this gives a total elastic scattering rate:

$$\overline{\Gamma_{\downarrow\leftarrow\uparrow}^{e,II}} = \frac{L D_0^c |\Delta\mu|}{4\pi\sqrt{2\pi}\hbar^3 v_g^2 l_B} e^{-\frac{d^2}{2l_B^2}} = 1.6 \times 10^7 \text{s}^{-1},$$

for window II. We note that this value is almost a factor hundred larger than in the naïve model. Using these parameters, the exponent $-\frac{d^2}{2l_B^2}$ has a value of -5.1×10^{-2}. The magnitude of the exponent is definitely larger than for the naïve case. However, the exponential still does not provide significant suppression. Because of the presence of degenerate states, we cannot calculate an inelastic scattering rate for window II.

There is elastic scattering from the sloped spin-up band into the almost flat spin-down band with a large final density of states in window I. We estimate this contribution to the total scattering rate by giving the spin-down band a finite slope as in Fig. 4.3. In a real sample, a finite temperature will produce a finite slope [17]. In this simplification, we treat the spin-down band as completely empty. Now that we have two sloped bands
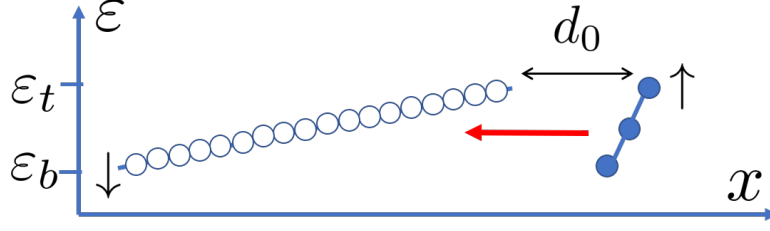
Figure 4.3: Simplification of the region I in 4.2.

with respective velocities $v_{g\uparrow}$ and $v_{g\downarrow}$, we can use the formalism that we introduced in section 3.2.

We take the width of the empty spin-down band b_2, which is the width of the second compressible strip, to be much larger than l_B. The height of the energy window $E_t - E_b$ is related to $v_{g\downarrow}$ and b_2 via:

$$E_t - E_b = \frac{\hbar v_{g\downarrow} b_2}{l_B^2}.$$

The separation between the filled and empty states d is dependent on ε in this case, and can be parametrised using:

$$d = d_0 + \frac{(\varepsilon_t - \varepsilon) l_B^2}{\hbar v_{g\downarrow}},$$

where we have assumed that $v_{g\uparrow} \gg v_{g\downarrow}$. Plugging this into Eq. (3.18) and performing the ε-integral gives:

$$\overline{\Gamma_{\downarrow\leftarrow\uparrow}^{e,I}} = \frac{D_0^c L}{8\pi\hbar^2 v_{g\uparrow} l_B^2} \left[erf\left(\frac{d_0 + b_2}{\sqrt{2} l_B}\right) - erf\left(\frac{a_1^0}{\sqrt{2} l_B}\right) \right], \tag{4.1}$$

where $erf()$ is the error function. When $b_2 \gg l_B$ and $a_1^0 \ll l_B$, the sum of the error function within the square brackets becomes equal to 1. In our calculation we can safely assume the width of the second compressible strip to be larger than the magnetic length. Furthermore, we assume the separation d_0 to be equal to a_1^0, which is larger than l_B using our parameters. Hence, the total elastic scattering rate in window I reduces to:

$$\overline{\Gamma_{\downarrow\leftarrow\uparrow}^{e,I}} = \frac{D_0^c L}{8\pi\hbar^2 v_{g\uparrow} l_B^2} = 1.2 \times 10^8 \text{s}^{-1}.$$

Here we have used the same values as above and taken $v_{g\uparrow} = 1.3 \times 10^4$ m/s.

The elastic scattering from the flat spin-up band (large initial density of states) into the sloped spin-down band in window III can be treated similarly. Hence, using the same parameters as above we get: $\overline{\Gamma_{\downarrow\leftarrow\uparrow}^{e,III}} = 1.2 \times 10^8 \text{s}^{-1}$.
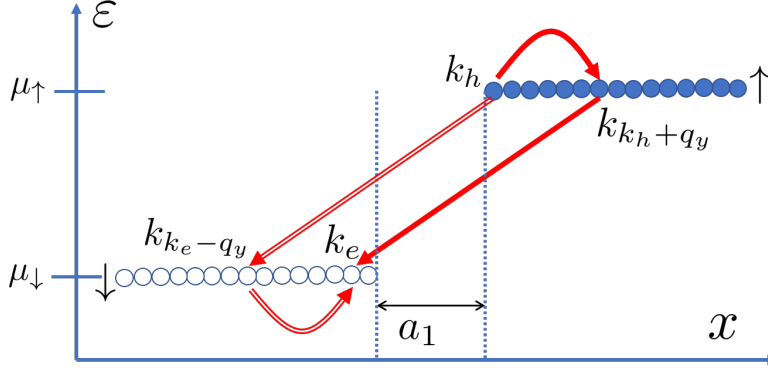
Figure 4.4: Set-up of the inelastic scattering calculation between the flat bands at reverse bias in the CSG model. The thick and the double thin line show the two interfering processes that give the same final state (same k_h, k_e, and q_y).

The last contribution to the total scattering rate we can calculate is the inelastic relaxation rate between the compressible strips. The set-up of this calculation is shown in Fig. 4.4. We use Eq. (3.31) to calculate this rate.

To simplify the calculation, we assume the parts of the spin-down and spin-up bands that we consider to be respectively completely empty and completely occupied. We assume both compressible strips to be at least several magnetic lengths long to treat them as infinitely long in the calculation. Using the CSG model [12], we calculated that the equilibrium width of the first compressible strip b_1 should be around 160 nm, which seems to justify our assumption. The energy difference between the occupied spin-up band and the empty spin-down band ΔE is the same for all pairs (k_h, k_e) and equal to $\Delta \mu$. In this set-up with flat bands, the intermediate energies $\varepsilon_{k_h+q_y\downarrow} - \varepsilon_{k_e\uparrow}$ and $\varepsilon_{k_h\downarrow} - \varepsilon_{k_e-q_y\uparrow}$ are also equal to $\Delta \mu$. The separation between the empty and occupied states closest to each other is equal to the incompressible strip width a_1, which increases as the bias becomes more negative [see Eq. (3.1)].

At a small bias, the magnitude of the phonon wavevector is small, and the piezo-electric mechanism [see Eq. (3.11)] is dominating the deformation potential one [see Eq. (3.12)]. The piezoelectric contribution goes down rapidly as the bias is made more negative because $\Delta \mu$ appears in the denominator. The values for the parameters that we use to calculate the inelastic relaxation rate are given in Tab. 4.2.

At small bias, $\Delta \mu = -\frac{1}{2}\Delta$, we calculate the inelastic relaxation rate between the flat bands to be:

$$\overline{\Gamma^i_{\downarrow\leftarrow\uparrow}} = 2.3 \times 10^8 \text{s}^{-1} + 2.4 \times 10^7 \text{s}^{-1} + 3.7 \times 10^6 \text{s}^{-1} = 2.6 \times 10^8 \text{s}^{-1}$$

where the first, second, and third term, respectively, are the piezoelectric transverse polarisation, piezoelectric longitudinal polarisation, and the deformation potential contributions. As a comparison: the rate at large negative bias, $\Delta \mu = -5\Delta$ is:

56

Parameter	Symbol	Value
Piezoelectric constant	h_{14}	1.38×10^9 V/m
Deformation potential	Ξ	13.7 eV
Mass density	ρ	5.3×10^3 kg/m^3
Transverse phonon velocity	v_t	3.0×10^3 m/s
Longitudinal phonon velocity	v_l	5.2×10^3 m/s

Table 4.2: Values of constants in the pre-factor of Eq. (3.31). Most values are taken from [42].

$$\overline{\Gamma^i_{\downarrow\leftarrow\uparrow}} = 4.2 \times 10^5 \text{s}^{-1} + 1.3 \times 10^5 \text{s}^{-1} + 2.0 \times 10^6 \text{s}^{-1} = 2.6 \times 10^6 \text{s}^{-1}$$

The total scattering rate at reverse bias is the sum of the rates calculated above. At $\Delta\mu = -\frac{1}{2}\Delta$, the result is:

$$\overline{\Gamma_{\downarrow\leftarrow\uparrow}} = \overline{\Gamma^{e,I}_{\downarrow\leftarrow\uparrow}} + \overline{\Gamma^{e,II}_{\downarrow\leftarrow\uparrow}} + \overline{\Gamma^{e,III}_{\downarrow\leftarrow\uparrow}} + \overline{\Gamma^i_{\downarrow\leftarrow\uparrow}} = 5.2 \times 10^8 \text{s}^{-1} \qquad (4.2)$$

We note that we did not include the total inelastic scattering rate. Moreover, we have overestimated the elastic scattering rates in windows I and III, and the inelastic scattering rate between the two flat bands by assuming the flat bands to be either completely empty or completely occupied.

4.2 Rates for forward bias

In this section, we calculate the scattering rates for the forward bias ($\Delta\mu > 0$) situation in both the naïve and the CSG model. Again, in all calculations, we assume the bulk filling factor ν_0 to be 2 unless explicitly stated otherwise.

4.2.1 Naïve model

Figure 4.5 shows the forward bias situation in the naïve model. We see that it is very similar to the reverse bias situation (see Fig. 4.1), only now the direction of the scattering is opposite.

In equivalence to the reverse bias case, the presence of degenerate states forbids us to calculate the inelastic scattering rate using the second-order FGR [see Eq. (3.8)]. Hence, in the naïve model, we only calculate the elastic scattering rate at forward bias.

We calculate the total elastic scattering rate $\overline{\Gamma^e_{\uparrow\leftarrow\downarrow}}$ in exactly the same way as we did for reverse bias. If we assume the same values for the parameters as we did for the reverse bias calculation (see tables 2.1 and 4.1), the scattering rate at small positive bias, $\Delta\mu = \frac{1}{2}\Delta$, will thus be:
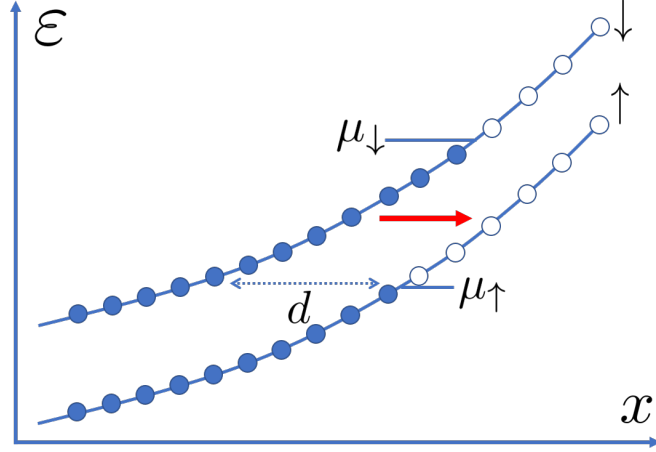
Figure 4.5: Forward bias situation in the naïve model.

$$\overline{\Gamma^e_{\uparrow\leftarrow\downarrow}} = \frac{LD_0^c\Delta\mu}{4\pi\sqrt{2\pi}\hbar^3 v_g^2 l_B}e^{-\frac{l_B^2\Delta^2}{2\hbar^2 v_g^2}} = 2.7\times10^5\mathrm{s}^{-1}.$$

4.2.2   CSG model

In the CSG model, the primary scattering mechanism at forward bias is inelastic scattering because there are few to none empty spin-up and occupied spin-down states at the same energy (see Figs. 3.3c and 3.3d). Herein, the CSG model differs strongly from the naïve model.

Using our Hartree-only simulations, we can qualitatively predict what the edge looks like in the CSG model under forward bias (see appendix B). We stress that in order to produce the CSG pictures, we switched off the Fock term in the simulations because the CSG model only includes the (classical) Hartree interaction.

At a small positive bias: $\Delta\mu = \frac{1}{2}\Delta$, empty spin-up states and occupied spin-down states that have the same energy are widely separated from each other by the outer (b_1) compressible strip (see Fig. 3.3c). Hence, we can neglect any elastic scattering. The spin-down electron density reaches zero at the edge-side of the second compressible strip, and the spin-up band is fully occupied at the bulk-side of the first compressible strip. Therefore, inelastic scattering is also strongly suppressed while $\Delta\mu < \Delta$. This explains the voltage threshold for forward bias below which virtually no scattering current is measured [9].

When the bias equals the spin-splitting: $\Delta\mu = \Delta$, the first incompressible strip has disappeared completely (see Sec. 3.1.1) and the first and second compressible strips have merged (see Figs. 4.6 and B.4). Suddenly, there are many empty spin-up states close
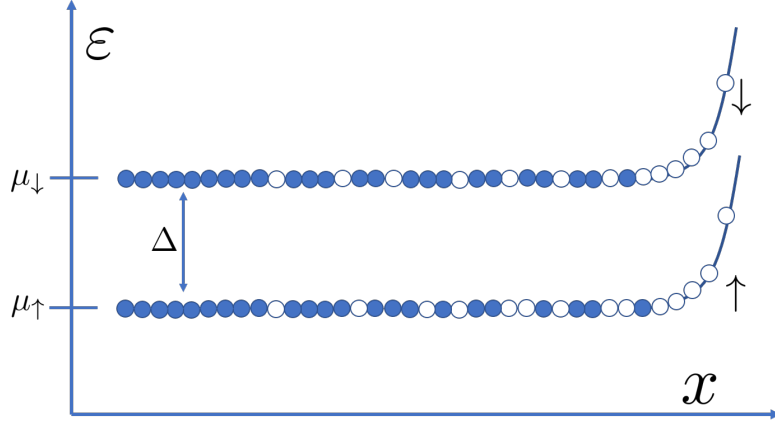
Figure 4.6: The band filling in the CSG model at the threshold bias $\Delta\mu = \Delta$. The incompressible strip has disappeared compared to Fig. 3.3c.
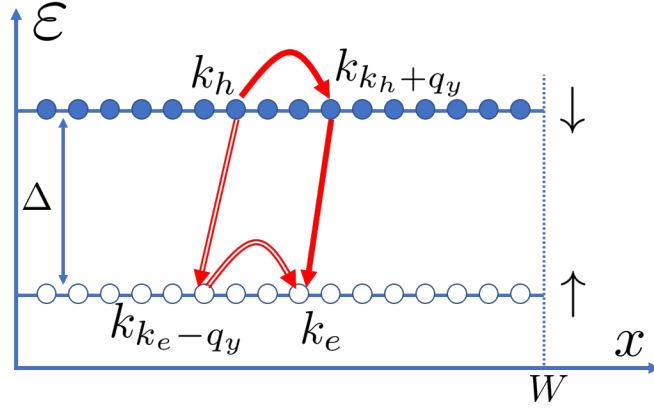

Figure 4.7: Inelastic scattering for two flat bands. For a given final state (defined by k_h, k_e, and q_y), the two interfering paths are drawn, one with thick lines and one with double thinner lines.

to occupied spin-down states, which causes the inelastic scattering to become significant.

When the bias is larger than the spin splitting: $\Delta\mu > \Delta$, the Hartree-only simulations show that a new compressible strip forms (see Figs. 3.3d and B.5). This gives us a strip where occupied spin-down states are above empty spin-down states.

We will now calculate the inelastic relaxation rate for this 'overhang' region. The set-up of the calculation is shown in Fig. 4.7. Since we are only interested in an order-of-magnitude estimate, we simplify the calculation by assuming the spin-down band is fully occupied. (In reality, the density of this band varies from 0 at the edge-side of the overhang region to n_L at the bulk-side of the overhang region.) We also ignore the incompressible strip part where the bands are sloped.

Again, we use 3.31 to determine the inelastic scattering rate. In appendix B, we estimate that at $\Delta\mu = 1.5\Delta$, the width of the overhang region (W in Fig. 4.7) is about 200 nm. In this simplification, the energy difference ΔE [see Eq. (3.28)] and the intermediate energies are always equal to the spin-splitting energy Δ. Furthermore, the sign-function $\mathfrak{S}(k_h, k_e, \theta, \phi, p)$ is always equal to $+1$. Using the same parameters as for the reverse bias inelastic calculation (see tables 2.1, 4.1 and 4.2), we obtain for the inelastic scattering rate:

$$\overline{\Gamma^i_{\downarrow \leftarrow \uparrow}} = 4.7 \times 10^9 \mathrm{s}^{-1} + 7.4 \times 10^8 \mathrm{s}^{-1} + 4.5 \times 10^8 \mathrm{s}^{-1} = 5.9 \times 10^9 \mathrm{s}^{-1}$$

where the first, second, and third term, respectively, are the piezoelectric transverse polarisation, piezoelectric longitudinal polarisation, and the deformation potential contributions.

We note that this is not the total inelastic scattering rate. Another contribution to this rate will come from the scattering in the second compressible strip (see, for example, the right part of Fig. B.5a). Here we have, similar to the threshold bias configuration, a fully occupied spin-down band on top of a partially filled spin-up band. Still, we believe that this estimate gives the correct order of magnitude for the total inelastic scattering.

In appendix B we discuss the bias-dependence of the overhang width. Furthermore, it seems that a larger bias makes the overhang region wider and opens up a window for elastic scattering. However, since there are too many unknowns to extract any quantitative relation from the simulations, we do not calculate the bias dependence of the inelastic scattering rate here.

4.3 Comparison of models

The main way to judge the predictions of the different models is by comparing them to experimental results. In Sec. 2.3.1, we discussed the relation between the measured scattering current and the scattering rate. Simply put, the scattering current divided by the electron charge (= number of electrons per second) equals the scattering rate.

Many assumptions (e.g., linearisation) in our calculations rely on the bias being small, and our theory might break down at large bias. Hence, we prefer to compare our calculations to measurements at a small bias when possible.

First we compare the calculated scattering currents with the Dixon et al. experiment [9] at small bias: ± 0.14 mV. In the IV curve in Fig. 2.12 we see that the scattering current at ± 0.14 mV is at least below -0.5 nA. At $\Delta\mu = -0.14$ meV, the naïve and CSG model calculations respectively predict a scattering current of around -0.04 pA and -0.1 nA. At $\Delta\mu = +0.14$ meV, the naïve calculation predicts a scattering current of around $+0.04$ pA, and the CSG model predicts there to be no observable scattering current (threshold).

We also venture to compare our calculations and the Dixon et al. experiment at forward bias larger than the threshold: $\Delta\mu = +0.41$ meV. Our calculations predict a

scattering current of +0.95 nA solely from the overhang region. In comparison, the Dixon et al. IV curve gives a scattering current of around +2 nA at +0.4 mV.

In the Wald et al. experiment [8], the scattering conductance becomes half the conductance quantum for a bias strength of around 0.2 mV and higher. This is a signature of complete equilibration between the spin-up and spin-down channels in the scattering region. The sudden increase of the scattering current reminds us of the threshold described in the Dixon et al. experiment. The total ballistic current carried by the spin-up channel at ± 0.2 mV is ± 7.7 nA. At $|V| > 0.2$ mV, we would thus expect a scattering current of ± 3.9 nA.

The CSG model performs better on a qualitative level because it explains the observed threshold voltage for forward bias. Also, on a quantitative (order-of-magnitude) level, the scattering rates calculated in the CSG model come closer to the experimental observations by Dixon et al. and Wald et al.. We understand the larger rates in the CSG model through the *number of scattering options*. We note that at $\Delta \mu = -0.14$ meV, the largest contribution to the elastic scattering rate in the CSG model comes from scattering into/from the compressible strips (see Sec. 4.1.2). Therefore, even if the velocity v_g that we assumed in the naïve model calculation was too large, and if we would instead use the same velocity as in the CSG calculation, the elastic rate predicted by the CSG model would still be much larger because of the larger number of scattering options.

We note that in naïve model calculations, we left out inelastic scattering altogether. In the CSG calculations, we left out part of the inelastic calculation. However, including inelastic scattering fully in both models would not change which of the two predicts the larger rate. The inelastic rate in the CSG model will always be larger than that in the naïve model due to the larger number of scattering options.

Chapter 5

Discussion and outlook

In this thesis, we calculated scattering rates for the hyperfine-mediated scattering between the spin-up and spin-down LLs at the edge of an IQHE-system. We considered a naïve model that neglects e-e interactions, the CSG model that takes these interactions into account semi-classically, and a third model that also considers the quantum mechanical exchange part of these interactions. We set up elastic and inelastic calculations for the first two models. By comparing to experiments, we found that the CSG model is better suited to describe the spin-scattering both quantitatively and qualitatively.

No scattering rates were calculated for the third model because there is no consensus on the effect of the exchange interaction on the edge structure. On the one hand, Hartree-Fock methods [25, 26, 27] usually predict a radically different edge structure. We also showed this ourselves. On the other hand, experiments do not consistently observe this predicted effect. Using a finite-width $\hat{z}$-direction wave function in the HF simulations might be the (partial) resolution of this inconsistency. The $\hat{z}$-broadening would allow electrons to avoid each other more and thus reduces the short-range Fock interaction [46]. In general, more work needs to be done to understand the effect of interactions beyond the Hartree-term on the edge structure. It would be helpful to use methods other than Hartree-Fock (perhaps the density-matrix renormalisation group (DMRG) method [47]) to obtain a new perspective and judge whether the Hartree-Fock approximation is overestimating the exchange contribution or not.

One missing ingredient in the calculation of the total spin-scattering rate is the inelastic scattering rate between spin-bands with degenerate states. In such situations, the non-degenerate perturbation theory on which the second-order FGR [see Eq. (3.8)] is based breaks down. The inelastic calculation can probably be performed by including the level-broadening of the electron states due to their finite lifetime. This finite lifetime is caused by the spin-flip and phonon-emission processes themselves.

Having studied spin-scattering in the IQHE, the next step would be to apply what we learnt to the FQHE case. Chang [16] and Beenakker [15] have described FQHE systems

in terms of alternating compressible and incompressible bands. It would be interesting to investigate this analogy with the CSG model to see if we can carry over any of the calculations performed in this thesis. We expect the Luttinger liquid theory to be suitable for the treatment of scattering in the FQHE [28, 29]. Hence, it would be a good start to first formulate the IQHE spin-scattering calculations in the Luttinger liquid picture.

Suppose we understand spin-scattering and the dynamical creation of nuclear polarisation. In that case, many other questions that were posed in the introduction still need to be answered before we can understand the intriguing long time-scale temporal oscillations in FQHE systems [10, 7] that motivated this thesis.

In our IQHE models, we have not yet included the feedback of the created nuclear polarisation. However, in the aforementioned FQHE experiments, a time- and position-dependent nuclear polarisation is assumed to play an important role. Hence, it would be of great interest to include the nuclear feedback on the spin-scattering rate [48] already in the IQH model.

Flip-flop scattering is only one of the mechanisms affecting the local nuclear polarisation. In order to calculate nuclear polarisation as a function of position and time, other mechanisms that affect nuclear polarisation need to be included. For example: diffusion due to nuclear dipole-dipole interactions [36, 49], and the spin-phonon coupling [48]. We tried to derive a steady-state nuclear profile given some creation rate (the spin-scattering rate) and a diffusion term. However, without a decay term, there is no steady-state profile other than that the entire sample becomes fully polarised at infinite time. The effects of diffusion and other mechanisms on nuclear polarisation still need to be better understood.

Appendix A

Electrochemical potentials of the bands in the scattering region

In this appendix, we show that the electrochemical potentials of the spin-up and spin-down channels at the start of the scattering region are equal to the electrochemical potentials of the contacts these channels are equilibrated with. The argument relies on the conservation of current and the relation between the local current and the slope of the dispersion relation [see Eq. (2.11)]. It applies both to systems of interacting and non-interacting electrons.

We take the experimental set-up of the Dixon et al. experiment [9] and assume that $\mu_1 > \mu_3$ such that there is a net electron current flowing from contact 1 to contact 3. The A and C gates and the AC-QPC have been fully depleted to simplify the argument. Figure A.1 illustrates this set-up. Figure A.2 shows a cross-section of the QPC with the corresponding filling of the bands.

The regions between contact 1 and the AB-QPC, and between contact 3 and the AB-QPC are at $\nu = 2$. The AB-QPC and the B gate are tuned to $\nu = 1$ and only let spin-up electrons through. However, not the entire spin-up current coming from contact 1 flows through the AB-QPC. Only the current carried by electrons with an energy above the energy of the QPC bottom flows through the QPC (see current ib in Fig. A.1). The other spin-up electrons stay in the region between contact 1 and the AB-QPC (current ia in Fig. A.1). For the electrons coming from contact 3, the story is similar. The current carried by electrons with an energy above the energy of the QPC bottom flows through the QPC (current iib in Fig. A.1), and the rest of the current (iia) flows along the gate B. The key point is now that all spin-up electrons feel the same QPC bottom energy. Therefore, the states along the ia and iia edge are both filled up until the same QPC bottom energy.

In the AB-QPC, the spin-up band at the edge bordering the A gate is filled up until μ_1. The spin-up current flowing through the QPC in the direction from contact 1 to contact 3 (ib) is proportional to the total slope height [see Eq. (2.12)]: the energy difference between μ_1 and the QPC bottom energy. The spin-up current flowing the
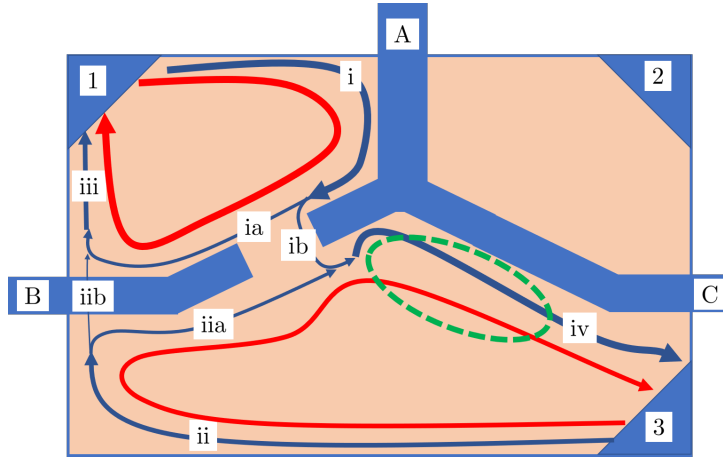
Figure A.1: The edge channels and current flow in the Dixon et al. sample [9] at reverse bias ($\mu_1 > \mu_3$). The A and C gates and the AC-QPC have been fully depleted to simplify the argument. The spin-up current is indicated by blue lines and the spin-down current by red lines. Note that the lines originating from contact 1 are thicker than the ones originating from contact 3. The scattering region is encircled by a green dotted line.
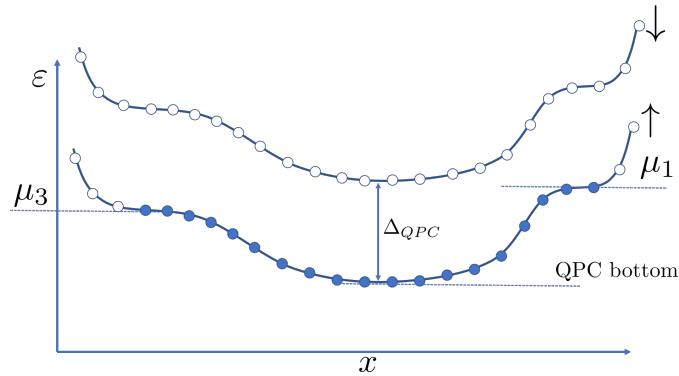

Figure A.2: The cross-section of the AB-QPC in Fig. A.1. The electrons that flow on the left and right slope respectively constitute the currents iib and ib.

other way (iib) is proportional to the energy difference between μ_3 and the QPC bottom energy. Consequently, the net electron current i-ii = ib-iib flowing through the AB-QPC is proportional to $\mu_1 - \mu_3$.

At the start of the scattering region, the spin-up current ib coming from contact 1 joins the spin-up current iia from contact 3 that did not make it through the AB-QPC (and which has an effective electrochemical potential equal to the QPC bottom energy). Because the ib current is conserved, the spin-up band at the start of the scattering region (before any scattering has taken place) should also be filled up until μ_1. This also makes a lot of sense from the perspective of an individual electron that flows from contact 1, through the AB-QPC, to the scattering region. This electron has a certain energy and

follows an equipotential path if it does not dissipate any energy.

As can be seen from a simpler but similar current-conservation argument, the spin-down band should be filled until μ_3 at the start of the scattering region.

Finally, we note by looking at Fig. A.2 that we can only realise a limited range of bias situations in this sample geometry. For example, if we make μ_1 too large in the reverse bias ($\mu_1 > \mu_3$) case, we see that spin-down electrons will start to flow through the QPC on the right edge. Moreover, when we set μ_1 below the QPC bottom in the forward bias scenario, no spin-up electrons flow through the QPC at the right edge. Hence, the electrochemical potential μ_1 is not 'communicated' to the scattering region. This latter problem can be solved by lowering the QPC bottom by changing the gate voltages A and B. However, we seem to be getting into trouble when the electrochemical potential difference exceeds the spin splitting within the QPC: $\Delta\mu > \Delta_{QPC}$ [25]. Here Δ_{QPC} is the spin-splitting within the QPC, which might be significantly larger than the bare spin-splitting ($E_z = g\mu_B B$) due to exchange enhancement (see Sec. 2.2.3).

Appendix B

HF analysis

We apply the Hartree-Fock method to the electrons near the edge and investigate whether this method gives alternating compressible and incompressible strips as in the CSG model. We also use the HF simulations to produce non-equilibrium pictures of the edge (see Fig. 3.3).

B.1 The Hartree-Fock method

In the Hartree-Fock method we are looking for the uncorrelated (Slater-determinant) state $|\Psi_{MF}\rangle = (\prod_i \xi_i^\dagger)|0\rangle$ that has the lowest possible energy. The single-particle orbitals $\{|i\rangle\}$ are in principle to be determined by the method. In our calculation, however, we *fix* what these single-particle orbitals are, namely the eigenstates of the system without the external potential: the Landau level basis states. We furthermore first restrict our attention to the LLL (see justification in Sec. 3.1.1). The eigenstates of the LLL are given in Eq. (2.9).

The full Hamiltonian of the system is:

$$H = H_0 + V_{ee} + V_0, \tag{B.1}$$

and contains a term H_0, of which the LLL eigenstates are the exact eigenstates, an external potential term V_0 and an electron-electron interaction term V_{ee}.

In the HF approximation, we can write down a second-quantised mean-field Hamiltonian of Eq. (B.2) in the LLL basis:

$$H_{MF} = \sum_{\alpha\sigma}(\frac{1}{2}\hbar\omega_c + \delta_{\sigma\downarrow}\Delta)a_{\alpha\sigma}^\dagger a_{\alpha\sigma} + \sum_{\alpha,\beta,\sigma}\int d\vec{r}V_0(\vec{r})\phi_\alpha^*(\vec{r})\phi_\beta(\vec{r})a_{\alpha\sigma}^\dagger a_{\beta\sigma}$$

$$+ \sum_{\alpha,\beta,\sigma,\sigma'}\int d\vec{r}V_H(\vec{r})\phi_\alpha^*(\vec{r})\phi_\beta(\vec{r})a_{\alpha\sigma}^\dagger a_{\beta\sigma} - \sum_{\alpha,\beta,\sigma,\sigma'}\int d\vec{r}\int d\vec{r'}V_F(\vec{r},\vec{r'})\phi_\alpha^*(\vec{r})\phi_\beta(\vec{r'})a_{\alpha\sigma}^\dagger a_{\beta\sigma'},$$

$$\tag{B.2}$$

where the operators $a_{\alpha\sigma}^\dagger$ and $a_{\alpha\sigma}$ respectively create and annihilate a particle in LLL state $|k_\alpha\sigma\rangle$. The corresponding spatial wave function $\phi_\alpha(\vec{r})$ of this state is given by Eq. (2.9). The spin-splitting Δ is also included in the first term. The Hartree potential in Eq. (B.2) is given by:

$$V_H(\vec{r}) = \int d\vec{r'}V_{ee}(\vec{r}-\vec{r'})\left\langle \Psi_{\sigma'}^\dagger(\vec{r'})\Psi_{\sigma'}(\vec{r'})\right\rangle_{MF} = \sum_{\gamma\in occ}\int d\vec{r'}V_{ee}(\vec{r}-\vec{r'})|\phi_\gamma(\vec{r'})|^2, \quad (B.3)$$

and the Fock potential by:

$$V_F(\vec{r},\vec{r'}) = V_{ee}(\vec{r}-\vec{r'})\left\langle \Psi_{\sigma'}^\dagger(\vec{r'})\Psi_\sigma(\vec{r})\right\rangle_{MF} = \sum_{\gamma\in occ}V_{ee}(\vec{r}-\vec{r'})\phi_\gamma^*(\vec{r'})\phi_\gamma(\vec{r})\delta_{\sigma\sigma'}, \quad (B.4)$$

where $\langle...\rangle_{MF}$ indicates the expectation value with respect to the many-body state $|\Psi_{MF}\rangle$. Note that the Fock interaction is only non-zero between particles of the same spin-species: $\sigma = \sigma'$. The Coulomb interaction (leaving out the pre-factor $\frac{e^2}{4\pi\epsilon_0}$) is given by:

$$V_{ee}(\vec{r}-\vec{r'}) = \frac{1}{|\vec{r}-\vec{r'}|} = \frac{1}{\sqrt{(x'-x)^2+(y'-y)}}. \quad (B.5)$$

We observe that the mean-field Hamiltonian in Eq. (B.2) is not necessarily diagonal in the LLL basis. When we derived the LL eigenstates, we assumed periodic boundary conditions in the $\hat{y}$-direction. However, the system we are dealing with is still rectangular. 'Rolling up the system' and using a cylindrical coordinate system removes this inconsistency and yields a diagonal mean-field Hamiltonian.

B.1.1 Use of cylindrical coordinate system

We get the cylindrical coordinate system when we start with the flat sample in a 2D (x,y) cartesian coordinate system of dimensions (W,L) and then fold the $y = 0$ edge the $y = L$ onto the edge so that we get a hollow cylinder of radius $R = L/2\pi$ in a 3D coordinate system:

$$(\tilde{x},\tilde{y},\tilde{z}) = (\tilde{x}, R\sin\theta, R\cos\theta), \quad (B.6)$$

that is open on both ends. The old 2D coordinate now lives on the surface of this cylinder and the y-coordinate has become periodic such that $y = y + L$; the x-coordinate is as before:

$$y = R\theta, \qquad x = \tilde{x}. \quad (B.7)$$

Using this coordinate system is consistent with the choice for periodic boundary conditions in the y-direction when we derive the LLL basis states (see Sec. 2.1).

The Coulomb interaction [see Eq. (B.5)] is inversely proportional to the distance between two particles. However, using this cylindrical coordinate system changes the notion of distance between two particles:

$$V_{ee} = \frac{1}{\sqrt{(\tilde{x}'-\tilde{x})^2 + (\tilde{y}'-\tilde{y})^2 + (\tilde{z}'-\tilde{z})^2}} = \frac{1}{\sqrt{(x'-x)^2 + 4R^2\sin^2(\frac{\theta'-\theta}{2})}}. \quad \text{(B.8)}$$

When R is large, the Coulomb interaction energy hardly changes with respect to the original coordinate system, which justifies the cylindrical coordinate system for large L. Using this cylindrical coordinate system, the mean-field Hamiltonian of Eq. (B.2) becomes diagonal in the LLL basis because the system itself is now truly periodic in the $\hat{y}$-direction. We show this by calculating both the Hartree and Fock interaction energies that appear in the mean-field Hamiltonian. The α, β element of the Hartree interaction energy in Eq. (B.2) is:

$$\int d\vec{r} V_H(\vec{r})\phi_\alpha^*(\vec{r})\phi_\beta(\vec{r}) =$$

$$\sum_{\gamma\in occ} \frac{1}{L^2}\frac{1}{\pi l^2} \int_\infty^\infty dx \int_\infty^\infty dx' \int_0^L dy \int_0^L dy' V_{ee}(\vec{r}-\vec{r'}) e^{\frac{-(x'-x_\gamma)^2}{l^2}} e^{\frac{-(x-x_\alpha)^2}{2l^2}} e^{\frac{-(x-x_\beta)^2}{2l^2}} e^{-i(k_\alpha-k_\beta)y},$$
$$\text{(B.9)}$$

where we can take the x-integrals from minus infinity to infinity because we have Gaussians (centred at $x_\gamma = -k_\gamma l^2$) which localise the integrand in the $\hat{x}$-direction. Using the cylindrical coordinate system discussed above, this becomes:

$$\sum_{\gamma\in occ} \frac{1}{(2\pi)^2}\frac{1}{\pi l^2} \int_\infty^\infty dxdx' \int_0^{2\pi} d\theta d\theta' \frac{e^{\frac{-(x'-x_\gamma)^2}{l^2}} e^{\frac{-(x-x_\alpha)^2}{2l^2}} e^{\frac{-(x-x_\beta)^2}{2l^2}} e^{-i(k_\alpha-k_\beta)R\theta}}{\sqrt{(x'-x)^2 + 4R^2\sin^2(\frac{\theta'-\theta}{2})}}. \quad \text{(B.10)}$$

We now change coordinates to the difference and average of both coordinates:

$$u_x = x' - x \quad v_x = \frac{x'+x}{2} \qquad u_\theta = \theta' - \theta \quad v_\theta = \frac{\theta'+\theta}{2}. \quad \text{(B.11)}$$

This allows us to solve the v_θ integral:

$$\int_0^{2\pi} dv_\theta e^{-i(k_\alpha-k_\beta)Rv_\theta} = \int_0^{2\pi} dv_\theta e^{-im\frac{2\pi}{L}\frac{L}{2\pi}v_\theta} = 2\pi\delta_{m,0} \to 2\pi\delta_{\alpha,\beta},$$

where m is an integer. The v_x integral can also be solved by completing the square and combining the exponentials. Hence, we obtain for the Hartree interaction energy:

$$\int d\vec{r} V_H(\vec{r})\phi_\alpha^*(\vec{r})\phi_\beta(\vec{r}) = \delta_{\alpha,\beta} \sum_{\gamma\in occ} \sqrt{\frac{\pi}{2}}\frac{1}{2\pi^2 l} \int_\infty^\infty du_x \int_0^{2\pi} du_\theta \frac{e^{\frac{-[u_x+(x_\alpha-x_\gamma)]^2}{2l^2}}}{\sqrt{u_x^2 + 4R^2\sin^2(\frac{u_\theta}{2})}}. \quad \text{(B.12)}$$

This proves the diagonality of Eq. (B.10). The resulting 2D integral in Eq. (B.12) is solved numerically. Note that this result is translationally invariant as it should be: it only depends on the difference coordinates u_x and u_θ.

We can calculate the Fock interaction energy term in Eq. (B.2) in the cylindrical coordinate system in a very similar way. For the Fock term we can also arrive at a translationally invariant 2D integral that can be solved numerically:

$$\int d\vec{r} \int d\vec{r'} V_F(\vec{r}, \vec{r'}) \phi_\alpha^*(\vec{r}) \phi_\beta(\vec{r'})$$
$$= \delta_{\alpha,\beta} \delta_{\sigma\sigma'} \sum_{\gamma \in occ} \sqrt{\frac{\pi}{2}} \frac{1}{2\pi^2 l} \int_\infty^\infty du_x \int_0^{2\pi} du_\theta \frac{e^{i(k_\alpha - k_\gamma)Ru_\theta}}{\sqrt{u_x^2 + 4R^2 \sin^2(\frac{u_\theta}{2})}} e^{\frac{-u_x^2}{2l^2}} e^{\frac{-(x_\alpha - x_\gamma)^2}{2l^2}}. \quad \text{(B.13)}$$

We assumed that the external potential $V_0(x)$ only depends on the x-coordinate (the direction in which the external potential confines the 2DEG). This makes external potential term - which we will refer to as V_0^α - in Eq. (B.2) also diagonal:

$$V_0^\alpha = \int d\vec{r} V_0(\vec{r}) \phi_\alpha^*(\vec{r}) \phi_\beta(\vec{r}) = \delta_{\alpha,\beta} \frac{1}{\sqrt{\pi} l} \int_{-\infty}^\infty dx V_0(x) e^{\frac{-(x-x_\alpha)^2}{l^2}}. \quad \text{(B.14)}$$

We have shown that the Hartree, Fock, and external potential terms in Eq. (B.2) are all diagonal in $\{\alpha, \beta\}$. Both the Hartree [see Eq. (B.12)] and Fock [see Eq. (B.13)] terms include a sum over all occupied orbitals $\{\gamma\}$. Because the interactions between orbital α and the orbitals $\{\gamma\}$ simply add, we can define the energies $V_H^{\alpha,\gamma}$ and $V_F^{\alpha,\gamma}$ that respectively represent the Hartree and Fock interaction energies between a particle on site $|\alpha\sigma\rangle$ and one on site $|\gamma\sigma'\rangle$. Using these energies, we can write the mean-field Hamiltonian as follows:

$$H_{MF} = \sum_{\alpha\sigma} \left[\left(\tfrac{1}{2}\hbar\omega_c + \delta_{\sigma\downarrow}\Delta \right) + V_0^\alpha + \sum_{|\gamma\sigma'\rangle \in occ} (V_H^{\alpha,\gamma} - V_F^{\alpha,\gamma}) \right] a_{\alpha\sigma}^\dagger a_{\alpha\sigma}, \quad \text{(B.15)}$$

where the Hartree and Fock interaction energies are defined as:

$$V_H^{\alpha,\gamma} = \sqrt{\frac{\pi}{2}} \frac{1}{2\pi^2 l} \int_\infty^\infty du_x \int_0^{2\pi} du_\theta \frac{e^{\frac{-[u_x + (x_\alpha - x_\gamma)]^2}{2l^2}}}{\sqrt{u_x^2 + 4R^2 \sin^2(\frac{u_\theta}{2})}},$$
$$V_F^{\alpha,\gamma} = \delta_{\sigma\sigma'} \sqrt{\frac{\pi}{2}} \frac{1}{2\pi^2 l} \int_\infty^\infty du_x \int_0^{2\pi} du_\theta \frac{e^{i(k_\alpha - k_\gamma)Ru_\theta}}{\sqrt{u_x^2 + 4R^2 \sin^2(\frac{u_\theta}{2})}} e^{\frac{-u_x^2}{2l^2}} e^{\frac{-(x_\alpha - x_\gamma)^2}{2l^2}}. \quad \text{(B.16)}$$

This mean-field Hamiltonian is purely diagonal in the LLL basis.

We assumed the LLL states to be the optimal single-particle orbitals. Hence, what is left for us to do is figure out the optimal way to fill these single-particle states.

B.2 The code

The basic equilibrium code finds the filling of the single-particle states given an electrochemical potential μ that applies to both spin-bands. The non-equilibrium code finds the filling given two different electrochemical potentials: $\mu_\uparrow$ for spin-up and $\mu_\downarrow$ for spin-down.

B.2.1 Interaction energies

The code uses pre-calculated $\alpha\gamma$-matrices for the Hartree $V_H^{\alpha,\gamma}$ and Fock $V_F^{\alpha,\gamma}$ interaction energies. Figure B.1 shows the interaction energies between a particle in the $|\alpha\sigma\rangle$ state, which has a transverse wave function centred at $X_{k_\alpha} = 0$, and a particle in the $|\gamma\sigma\rangle$ centred at X_{k_γ}.

We see that the Fock interaction energy dies off over a very short distance compared to the Hartree interaction energy. When the x-separation between the two sites is much larger than the radius R of the two rings in the cylindrical coordinate system, the Hartree interaction energy will start to look more and more like the interaction energy between two point charges $V_H^{\alpha,\gamma} \propto \frac{1}{x}$ (a ring looks just like a point when seen from afar). We can use this to extrapolate the interaction energy for sites that are very far apart.

For the external potential $V_0(x)$ [see Eq. (B.14)] we generally choose a smooth Gaussian function. We choose this function such that it provides an electric field of around 10^6 V/m in the depleted region [see Eq. (2.13)] [12].
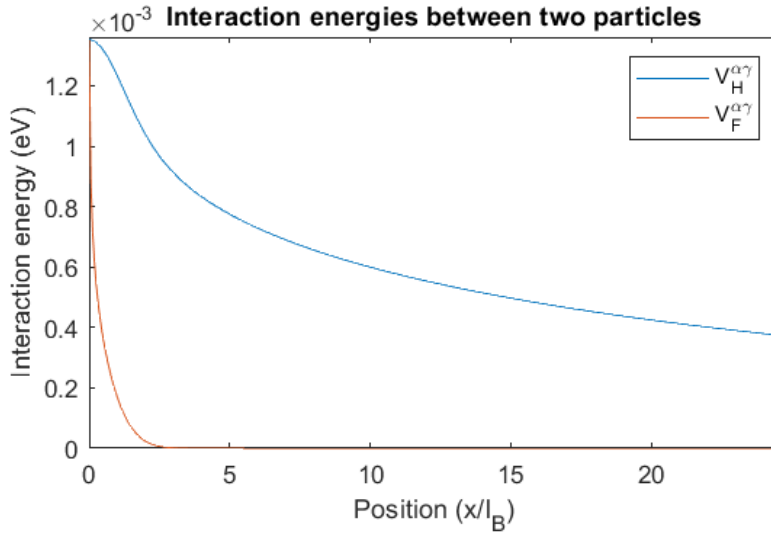

Figure B.1: The interaction energy between a particle in a state centred at $x = 0$ and one centred at x. For this calculation, the system length L was taken to be 1 μm and the magnetic length 10 nm.

B.2.2   Total and single-particle energies

We note that if we try to calculate the energy of a many-body state by taking the expectation value of the expression in Eq. (B.15) with respect to this state, we double-count the interaction terms. For example: if only orbitals 1 and 2 are occupied, we get both $V_H^{1,2}$ and $V_H^{2,1}$, which are equal to each other. Hence, the total energy of the system is given by:

$$E_{tot} = \sum_{|\alpha\sigma\rangle \in occ} \left[\left(\tfrac{1}{2}\hbar\omega_c + \delta_{\sigma\downarrow}\Delta \right) + V_0^\alpha + \sum_{|\gamma\sigma'\rangle \in occ} \frac{1}{2}(V_H^{\alpha,\gamma} - V_F^{\alpha,\gamma}) \right]. \tag{B.17}$$

We define the single-particle energies that are used in the HF code in the following way:

$$E_{\alpha\sigma} = \delta_{\sigma\downarrow}\Delta + \sum_{|\gamma\sigma'\rangle \in occ} (V_H^{\alpha,\gamma} - V_F^{\alpha,\gamma}) + V_0^\alpha \tag{B.18}$$

We leave out the cyclotron energy $\frac{1}{2}\hbar\omega_c$ because it is the same for all particles in the system. These single-particle energies $E_{\alpha\sigma}$ have different meanings for occupied and empty states.

For the unoccupied sites, the single-particle energy $E_{\alpha\sigma}$ tells us what the energy increase of the system would be if we were to add a particle to the system at this site while *freezing* the other particles at their current positions. This means that we do not let the system evolve to a possibly distinct configuration. Note that as we calculate these 'addition' energies for the individual sites, we are not double-counting the interaction energies.

For the occupied sites, the single-particle energy $E_{\alpha\sigma}$ is an 'ionisation' energy that corresponds to the energy reduction of removing a particle from this site while *freezing* the resulting state with one particle less. Again, in reality, the resulting state would possibly evolve to a different configuration with lower total energy.

B.2.3   Iteration strategies

We find the equilibrium distribution by starting with an empty system and setting an electrochemical potential. We then add one electron to the unoccupied single-particle state with the lowest energy $E_{\alpha\sigma}$. After adding the particle, we update the entire single-particle energy landscape [see Eq. (B.18)]. We iterate this procedure until the energy of the lowest energy empty state is above the electrochemical potential.

In the non-equilibrium case, we first find the equilibrium distributions for both $\mu_\uparrow$ and $\mu_\downarrow$. We then take the filling for the spin-up band from the $\mu_\uparrow$ distribution and the filling of the spin-down band from the $\mu_\downarrow$ distribution, and put them together. Subsequently, we update the single-particle landscape [see Eq. (B.18)]. When $\mu_\uparrow > \mu_\downarrow$, we find that the largest single-particle energy $E_{\alpha\uparrow}^{max}$ is now below $\mu_\uparrow$, and the largest single-particle energy $E_{\alpha\downarrow}^{max}$ is above $\mu_\downarrow$. This means that we have to add electrons to the spin-up band and remove them from the spin-down band. We do this by iterating the following algorithm: add one electron to the empty spin-up state with the lowest single-particle

energy, update the single-particle energies, remove one electron from the occupied spin-down state with the largest single-particle energy, update the single-particle energies. Note that each added electron increases the mean-field energy for *all* the other electrons in the system, while each removed electron lowers it. We iterate this algorithm until $E_{\alpha\uparrow}^{max}$ and $E_{\alpha\downarrow}^{max}$ are respectively equal to $\mu_\uparrow$ and $\mu_\downarrow$, or at least as close as is possible in a discrete system using this method.

B.2.4   Equilibrium simulation results

Figure B.2 shows that our HF calculation yields flat compressible and sloped incompressible strips. In the compressible strips, the particle density development (see Fig. B.2c) is such that the external field is screened out. We cannot say anything definite about the functional shape of the electron density. However, it shows similarities to the square-root-like density development predicted by the CSG model (see Fig. 2.8).

In the top right panel of Fig. B.2 we see how the spin-splitting Δ between the spin-bands depends on the local filling factor. This is explained by the exchange enhancement of the spin-splitting, which is very large because the Zeeman splitting is tiny compared to the Coulomb energy (see estimates in Sec. 3.1.1).

The fact that both bends bend down on the right in Fig. B.2 is a consequence of the finite size of the simulated system. This feature can be ignored.

The interaction energy between two electrons of the same species is $V_H^{\alpha,\gamma} - V_F^{\alpha,\gamma}$ [see Eq. (B.18)]. In Fig. B.1 we can see that it is therefore energetically favourable for electrons of the same spin species to sit right next to each other (or very far apart). This explains why the electrons group together in 'pockets', as shown in the top right panel of Fig. B.2. We understand this pocket formation as a particularity of the HF method in this discrete system that does not carry any further physical significance.

B.2.5   Hartree-only simulation

We now briefly discuss some complications in the Hartree-only version of the simulation that already show up at equilibrium. In the Hartree-only simulation, the result looks a bit odd compared to the Hartree-Fock result (compare figures B.2b and B.3a and note the different energy scales on the vertical axes). The energy fluctuations that are visible in the Hartree-only result (see Fig. B.3a) need some explaining.

The fluctuation of the single-particle energies in the compressible strip is because the mean-field potential itself is fluctuating. These fluctuations show that there are many nearly degenerate configurations of which our simulation just found a single representative.

These energy fluctuations are so small that they would normally go unnoticed if it were not for the smallness of the spin-splitting. When we only consider the Hartree term, the spin-splitting energy is the bare one, which is very small compared to the interaction energies between the different sites. Hence, the fluctuations of the mean-field show up very dramatically (see Fig. B.3a).
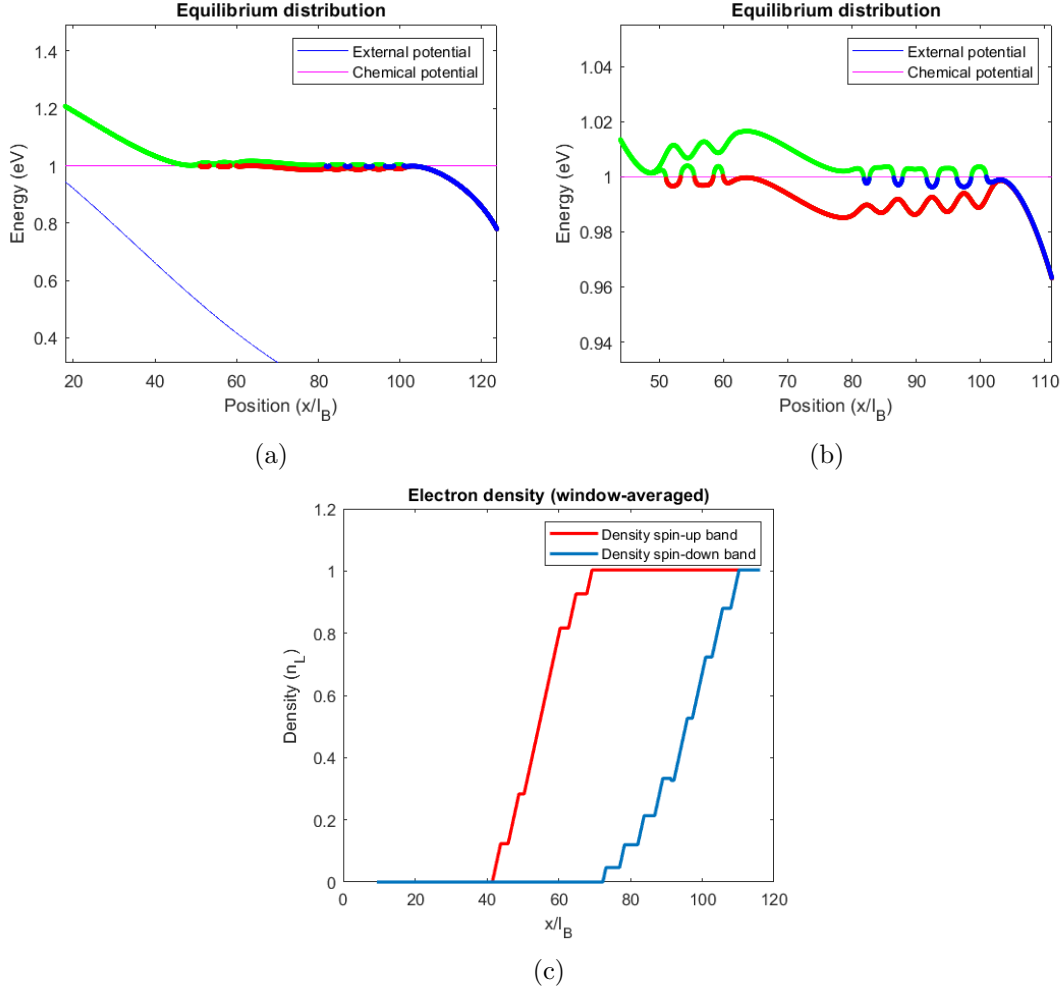
Figure B.2: Equilibrium distribution result of the HF code. The top right panel is a zoom-in of the bands in the top left panel. The following parameters were used: $L = 1$ μ m, $l_B = 10$ nm, $\Delta = 0.27$ meV ($B = 7$ T). The red and blue dots (which show up as lines because there are so many) respectively represent the filled spin-up and spin-down states with ionisation energies $E_{\alpha\uparrow}$ and $E_{\alpha\downarrow}$ [see Eq. (B.18)]. The green dots represent the addition energies $E_{\alpha\sigma}$ [see Eq. (B.18)] of the still empty states. At the point where the electron density becomes non-zero, the electric field strength is about 1×10^6 V/m. The lower panel shows the development of the electron density. We used a windowed-average to ignore the pocket feature.

We think that adding a small temperature and then averaging over the different thermal configurations will remove these fluctuations. However, our goal with this HF analysis is not to produce any quantitative predictions. Therefore, we decided to use a quick fix: we visually removed the fluctuations by adding a homogeneous (not dependent
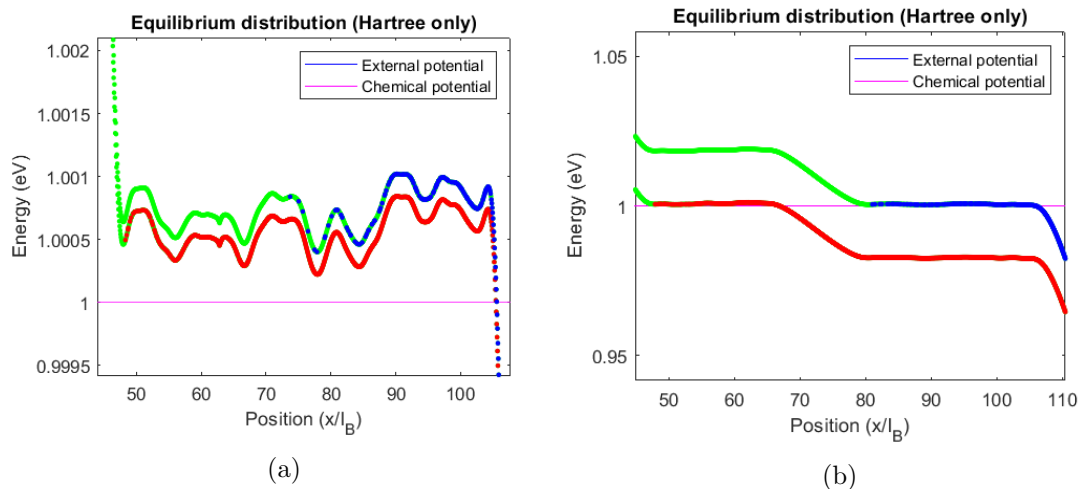
74

Figure B.3: Panel (a): same situation as in Fig. B.2 but now with the Fock term switched off. The spin-splitting Δ is the bare Zeeman-splitting E_z. Note the smallness of the fluctuations and compare to the energy scale in Fig. B.1. The fact that both the spin-up and the spin-down band are filled beyond the chemical potential is due to the fact that you can never fill up the states until *exactly* μ in a discrete system using the iteration strategy described above. Panel (b): the same situation as in panel (a) but now with a uniformly enhance spin-splitting of a factor hundred. Note the different energy scales on the vertical axes.

on the local filling factor) enhancement the spin-splitting (see Fig. B.3b). We note that the compressible strip widths stay more or less the same after the quick fix. As expected, the incompressible strip grows wider because the total potential should drop over a larger energy after the enhancement.

B.2.6 Non-equilibrium simulation results

As we discussed in Sec. 3.1.1, there are many uncertainties around the exchange enhancement of the spin-splitting. It might be the case that HF simulations tend to overestimate this effect. Hence, we switch off the Fock term and only use our code to produce non-equilibrium pictures for the CSG model (so not for the exchange model). The schematic non-equilibrium CSG pictures that are presented in Fig. 3.3 are based on Hartree-only simulations.

The Hartree-only simulation confirms the disappearance of the first incompressible strip at the threshold voltage $\Delta\mu = \Delta$ [9]. At the threshold voltage, the first and second compressible strips have merged into one wide compressible strip (see Fig. B.4).

The Hartree-only simulation also allows us to find the edge structure for large forward bias ($\Delta\mu > \Delta$). We find that an 'overhang region' forms in this case (see Fig. B.5). To calculate the inelastic relaxation rate in the CSG model at large forward bias, we
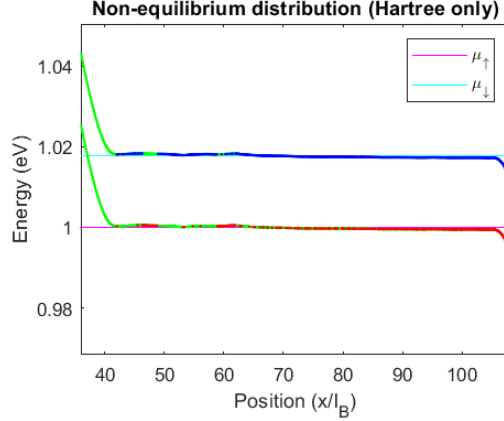
Figure B.4: The bands and their filling at the threshold voltage $\Delta\mu = \Delta$, given by the Hartree-only simulation. The following parameters were used: $L = 1$ μm, $l_B = 10$ nm, and the original spin-splitting $\Delta = 0.27$ meV is enhanced 100 times to polish away the fluctuations.

need an estimate of the width of this overhang region. For the voltage dependence of the scattering rate, we also want to know how this width depends on the applied bias. We can make a rough estimate of this width using the Hartree-only code with the homogeneously enhanced spin-splitting. We ensure that the electric field in the depleted region is around 10^6 V/m. Figure B.5 shows that the width of the overhang region is around $20 l_B = 200$ nm at $\Delta\mu = 1.5\Delta$, and $25 l_B = 250$ nm at $\Delta\mu = 2.5\Delta$. A wider overhang region leads to more inelastic scattering, and this could (partly) explain the increase of the scattering current (see Fig. 2.12) as the positive bias is made stronger. Strong forward bias like in Fig. B.5b also seems to open up the way for elastic scattering again. However, we should be careful to use our models at large bias because they will probably not be well-controlled there.

In equilibrium, the width of the outer compressible strip b_1 is around 170 nm, given the parameters $l = 250$ nm and $\nu_0 = 2$ [12]. This strengthens us in our belief that our estimate for the width of the overhang region is not way off because the overhang region is the outermost compressible strip in this non-equilibrium situation.

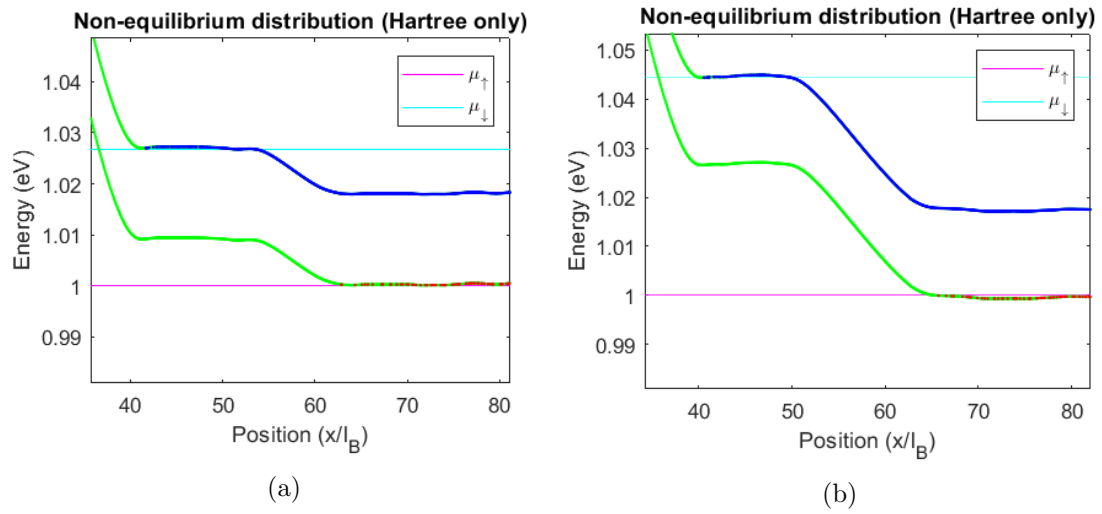Figure B.5: Illustration of the 'overhang' region that forms when $\Delta\mu > \Delta$. In panel (a): $\Delta\mu = 1.5\Delta$, and in panel (b): $\Delta\mu = 2.5\Delta$. The following parameters were used: $L = 1$ μm, $l_B = 10$ nm, and the original spin-splitting $\Delta = 0.27$ meV is enhanced 100 times to polish away the fluctuations. At $10\times$ enhancement, the width of the overhang region is more or less the same.

Appendix C

Value D_0^c

Here we present a derivation for the value of D_0^c: the squared one-component rms-strength of our effective nuclear magnetic field $\vec{B}_N(\vec{r})$. In Sec. 3.1.2, D_0^c is defined as follows:

$$\overline{B_N^\alpha(\vec{r})B_N^\beta(\vec{r'})} = D_0^c \delta_{\alpha\beta}\delta(\vec{r}-\vec{r'}). \tag{C.1}$$

We will find a value for D_0^c by comparison to a study by Taylor et al. about quantum dots [50]. They similarly consider the hyperfine interaction between an electron (in a QD) and the surrounding nuclei. They assume an infinite temperature distribution of N nuclei. We also consider this assumption justified for our problem because of the extremely low ordering temperature of the nuclei: $0.1 - 1$ mK for the Zeeman energy and about 0.1 μK for the nuclear dipole-dipole interaction. The electronic-nuclear dipole-dipole interaction is estimated to be of the order of 0.3 mK. Within the infinite T approximation, they arrive at the following expression for the (square of the) root-mean-squared nuclear field $B_{nuc} = \sqrt{\frac{\left\langle |\hat{\vec{B}}_{nuc}|^2 \right\rangle}{3}}$:

$$B_{nuc}^2 = \sum_\beta x_\beta b_\beta^2 \frac{I(I+1)v_0}{3} \int dr^3 |\psi(\vec{r})|^4 = \frac{h_1^2}{2}\int d\vec{r}|\psi(\vec{r})|^4 v_0. \tag{C.2}$$

For h_1, they find a value of 4.0 Tesla, which in units of energy is 102 μeV (multiplying by $g\mu_B$ where we take g to be the un-enhanced -0.44).

Note that their operator $\hat{\vec{B}}_{nuc}$ has no $\vec{r}$-dependence and is not the same as our nuclear field $\vec{B}_N(\vec{r})$. $\hat{\vec{B}}_{nuc}$ is defined as follows: $\hat{\vec{B}}_{nuc} = \sum_\beta b_\beta \sum_j v_0 |\psi(\vec{r}_{j,\beta})|^2 \hat{\vec{I}}^{\beta,j}$. Here ψ is the wave function of the electron that is coupled to the nuclei, v_0 is the unit cell volume (an area in our 2D approach), $I = 3/2$ is the magnitude of the nuclear spins, the β sum is over the different nuclear species in the unit cell with x_β their relative populations and b_β a measure of how much they contribute to the effective field [51].

In our approach, where we do not consider the different nuclear species, and $\left\langle \hat{\vec{B}}_{nuc} \right\rangle$

would correspond to $\sum_j v_0 |\psi(\vec{r_j})|^2 \vec{B}_N(\vec{r_j}) = \int d\vec{r} |\psi(\vec{r})|^2 \vec{B}_N(\vec{r})$. Furthermore, the expression corresponding to $\left\langle |\hat{\vec{B}}_{nuc}|^2 \right\rangle$ in our approach would be:

$$\left\langle |\hat{\vec{B}}_{nuc}|^2 \right\rangle = \int d\vec{r} \int d\vec{r'} |\psi(\vec{r})|^2 |\psi(\vec{r'})|^2 \left(B_N^x(\vec{r}) B_N^x(\vec{r'}) + B_N^y(\vec{r}) B_N^y(\vec{r'}) + B_N^z(\vec{r}) B_N^z(\vec{r'}) \right),$$

where $B_N^\alpha(\vec{r})$ is one of the three components of $\vec{B}_N(\vec{r})$. In the case of infinite T, any correlations between nuclear spins that might have been there are erased, and there is no preferred orientation for any spin to point in. Using this fact and the above expressions, we arrive at an expression for $\overline{B_{nuc}^2}$:

$$\overline{B_{nuc}^2} = \frac{1}{3} \int d\vec{r} \int d\vec{r'} |\psi(\vec{r})|^2 |\psi(\vec{r'})|^2 \left(\overline{B_N^x(\vec{r}) B_N^x(\vec{r'})} + \overline{B_N^y(\vec{r}) B_N^y(\vec{r'})} + \overline{B_N^z(\vec{r}) B_N^z(\vec{r'})} \right)$$

$$= D_0^c \int d\vec{r} |\psi(\vec{r})|^4. \quad \text{(C.3)}$$

Now, combining Eqs. (C.2) and (C.3), we can identify $D_0^c = \sum_\beta x_\beta b_\beta^2 \frac{I(I+1)v_0}{3} (g\mu_B)^2 = \frac{h_1^2 v_0}{2}$. For the unit cell volume v_0 we will take the value $(0.56 \text{ nm})^2$ in the following, because 0.56 nm is the lattice constant of GaAs. This gives a $D_0^c = 1.634 \times 10^{-27}$ [eV]^2 [m]^2.

Appendix D

Useful integrals

The following integrals are used in the calculation of the inelastic scattering rate in Sec. 3.3:

$$\int dx |f_{k_1}(x)|^2 |f_{k_2}(x)|^2 = \frac{1}{\sqrt{2\pi}l_B} e^{-\frac{1}{2}l_B^2(k_1-k_2)^2}, \tag{D.1}$$

$$\int dx f_{k_h}(x) f_{k_e-q_y}(x) f_{k_h+q_y}(x) f_{k_e}(x) = \frac{1}{\sqrt{2\pi}l_B} e^{-\frac{1}{2}l_B^2 q_y^2} e^{-\frac{1}{2}l_B^2(k_e-k_h-q_y)^2}, \tag{D.2}$$

$$\int dx |f_k(x)|^2 e^{iq_x x} = e^{-iq_x k l_B^2} e^{-\frac{1}{4}q_x^2 l_B^2}, \tag{D.3}$$

$$\int dx f_{k_1}(x) f_{k_2}(x) e^{iq_x x} = e^{-il_B^2 \frac{(k_1+k_2)}{2} q_x} e^{-\frac{1}{4}q_x^2 l_B^2} e^{-\frac{l_B^2}{4}(k_1-k_2)^2}. \tag{D.4}$$

Bibliography

[1] E. H. Hall, "On a New Action of the Magnet on Electric Currents," *American Journal of Mathematics*, vol. 2, no. 3, pp. 287–292, 1879. Publisher: Johns Hopkins University Press.

[2] K. v. Klitzing, G. Dorda, and M. Pepper, "New Method for High-Accuracy Determination of the Fine-Structure Constant Based on Quantized Hall Resistance," *Physical Review Letters*, vol. 45, pp. 494–497, Aug. 1980.

[3] J. Weis and K. von Klitzing, "Metrology and microscopic picture of the integer quantum Hall effect," *Philosophical Transactions of the Royal Society A: Mathematical, Physical and Engineering Sciences*, vol. 369, pp. 3954–3974, Oct. 2011.

[4] D. C. Tsui, H. L. Stormer, and A. C. Gossard, "Two-Dimensional Magnetotransport in the Extreme Quantum Limit," *Physical Review Letters*, vol. 48, pp. 1559–1562, May 1982.

[5] A. Y. Kitaev, "Fault-tolerant quantum computation by anyons," *Annals of Physics*, vol. 303, pp. 2–30, Jan. 2003.

[6] A. Stern and B. I. Halperin, "Proposed Experiments to Probe the Non-Abelian $= 5/2$ Quantum Hall State," *Physical Review Letters*, vol. 96, p. 016802, Jan. 2006.

[7] S. Hennel, B. A. Braem, S. Baer, L. Tiemann, P. Sohi, D. Wehrli, A. Hofmann, C. Reichl, W. Wegscheider, C. Rssler, T. Ihn, K. Ensslin, M. S. Rudner, and B. Rosenow, "Nonlocal Polarization Feedback in a Fractional Quantum Hall Ferromagnet," *Physical Review Letters*, vol. 116, p. 136804, Apr. 2016.

[8] K. R. Wald, L. P. Kouwenhoven, P. L. McEuen, N. C. van der Vaart, and C. T. Foxon, "Local Dynamic Nuclear Polarization Using Quantum Point Contacts," *Physical Review Letters*, vol. 73, pp. 1011–1014, Aug. 1994.

[9] D. C. Dixon, K. R. Wald, P. L. McEuen, and M. R. Melloch, "Dynamic nuclear polarization at the edge of a two-dimensional electron gas," *Physical Review B*, vol. 56, pp. 4743–4750, Aug. 1997.

[10] G. Yusa, K. Hashimoto, K. Muraki, T. Saku, and Y. Hirayama, "Self-sustaining resistance oscillations: Electron-nuclear spin coupling in mesoscopic quantum Hall devices," *Physical Review B*, vol. 69, p. 161302, Apr. 2004.

[11] S. M. Girvin, "The Quantum Hall Effect: Novel Excitations And Broken Symmetries," in *Aspects topologiques de la physique en basse dimension. Topological aspects of low dimensional systems* (A. Comtet, T. Jolicur, S. Ouvry, and F. David, eds.), vol. 69, pp. 53–175, Berlin, Heidelberg: Springer Berlin Heidelberg, 1999.

[12] D. B. Chklovskii, B. I. Shklovskii, and L. I. Glazman, "Electrostatics of edge channels," *Physical Review B*, vol. 46, pp. 4026–4034, Aug. 1992.

[13] B. I. Halperin, "Quantized Hall conductance, current-carrying edge states, and the existence of extended states in a two-dimensional disordered potential," *Physical Review B*, vol. 25, pp. 2185–2190, Feb. 1982.

[14] B. Jeanneret, B. D. Hall, H.-J. Bhlmann, R. Houdr, M. Ilegems, B. Jeckelmann, and U. Feller, "Observation of the integer quantum Hall effect by magnetic coupling to a Corbino ring," *Physical Review B*, vol. 51, pp. 9752–9756, Apr. 1995.

[15] C. W. J. Beenakker, "Edge channels for the fractional quantum Hall effect," *Physical Review Letters*, vol. 64, pp. 216–219, Jan. 1990.

[16] A. M. Chang, "A unified transport theory for the integral and fractional quantum hall effects: Phase boundaries, edge currents, and transmission/reflection probabilities," *Solid State Communications*, vol. 74, pp. 871–876, June 1990.

[17] K. Lier and R. R. Gerhardts, "Self-consistent calculations of edge channels in laterally confined two-dimensional electron systems," *Physical Review B*, vol. 50, pp. 7757–7767, Sept. 1994.

[18] T. Englert, D. C. Tsui, A. C. Gossard, and C. Uihlein, "g-Factor enhancement in the 2D electron gas in GaAs/AlGaAs heterojunctions," *Surface Science*, vol. 113, pp. 295–300, Jan. 1982.

[19] T. Ando and Y. Uemura, "Theory of Oscillatory g Factor in an MOS Inversion Layer under Strong Magnetic Fields," *Journal of the Physical Society of Japan*, vol. 37, pp. 1044–1052, Oct. 1974.

[20] A. P. Smith, A. H. MacDonald, and G. Gumbs, "Quasiparticle effective mass and enhanced g factor for a two-dimensional electron gas at intermediate magnetic fields," *Physical Review B*, vol. 45, pp. 8829–8832, Apr. 1992.

[21] V. T. Dolgopolov, A. A. Shashkin, A. V. Aristov, D. Schmerek, W. Hansen, J. P. Kotthaus, and M. Holland, "Direct Measurements of the Spin Gap in the Two-Dimensional Electron Gas of AlGaAs-GaAs Heterojunctions," *Physical Review Letters*, vol. 79, no. 4, p. 4, 1997.

[22] R. J. Nicholas, R. J. Haug, K. v. Klitzing, and G. Weimann, "Exchange enhancement of the spin splitting in a GaAs- Ga x Al 1 x As heterojunction," *Physical Review B*, vol. 37, pp. 1294–1302, Jan. 1988.

[23] A. Usher, R. J. Nicholas, J. J. Harris, and C. T. Foxon, "Observation of magnetic excitons and spin waves in activation studies of a two-dimensional electron gas," *Physical Review B*, vol. 41, pp. 1129–1134, Jan. 1990.

[24] G. Sukhodub, F. Hohls, R. J. Haug, D. K. Maude, D. Reuter, and A. D. Wieck, "Tunneling Between Spin Polarized Edge States Studied at High Magnetic Fields," *International Journal of Modern Physics B*, vol. 18, no. 27n29, pp. 3649–3652, 2004. Publisher: World Scientific.

[25] L. Rijkels and G. E. W. Bauer, "Hysteresis and defects of spin-polarized edge states in the integer quantum Hall regime," *Physical Review B*, vol. 50, pp. 8629–8635, Sept. 1994.

[26] J. Oswald and R. A. Rmer, "Exchange-mediated dynamic screening in the integer quantum Hall effect regime," *EPL (Europhysics Letters)*, vol. 117, p. 57009, Mar. 2017.

[27] D. Werner and J. Oswald, "Size scaling of the exchange interaction in the quantum Hall effect regime," *Physical Review B*, vol. 102, p. 235305, Dec. 2020.

[28] A. Crepieux, "Lecture on Luttinger liquid theory," Aug. 2006.

[29] A. M. Chang, "Chiral Luttinger liquids at the fractional quantum Hall edge," *Reviews of Modern Physics*, vol. 75, pp. 1449–1505, Nov. 2003.

[30] B. W. Alphenaar, P. L. McEuen, R. G. Wheeler, and R. N. Sacks, "Selective equilibration among the current-carrying states in the quantum Hall regime," *Physical Review Letters*, vol. 64, pp. 677–680, Feb. 1990.

[31] B. J. van Wees, L. P. Kouwenhoven, E. M. M. Willems, C. J. P. M. Harmans, J. E. Mooij, H. van Houten, C. W. J. Beenakker, J. G. Williamson, and C. T. Foxon, "Quantum ballistic and adiabatic electron transport studied with quantum point contacts," *Physical Review B*, vol. 43, pp. 12431–12453, May 1991.

[32] S. Komiyama, H. Hirai, M. Ohsawa, Y. Matsuda, S. Sasa, and T. Fujii, "Inter-edge-state scattering and nonlinear effects in a two-dimensional electron gas at high magnetic fields," *Physical Review B*, vol. 45, pp. 11085–11107, May 1992.

[33] G. Müller, E. Diessel, D. Weiss, K. von Klitzing, K. Ploog, H. Nickel, W. Schlapp, and R. Lsch, "Influence of interedge channel scattering on the magneto-transport of 2D-systems," *Surface Science*, vol. 263, pp. 280–283, Feb. 1992.

[34] G. Müller, D. Weiss, A. V. Khaetskii, K. von Klitzing, S. Koch, H. Nickel, W. Schlapp, and R. Lsch, "Equilibration length of electrons in spin-polarized edge channels," *Physical Review B*, vol. 45, pp. 3932–3935, Feb. 1992.

[35] A. V. Khaetskii, "Transitions between spin-split edge channels in the quantum-Hall-effect regime," *Physical Review B*, vol. 45, pp. 13777–13780, June 1992.

[36] D. Paget, "Optical detection of NMR in high-purity GaAs: Direct study of the relaxation of nuclei close to shallow donors," *Physical Review B*, vol. 25, pp. 4444–4451, Apr. 1982.

[37] N. B. Zhitenev, R. J. Haug, K. v. Klitzing, and K. Eberi, "Influence of a Current on the Edge Structure Probed by Time-Resolved Transport Measurements," *Europhysics Letters (EPL)*, vol. 28, pp. 121–127, Oct. 1994.

[38] M. Kataoka, N. Johnson, C. Emary, P. See, J. Griffiths, G. Jones, I. Farrer, D. Ritchie, M. Pepper, and T. Janssen, "Time-of-Flight Measurements of Single-Electron Wave Packets in Quantum Hall Edge States," *Physical Review Letters*, vol. 116, p. 126803, Mar. 2016.

[39] A. Würtz, R. Wildfeuer, A. Lorke, E. V. Deviatov, and V. T. Dolgopolov, "Separately contacted edge states: A spectroscopic tool for the investigation of the quantum Hall effect," *Physical Review B*, vol. 65, p. 075303, Jan. 2002.

[40] E. V. Deviatov, A. Wrtz, A. Lorke, M. Yu. Melnikov, V. T. Dolgopolov, D. Reuter, and A. D. Wieck, "Two relaxation mechanisms observed in transport between spin-split edge states at high imbalance," *Physical Review B*, vol. 69, p. 115330, Mar. 2004.

[41] A. M. Lunde and G. Platero, "Hyperfine interactions in two-dimensional HgTe topological insulators," *Physical Review B*, vol. 88, p. 115411, Sept. 2013.

[42] J. Danon, "Spin-flip phonon-mediated charge relaxation in double quantum dots," *Physical Review B*, vol. 88, p. 075306, Aug. 2013.

[43] H. le Sueur, C. Altimiras, U. Gennser, A. Cavanna, D. Mailly, and F. Pierre, "Energy Relaxation in the Integer Quantum Hall Regime," *Physical Review Letters*, vol. 105, p. 056803, July 2010.

[44] H. Bruus and K. Flensberg, *Many-body quantum theory in condensed matter physics: an introduction*. Oxford university press, 2004.

[45] H. Kamata, T. Ota, K. Muraki, and T. Fujisawa, "Voltage-controlled group velocity of edge magnetoplasmon in the quantum Hall regime," *Physical Review B*, vol. 81, p. 085329, Feb. 2010.

[46] F. C. Zhang and S. Das Sarma, "Excitation gap in the fractional quantum Hall effect: Finite layer thickness corrections," *Physical Review B*, vol. 33, pp. 2903–2905, Feb. 1986.

[47] M. P. Zaletel and R. S. K. Mong, "Exact matrix product states for quantum Hall wave functions," *Physical Review B*, vol. 86, p. 245305, Dec. 2012.

[48] A. M. Lunde and G. Platero, "Helical edge states coupled to a spin bath: Current-induced magnetization," *Physical Review B*, vol. 86, p. 035112, July 2012.

[49] G. Sharma, T. Gaebel, E. Rej, D. J. Reilly, S. E. Economou, and E. Barnes, "Enhancement of nuclear spin coherence times by driving dynamic nuclear polarization at defect centers in solids," *Physical Review B*, vol. 99, p. 205423, May 2019. arXiv: 1810.06542.

[50] J. M. Taylor, J. R. Petta, A. C. Johnson, A. Yacoby, C. M. Marcus, and M. D. Lukin, "Relaxation, dephasing, and quantum control of electron spins in double quantum dots," *Physical Review B*, vol. 76, p. 035315, July 2007.

[51] D. Paget, G. Lampel, B. Sapoval, and V. I. Safarov, "Low field electron-nuclear spin coupling in gallium arsenide under optical pumping conditions," *Physical review B*, vol. 15, no. 12, p. 5780, 1977. Publisher: APS.